Taylor, B., Huchon, P., Klaus, A., et al., 1999
Proceedings of the Ocean Drilling Program, Initial Reports Volume 180

4. EXPLANATORY NOTES[1]

Shipboard Scientific Party[2]

INTRODUCTION

This chapter includes information on shipboard methods that will help the reader understand the basis for our preliminary interpretations and also help the interested investigator select samples for further analysis. Coring techniques and core handling, including the numbering of sites, holes, cores, sections, and samples, are the same as those reported in previous *Initial Reports* volumes of the *Proceedings of the Ocean Drilling Program* and are only briefly summarized within this chapter.

Reference Depths

Seafloor depths and cored intervals below seafloor (meters below seafloor, mbsf) are determined by drill-pipe measurement.

Numbering of Sites, Holes, Cores, Sections, and Samples

Ocean Drilling Program (ODP) drill sites are numbered consecutively from the first Deep Sea Drilling Project (DSDP) site drilled by the *Glomar Challenger* in 1968. A site refers to one or more holes drilled while the ship is positioned over a single acoustic beacon. The first hole drilled at a given site is assigned the site number modified by the suffix "A," the second hole takes the site number and suffix "B," and so forth. These suffixes are assigned regardless of recovery as long as penetration takes place. This is exemplified by Hole 1108A, the first one drilled during Leg 180, which consisted of a jet-in test to 16.3 mbsf.

Each cored interval is generally 9.5 m long, which is the length of a core barrel. Coring intervals may be shorter and may not necessarily be adjacent if separated by intervals that are drilled but not cored. The depth interval assigned to an individual core begins with the depth

[1]Examples of how to reference the whole or part of this volume.
[2]Shipboard Scientific Party addresses.

Ms 180IR-104

below seafloor at which the coring operation began and extends to the depth at which the coring operation ended for that core.

A recovered core is typically divided into 1.5-m-long sections that are numbered serially from the top, from 1 through 7 (or less if partial recovery). When the recovered core is shorter than the cored interval, the top of the core is equated with the top of the cored interval by convention to achieve consistency in handling analytical data derived from the cores. Also by convention, material recovered from the core catcher is placed in a separate section during the core description, labeled CC (core catcher), and placed below the last (bottom) section recovered in the liner. When material is recovered only in the core catcher, the core catcher is placed at the top of the cored interval.

Samples removed from a core section are designated by distance measured in centimeters from the top of the section to the top and bottom of each sample removed from that section. A full identification number for a sample consists of the following information: leg, site, hole, core number, core type, section number, and interval in centimeters measured from the top of the section (Fig. F1). For example, "180-1108B-26R-2, 20–25 cm" represents a sample removed from the interval between 20 and 25 cm below the top of Section 2, Core 26 (R designates that this core was taken during rotary core barrel coring) of Hole 1108B during Leg 180.

All ODP core identifiers indicate core type. The following abbreviations are used: H = advanced hydraulic piston core (APC); X = extended core barrel (XCB); R = rotary core barrel (RCB); and W = wash core.

F1. Diagram illustrating core, section, and sample numbering, p. 51.

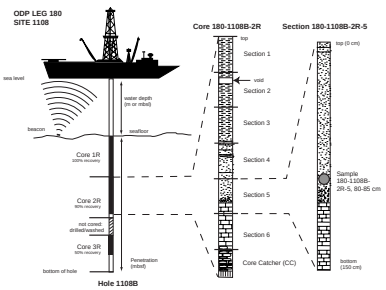

Core Handling

As soon as a core is retrieved on deck, a sample of sediment is taken from the core catcher and given to the paleontological laboratory for an initial age assessment. The core liner with the core inside is marked into section lengths, each section is labeled, and the core is then cut into sections. If whole-round samples are to be taken, the desired intervals are identified and cut out of the core, and then the sections are cut. When possible, whole-round samples are taken from the bottom of sections. During Leg 180, whole-round samples were taken for interstitial water (IW) analyses, organic geochemistry, microbiology, and post-cruise permeability measurements. For safety monitoring, small (~5 cm^3) plugs of sediment are taken from the end of one section per core for headspace gas analysis. If pockets of gas are present, a vacutainer gas sample is taken through the core liner.

Each section is then sealed at the top and bottom by using acetone to seal color-coded plastic caps to the plastic core liner. A blue cap marks the top of a section, a clear cap marks the bottom of a section, and a yellow cap marks the end of a section from which a whole-round sample has been removed. The sample code (e.g., IW) is written on the yellow cap. The core sections are then carried into the laboratory where the length of the core sections and any samples taken are logged into the shipboard database.

After the core sections equilibrate to ambient lab temperature (~3 hr), they are run through the multisensor track (MST) and thermal conductivity measurements are made for soft sediments (see "Multisensor Track Measurements," p. 29). Cores are subsequently split lengthwise into working and archive halves. The archive half is used for nondestructive measurements: visual core description, paleomagnetics, magnetic susceptibility, and color reflectance. Samples are taken from the

working half for shipboard physical properties measurements (see "Physical Properties," p. 28) before being sampled for additional shipboard and postcruise studies. The archive halves are photographed a whole core at a time, and close-up photographs are taken as requested. Finally, the core sections are put into labeled plastic tubes, sealed, and transferred to cold-storage space aboard the drilling vessel. Following the cruise, the cores from Leg 180 were transported to the Gulf Coast Repository of the Ocean Drilling Program in College Station, Texas.

LITHOSTRATIGRAPHY

Sediment Core Description Forms

Leg 180 sediment classification is based on visual core description and smear-slide analysis. Data are condensed to ODP standard barrel-sheet format and presented using the program AppleCORE. The shipboard sedimentologists adopted the widely used classification scheme of Mazzullo et al. (1988). The only significant modification is a further subdivision of volcaniclastic sediment, which is described in "Classification of Sediments and Sedimentary Rocks," p. 6. The shipboard sedimentologists also collected spectrophotometer reflectance and magnetic susceptibility data on the archive multisensor track.

Graphic Lithology Column

Sediment type is represented graphically on the core description forms (barrel sheets) using the symbols illustrated in Figure F2. In the "Graphic Lithology" column, major and minor lithologies are represented. Only lithologies that constitute at least 10% of the core are shown, and only lithologic units that are 10 cm or greater in thickness are portrayed in this column. Thin interbeds (<20 cm) of contrasting sediments or sedimentary rocks are indicated in the "Graphic Lithology" column by a vertical subdivision into average percentages.

F2. Key to symbols used in core description and barrel sheets, p. 52.

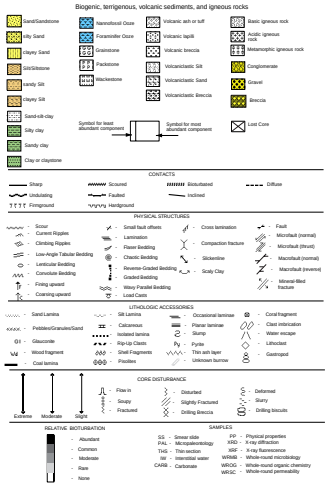

Sedimentary Structures

The location and nature of sedimentary structures in the cores are shown in the "Structure" column of the core description form, using the nomenclature of Miall (1984), Mazzullo et al. (1988), and Frey and Pemberton (1984). Standard key symbols are used on ODP visual core description (VCD) forms and barrel sheets (Fig. F2).

Sediment Disturbance

Observations of drilling-related disturbance over an interval of 20 cm or more are recorded in the "Disturbance" column using the symbols in Figure F2. The degree of drilling disturbance is described for soft and firm sediments using the following categories:

1. Slightly disturbed: bedding contacts are slightly deformed.
2. Moderately disturbed: bedding contacts have undergone extreme bowing.
3. Highly disturbed: bedding is completely deformed as flow-in, coring/drilling slurry, and other soft stretching and/or compressional shearing structures attributed to the coring/drilling.

4. Soupy: intervals are water saturated and have lost all aspects of original bedding.

The degree of fracturing within indurated sediments is described using the following categories:

1. Slightly fractured: core pieces are in place and broken.
2. Moderately fractured: core pieces are in place or partly displaced, but original orientation is preserved, or recognizable (drilling slurry may surround fragments; i.e. drilling/coring "biscuits" are evident).
3. Highly fractured: core pieces are probably in correct stratigraphic sequence, but original orientation is lost.
4. Drilling breccia: core is crushed and broken into many small and angular pieces, with original orientation and stratigraphic position lost; often drilling breccia is completely mixed with drilling slurry.

Samples

The position of samples taken for analysis from each core are indicated by letters in the "Sample" column of the core description form as follows: SS (smear slide), THS (thin section), PAL (micropaleontology), IW (interstitial water), XRF (X-ray fluorescence), XRD (X-ray diffraction), and PMG (palaeomagnetic plug), WRMB (whole-round microbiology), WROC (whole-round organic chemistry), and WRSC (whole-round permeability).

Lithologic Description

The lithologic description that appears on each of the VCD forms consists of a list of major lithologies followed by a more detailed description of the composition (as determined from smear slides), color, sedimentary characteristics, and other notable features. Descriptions and locations of thin, interbedded, or minor lithologies are also included in the text.

Nomenclature for the thickness of sedimentary beds and laminae remains unchanged from Mazzullo et al. (1988), using standard terms such as thinly laminated (1–3 mm), laminated (3 mm–1 cm), very thin bedded (1–3 cm), thin bedded (3–10 cm), medium bedded (10–30 cm), thick bedded (30–100 cm), and very thick bedded (>100 cm).

Smear-Slide Summary

Tables are included that summarize data from smear slides. Because smear slides are generally unreliable for quantitative analysis, relative abundances are estimated qualitatively using the following categories:

Abundant (a) = 51%–100%,
Common (c) = 11%–50%,
Rare (r) = 1%–10%, and
Trace (Tr) = ≤1%.

Initials of the shipboard scientists who described the smear slides are given in the table. The sedimentary categories recognized in smear slides were customized to reflect the actual recovery during Leg 180 (Table T1).

T1. Sedimentary smear-slide table, p. 68.

Grain sizes were routinely estimated using smear slides combined with visual observation of the cores to produce data shown in the "Grain Size" column of the core description forms (barrel sheets). These data were smoothed and processed to show downhole variation where recovery was sufficient.

X-Ray Diffraction

Bulk-rock XRD analyses were undertaken on a limited number of samples to determine mineral composition. Standard XRD operating procedure and conditions were adhered to, and an interactive software package (R. Petschick, Macdiff 3.1, 1995) was used to help identify the main minerals. Only qualitative estimates of mineral abundances were made.

Thin-Section Analysis

Thin sections were used to help identify the composition of siltstones and sandstones. Tables are included that summarize data from these slides. Percentages of minerals, rock fragments, matrix (including cement), and bioclasts are given (Table T2). The main constituents were estimated qualitatively using the following categories:

T2. Sedimentary rock thin-section table, p. 69.

Abundant (A) = 51%–100%,
Common (C) = 11%–50%, and
Rare (R) = 1%–10%.

Lowercase letters based on the same system were used to indicate subcategories (e.g., quartz [A], strained quartz [a], and unstrained quartz ([c]) of the following major constituents: quartz, feldspar, mica, accessory minerals, volcanic rock fragments, sedimentary rock fragments, metamorphic rock fragments, and foraminiferal types. Initials of the shipboard scientists who described the thin sections are given in the table.

Archive Multisensor Track (AMST)

During Leg 180, the newly developed AMST was utilized for the first time, following the procedures set out in the accompanying instruction manual. Spectral color (false color) and magnetic susceptibility (except for Cores 180-1108B-1R through 20R) were collected. The data collected are displayed as two graphs on the visual display unit. The first graph (top) displays the height of the core as measured by the LB1011 laser displacement transducer. The second graph displays the spectral data measured by the Minolta CM2002 spectrophotometer. Color in the graph indicates the intensity (0%–100%) at the specific wavelength (400–700 nm at 10-nm bins). The data were stored in the central shipboard computer system for processing and archiving (see **ASCII format**). During operation it was noted that the recorded color spectrum varied according to whether the sediment was wet or dry. This was problematic, especially for sands that dried quickly. Details of the magnetic susceptibility methods are described in **"Paleomagnetism,"** p. 21.

Classification of Sediments and Sedimentary Rocks

Introduction

The sediment classification system used during Leg 180 closely follows that proposed for ODP by Mazzullo et al. (1988). This classification is descriptive rather than genetic and is based mainly on sediment composition and texture. The classification depends entirely on the data collected on board the *JOIDES Resolution* (Fig. F3), including smear-slide analysis and thin-section analysis for components and grain size, visual core descriptions, and coulometrically determined calcium carbonate contents. During Leg 180 we encountered a need to classify several different sediment types as follows:

1. Volcaniclastic sediments. Clastic sediments of volcanic provenance are described in the same fashion as siliciclastic sediments, noting the dominant composition of the volcanic grains.
2. Unsorted to poorly sorted sediments. The ODP classification does not adequately address unsorted or poorly sorted siliciclastic or volcaniclastic sediments, such as those characterized by debris flows (debrites).
3. Carbonate rocks. Wackestones are defined as fine-grained limestones; packstones are limestones with a packed fabric including fine-grained interstitial sediment; and grainstones have a packed fabric without matrix.

F3. Diagram showing classes of granular sediment, p. 53.

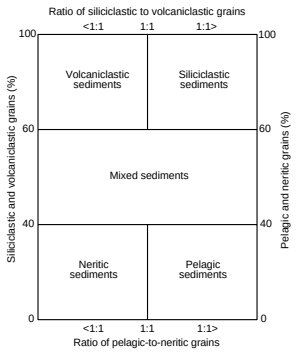

Classes of Granular Sediment

The following types of grains are found in granular sediments: (1) pelagic, (2) neritic (calciclastic), (3) siliciclastic, (4) volcaniclastic, and (5) mixed grain. Pelagic grains are composed of the organic remains of open-marine siliceous and calcareous microfauna and microflora (e.g., radiolarians and nannofossils), and associated organisms. Neritic grains are composed of coarse-grained calcareous (i.e., fossil) debris and fine-grained calcareous grains of nonpelagic origin (e.g., micrite). Siliciclastic grains are composed of mineral and rock fragments derived from igneous, sedimentary, and metamorphic rocks. Volcaniclastic grains are composed of rock fragments, glass, and minerals derived from volcanic sources.

Granular sediments are identified as follows:

1. Pelagic sediments are composed of >60% pelagic and neritic grains and <40% siliciclastic grains. They also contain a higher proportion of pelagic rather than neritic grains.
2. Neritic sediments are composed of >60% neritic and pelagic grains and <40% siliciclastic and volcaniclastic grains.
3. Siliciclastic (terrigenous) sediments are those having >50% terrigenous component, classified on the basis of grain size as shown in Figure F4. This classification follows that of ODP Leg 178 (Shipboard Scientific Party, 1999a) in that sediments having >75% of a single component are given that name (e.g., 23% silt, 77% sand = SAND or 24% clay, 76% silt = SILT).
4. Volcaniclastic sediments are composed of >60% siliciclastic and volcaniclastic grains and <40% pelagic and calciclastic grains. They contain a higher proportion of volcaniclastic than siliciclastic grains. This class includes epiclastic sediment (volcanic

F4. Lithologic classification scheme for sediments with terrigenous components, p. 54.

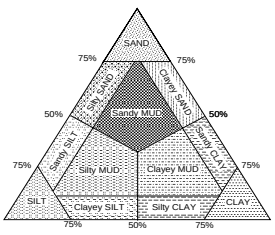

detritus produced by erosion of volcanic rocks by wind, water, and ice), pyroclastic sediment (products of degassing of magma), and hydroclastic sediment (produced by granulation of steam explosions and quenching).

Principal Names

For pelagic sediment, the principal name describes the composition and degree of consolidation using the following terms:

1. Ooze: unconsolidated calcareous and/or siliceous pelagic sediments;
2. Chalk: firm pelagic sediment composed predominantly of calcareous pelagic grains; and
3. Limestone: hard pelagic sediment composed predominantly of calcareous pelagic grains.

For siliciclastic sediments, the principal name describes the texture and is assigned according to the following guidelines: (1) the Udden-Wentworth grain-size scale (Wentworth, 1922) defines the grain-size ranges and the names of the textural groups (gravel, sand, silt, and clay) and subgroups (fine sand, coarse silt, etc.) that are used as the principal names of granular sediment; and (2) the suffix "-stone" is affixed to the principal names sand, silt, and clay if the sediment is lithified.

Volcanogenic sediments of various types were extensively recovered during Leg 180. We use the term volcanogenic for all sediments of mainly volcanogenic origin including clastic sediments (i.e., volcaniclastic sediments and sedimentary rocks), fine-grained (volcanic-derived) sediments and sedimentary rocks, and diagenetic sediments and sedimentary rocks of volcanic origin. We used a classification scheme followed by the shipboard sedimentologists during Leg 152 (Shipboard Scientific Party, 1994). This differs somewhat from the classification scheme recommended by Mazzullo et al. (1988). This (siliciclastic type) textural classification separates the various volcaniclastic sediments (and sedimentary rocks) into volcaniclastic gravel (volcaniclastic conglomerate; grain size = >2.0 mm), volcaniclastic sand (volcaniclastic sandstone; grain size = 2.0–0.063 mm), volcaniclastic silt (volcaniclastic siltstone; grain size = 0.063–0.002 mm), and volcanogenic clay (volcanogenic claystone; grain size = <0.002 mm). Sediment modifiers are vitric (glass), crystal (mineral fragments), and lithic (rock fragments). For example, a volcanic sand composed of 45% glass, 35% feldspar crystals, and 20% lithic fragments was named a crystal vitric volcanic sand with lithic fragments. Wherever appropriate, comments were added on the core description forms regarding the presumed pyroclastic or epiclastic origin. In addition, dispersed volcanic particles (<10% from smear-slide observations) were noted on the core description forms. We use the terms volcanic breccia and volcanic conglomerate for poorly sorted deposits that consist of angular or rounded clasts, respectively, of mainly volcanic origin in a fine-grained matrix. When evidence of primary (pyroclastic) origin was available for fine-grained sediments, we use the terms lapilli or lapillistone (2–64 mm in grain size) and ash or tuff (<2 mm in grain size), as defined by Mazzullo et al. (1988).

Modifiers

Where possible, sediment types are distinguished on the basis of the dominant component (>60%), which provides the principal lithologic name (e.g., volcaniclastic sediment and pelagic sediment). When a component comprises 25%–50% of the sediment, it is mentioned as a major modifier preceding the principal name (e.g., diatomaceous clay and nannofossil silty sand). Minor constituents (10%–25%) are included using the term "-bearing" (e.g., diatom-bearing clay and nannofossil-bearing silty sand). The sediment modifiers are ordered so that the minor modifier(s) precede the major modifier(s).

Coarse-Grained Deposits

Coarse siliciclastic sediments (i.e., nonvolcanogenic) were recovered during Leg 180. These sediments were divided into conglomerates (rounded clasts) and breccias (angular clasts). Classification of clast types was the same as that employed for coarse (rudaceous) volcaniclastic sediments.

Conglomerates were subdivided according to texture and composition. Clast-supported conglomerates are termed orthoconglomerates, whereas matrix-supported conglomerates are termed paraconglomerates (synonymous with diamictite). Conglomerates composed of one rock type are termed oligomictic, whereas conglomerates composed of several rock types are termed polymictic. Clast-supported types (orthoconglomerate) commonly relate to traction current depositional processes, whereas matrix-supported types (paraconglomerate) are commonly deposited by mass-flow processes and are known as debris flows, or debrites (but also include deposits from high-concentration turbidity currents). The classification used for different clast fabrics is shown in Figure F5 (after Schulz, 1984). Where practicable, conglomerates derived from clasts within the depositional basin (i.e., intraformational) were distinguished from those derived from outside the basin (i.e., extraformational).

F5. Schematic diagram showing the different types of debrites, p. 55.

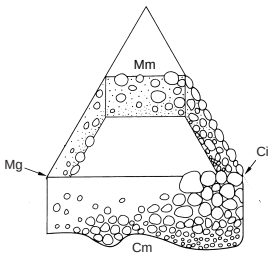

Sediment Gravity Deposits and Current Deposits

Successions recovered during Leg 180 include turbidity current deposits that vary in grain size and bed thickness. Some other fine-grained laminated facies were deposited by bottom currents (contourites). Descriptive criteria used to separate these sediment types are as follows:

Turbidites are commonly recognized by reference to the classic descriptive scheme (Fig. F6) of Bouma (1962) (divisions T_A to T_E). These are often referred to as "classical turbidites." Many beds deposited by turbidity currents cannot be described using the Bouma (1962) scheme. Such beds commonly vary from massive to normally graded or inversely graded, and were deposited from high-concentration turbidity currents (Pickering et al., 1989). In addition, fine-grained turbidites recovered during Leg 180 commonly exhibit the $T_{C–D–E}$ divisions corresponding to cross-laminated silt, parallel-laminated silt, and mud components. Bouma's (1962) original scheme is too generalized for application to these muddy turbidites. Accordingly, Piper (1978) further subdivided the T_D and T_E divisions of Bouma into laminated silt (D), laminated mud (E_1), graded mud (E_2), ungraded mud (E_3), and H (pelagic and hemipelagic) intervals (Fig. F7). Our interpretations of the fine-grained deposits

F6. Schematic representation of internal structure of facies within turbidites, p. 56.

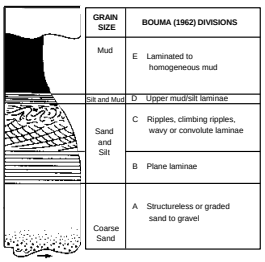

F7. Piper's (1978) descriptive scheme for muddy turbidites used during Leg 180, p. 57.

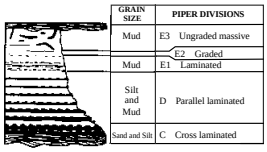

recovered during Leg 180 were based upon detailed visual and hand-lens examinations using Piper's (1978) scheme.

Furthermore, some horizons recovered during Leg 180 were interpreted as contourites (i.e., current deposits). The most important characteristics for distinguishing turbidites from contourites are repetitive internal structure (the "Bouma" sequence) and a tendency to form thick and repetitively bedded stratigraphic successions (Stow and Piper, 1984).

IGNEOUS AND METAMORPHIC PETROLOGY

The procedures and methods for igneous and metamorphic descriptions of the core during Leg 180 generally follow those adopted during Leg 147 (Gillis, Mével, Allan, et al., 1993), Leg 153 (Cannat, Karson, Miller, et al., 1995a), Leg 176 (Dick, Natland, Miller, et al., 1999b), and Leg 179 (Pettigrew, Casey, Miller, et al., 1999c). To ensure accurate core descriptions, thin-section petrography of representative samples was integrated with the VCDs (Fig. F8). When possible, identification of mineral phases was confirmed by XRD analyses according to standard ODP procedures outlined in previous *Initial Reports* volumes (e.g., Volume 118; Shipboard Scientific Party, 1989). The XRF analyses were also conducted according to ODP standards. After coarse crushing, samples were ground in a tungsten carbide shatterbox. Ignited rock powder in 600-mg aliquots was intimately mixed with a fusion flux consisting of 80 wt% lithiumtetraborate and 20 wt% heavy absorber La_2O_3. The glass disks for the analysis of the major oxides were prepared by melting the mixture in a platinum mold in an electric induction furnace. Trace elements were determined on pressed powder pellets prepared from 5 g of rock powder (dried at 110°C) mixed with a small amount of a polyvinyl alcohol binder solution. The calibration of the XRF system was based on the measurement of a set of reference rock powders. A Compton scattering technique was used for matrix absorption correction for trace element analysis. Loss on ignition (LOI) for each sample was determined by the standard practice of heating an oven-dried (110°C) 20-mg sample to 1100°C for 12–24 hr. A list of the elements analyzed and the operating conditions for Leg 180 XRF analyses are presented in Table T3.

Alteration intensity was classified as follows: negligible (<2%), slight (2%–10%), moderate (10%–40%), high (40%–80%), and pervasive (80%–100%). A column on the VCDs shows the variation in the degree of alteration (see "Core Descriptions" contents list).

F8. Example of visual core description form, p. 58.

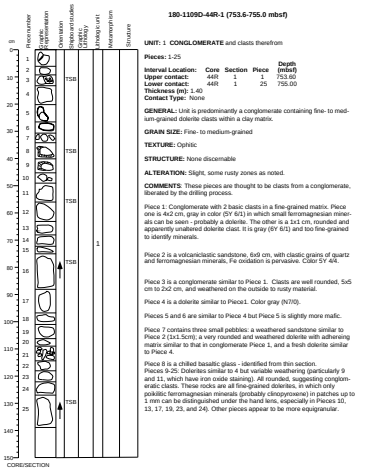

T3. XRF analytical conditions, p. 70.

Igneous Petrology

General Procedures

All igneous petrography and petrology observations are stored in paper and electronic form and in project-designed spreadsheets following the definitions given below. Details of core curation and handling are discussed in "Core Handling," p. 2. Standard ODP VCD sheets were used to document the igneous rock cores. The VCD sheets include graphical representations and summaries of the dominating macroscopic features (see "Core Descriptions" contents list). Descriptions of microscopic features were archived in text files (see "Core Descriptions" contents list).

Igneous intervals were defined on the basis of primary igneous lithologies, textures, and contacts. The intervals do not necessarily imply intrusive relationships. The natures of the igneous contacts were systematically recorded together with igneous structures, mineralogies, and textures. Mineral modes and grain sizes were visually estimated, and textures and fabric evaluated. The observations were recorded for each lithologic interval. A summary of the individual measurements is given below.

Rock Classification

The classification of plutonic rocks followed International Union of Geological Sciences (IUGS) recommendations (Le Maitre, 1989; Figs. F9A, F9B) with minor modifications.

The appropriate metamorphic rock names were used for mafic plutonic rock exhibiting the effects of dynamic metamorphism such that the assemblage consists of secondary hydrous minerals that obliterate the protolith mineralogy and texture, and for rock made up of recrystallized primary minerals such that the original igneous protolith cannot be recognized. The textural terms mylonitic, cataclastic, schistose, and gneissic were added to metamorphic rock names such as greenstone, amphibolite, or metagabbro to indicate that the rocks exhibit the effects of dynamic metamorphism.

Volcanic rocks were classified according to the nature and abundance of phenocryst assemblages as aphyric (1%), sparsely phyric (1%–2%), moderately phyric (2%–10%), or highly phyric (>10%). Volcanic rocks were further classified by phenocryst type using mineral name modifiers given in the order of decreasing abundance. Therefore, a moderately plagioclase-olivine phyric basalt contains 2%–10% phenocrysts with plagioclase more abundant than olivine.

Volcanic rock names are provisional even after thin-section description, unless the rock has been analyzed by XRF in which case it can be assigned a name in the IUGS system (Le Maitre, 1989) on the basis of normative mineralogy.

Primary and Secondary Minerals

The principal rock-forming minerals in the cores are plagioclase, olivine, clinopyroxene, hornblende (or other amphiboles), biotite, Fe-Ti oxides, and sulfides. For each of these minerals, data were recorded on the VCDs and in electronic form on spreadsheets: (1) estimated modal percent of the primary minerals, (2) largest size of mineral grains (measured along the longest axis in millimeters), (3) in the case of alteration, the estimated original percentage of primary minerals replaced by secondary phases, and (4) the percentages of secondary minerals such as chlorite, epidote, serpentine, and calcite. A lithology name based on IUGS definitions was generated from these data by a "Visual Basic for Applications" macro in the spreadsheet. An overall grain size was assigned using the terms fine grained (<1 mm), medium grained (1–5 mm), coarse grained (5–30 mm), and pegmatitic (>30 mm). Descriptions of mineral shapes were recorded using terms such as equidimensional, tabular, prismatic, platy, elongate, acicular, skeletal, and amoeboidal. Descriptions of general appearance were recorded using terms such as euhedral, subhedral, anhedral, rounded, deformed, and fractured.

F9. Classification of ultramafic, gabbroic, and silicic plutonic rocks, p. 59.

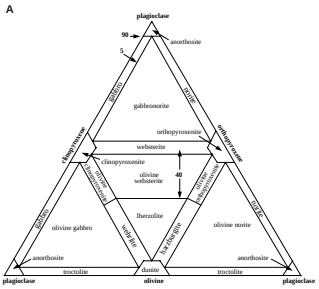

Igneous Textures

Textures of the plutonic rocks were characterized on the basis of grain shape, mutual contacts, and preferred mineral orientation. Rock textures such as equigranular, inequigranular, intergranular, and granular were used to describe the overall texture of each lithologic interval. Poikilitic, ophitic, subophitic, and interstitial textures were distinguished according to the predominant grain shapes in each interval. Igneous fabrics that were distinguished include lamination and lineation for rocks exhibiting a preferred dimensional orientation of mineral grains that was likely derived from magmatic processes, clusters for mineral aggregates, and schlieren for lenses of igneous minerals.

Textures of volcanic rocks were characterized on the basis of grain size and crystallinity (glassy or crystalline), the shape of the phenocrysts (euhedral, subhedral, anhedral, or skeletal), incipient crystals (crystallites or microlites), phenocrysts (seriate or glomerocrystic), relations between phenocrysts and matrix (intersertal or granular), and vesicularity. Magmatic flow textures include trachytoid (mainly for felsic rocks) and pilotaxitic (mainly for basic rocks).

Glass may be fresh (if basic, it is then called sideromelane) or devitrified. Hydrated basaltic glass is palagonite, which subsequently changes to a variolitic texture that is distinguished by poorly defined spherulite. Devitrification of acid glass (obsidian) leads first to pitchstone and subsequently to the formation of spherulites. Black, optically opaque material found in many of the Leg 180 rocks is known as tachylite (i.e., glass rendered opaque by microcrystalline iron oxides; Fisher and Schmincke, 1984, p. 96).

Igneous Structures

In plutonic rocks, igneous structures can be especially important in defining the mechanism of crystallization of the primary mineralogy (Irvine, 1982). Igneous structures include layering or lamination, gradational grain-size variations, gradational modal variations, gradational textural variations, and breccias. Layering was used to describe vertical changes in grain size, mode, or texture within an interval. Apart from gradational grain-size variations, these features were not encountered during Leg 180.

Volcanic rock structures were described according to the distribution of phenocrysts, vesicles, chilled margins, alteration, and vesicle fillings.

Contacts between Lithologic Intervals

The nature of igneous contacts is an important observation because it provides clues to the intrusive and/or structural relationships between intervals. The most common type of contact is the chilled contact. Contacts were encountered only on a few occasions during Leg 180.

Thin-Section Description

Thin sections of igneous rocks were examined to complement and refine the hand-specimen observations. In general, the same types of data were collected from thin sections as from hand-specimen descriptions. Modal data were collected using visual estimation by reference to standard charts. All data are summarized in ODP format thin-section descriptions (see **"Core Descriptions"** contents list). Crystal sizes were

measured using a micrometer scale and are generally more precise than hand-specimen estimates. The presence of inclusions, overgrowths, and zonation was noted, and descriptions of other special features were placed in the comment section. The presence and relative abundance of accessory minerals such as Fe-Ti oxides, sulfides, apatite, and zircon were also noted as well as the amount and nature of alteration.

Igneous Lithology, Interval Definitions, and Summary

The lithologic intervals adopted here were defined by vertical sections with consistent internal characteristics, and lithologies were separated based on geological contacts defined by significant changes in modal mineralogy or primary texture as encountered downhole. Generally, boundaries were not defined where changes in rock appearance were only the result of changes in the type or degree of metamorphism or the intensity of deformation. If the contact was recovered, its location was recorded by the core, section, position (in centimeters), and piece number. If the contact was not recovered but a significant change in lithology or texture was observed, the contact was placed at the lowest piece of the upper interval. The information recorded for each section of the core includes (1) rock type; (2) igneous, metamorphic, and/or deformational texture and structures; (3) extent, type, and intensity of deformation; (4) primary and secondary minerals present; (5) grain shape for each primary mineral phase; (6) evidence of preferred orientation; (7) the position of quartzo-feldspathic veins (whether of igneous or hydrothermal origin); and (8) general comments. The description and summary of each interval was entered into the standard ODP format where the general lithologic description and top and bottom of the interval are recorded with reference to curated core, section, piece(s), depth, and thickness.

Metamorphic Petrology

General Procedures

The VCDs of metamorphic characteristics were compiled together with stratigraphic, igneous, and structural documentation of the core. This information was recorded as completely as possible to provide two types of information: (1) the extent of replacement of primary minerals by metamorphic or secondary minerals, and (2) the extent to which metamorphic or alteration minerals contribute to any subsolidus fabric found in the core. These data, along with any other pertinent observations, were recorded in the VCDs. The following information was recorded for each section: leg, site, hole, core number, core type, section number, piece number (consecutive downhole), and position in the section. Terminologies adopted for metamorphic rock types, metamorphic textures and fabrics, metamorphic facies, and so forth, follow conventional usage (see "Core Descriptions" contents list).

Macroscopic and Thin-Section Descriptions

The metamorphic mineral assemblages and alteration intensities obtained from thin-section observations were recorded in the metamorphic VCDs. Primary phases (quartz, plagioclase, pyroxene, amphibole, alkali feldspar, biotite, muscovite, and rutile) and the secondary or retrograde minerals (sericite, chlorite, pyrite, ilmenite, and sphene) that

replace them were noted. Where possible, the volume percent of alteration for each phase was estimated in hand specimen and checked by observation of representative thin sections. Portions of pieces where primary textures were ambiguous or obliterated by secondary minerals were termed patches. Where thin-section analysis was available, pertinent observations were used to supplement information in the VCDs.

Detailed petrographic descriptions were made aboard ship to aid in identification and characterization of metamorphic and vein mineral assemblages. Stable mineral paragenesis were noted, as were textural features of minerals indicating overprinting events (e.g., coronas, overgrowths, and pseudomorphs). Mineral abundances were visually estimated. These data are recorded in the thin-section tables (see **"Core Descriptions"** contents list). The modal data allowed accurate characterization of the intensity of metamorphism and helped establish the accuracy of the macroscopic visual estimates of the extent of alteration.

Description of Metamorphic Fabrics

Assignment to metamorphic grade or facies was made on the basis of key index minerals as described in standard texts (e.g., Turner and Verhoogen, 1960; Fry, 1984).

Where metamorphic minerals were included in fabric elements, such as shear zones, cataclastic fabrics or foliations, textures, and associated minerals were recorded. For samples affected by crystal-plastic deformation, textural features noted include identities and abundances (volume percent) of porphyroclasts and their alteration products, neoblasts, and other minerals associated with and defining the fabric.

Breccias were defined as intervals of angular fragments in which clast rotation could be documented. Portions of the core crosscut by dense vein networks may appear to be brecciated; however, if adjacent clasts separated by the veins were not visibly rotated, they were described as net or mesh veined. Characterization of breccias included clast lithology and secondary phase mineralogy, matrix mineralogy, and abundances of clasts and mineral phases.

Fault gouge is defined as soft, uncemented, pulverized, claylike material—a mixture of minerals in finely divided form. The fault gouge was found along the fault or between the walls of a fault commonly associated with breccia.

Metamorphic Terminology

Metamorphic rocks are classified using a variety of criteria based on the overall aspect of the rock in hand specimen. Examples include slate, greenschist, serpentinite, marble, amphibolite, hornfels, gneiss, mylonite, and metagabbro, depending on factors such as grade, protolith composition, and deformation.

Metamorphic grade category: low grade, medium grade, and high grade, depending on the minerals assemblage.
Composition: for example, pelite, calc-silicate, and ultramafic.
Association: for example, ophiolite, migmatite, and metagabbro.

During Leg 180, we used the rock-type terms in the VCD because further classification is generally not possible unless full mineralogical information is available. In problematic cases the samples have been examined in thin section, which also allows an estimation to be made of

the metamorphic grade. For thin-section examination, we have used the guide to compositional categories and their grade indicators given by Fry (1984, pp. 97–102). Our nomenclature for cataclastic and mylonitic rocks follows Table 9.1 (p. 93) in the same book.

Other Terms

Crystalloblastic textures are crystalline textures produced by metamorphic recrystallization. Examples of crystalloblastic textures include

Granoblastic: a nonschistose rock with equidimensional crystals.
Nematoblastic: development during recrystallization of slender parallel prismatic crystals.
Lepidoblastic: foliated or schistose rock with foliation defined by the parallel orientation of minerals with a flaky or scaly habit.

Foliation is the term used to define all planar textures and structures in metamorphic rocks developed during metamorphism. Foliation may be defined by layering of contrasting mineralogies (*gneissosity*), planar-preferred orientations of individual grains (*schistosity*), planar-fracture surfaces (*cleavage*), or any combination of the three.

Porphyroblastic: a crystalloblastic texture with minerals of two or more distinct grain sizes. The large crystals are called *porphyroblasts*.
Poikiloblastic: a texture in which large porphyroblasts include numerous small mineral grains.
Mosaic: crystals are equigranular and equidimensional and are generally polygonal in shape with simple straight-line or gently curved intergranular boundaries.
Mylonitic: a very fine grained product of mechanical crushing with recrystallization of the primary minerals.
Sutured: crystals have highly irregular boundaries with much interpenetration of each grain into neighboring grains.

Cataclastic textures are produced by mechanical crushing without significant recrystallization. Examples of cataclastic textures include

Mortar: a texture consisting of larger mineral fragments set in a groundmass of crushed material derived from the same crystals.
Porphyroclastic: a cataclastic texture characterized by the presence of large relict mineral grains set in a matrix of smaller crushed grains.
Blastoporphyritic: a relict texture in a cataclastic metamorphic rock in which traces of an original porphyritic texture remain.

Lineation is a general term for the parallel orientation of textural or structural features that are linear.

STRUCTURAL GEOLOGY

The structural study of rocks sampled during Leg 180 was devoted mainly to understanding the mechanisms of extension in the footwall and hanging wall of a low-angle fault system just ahead of the tip zone of a propagating oceanic rift. Structural observations were made on

unlithified sediments and sedimentary rocks, and on igneous and metamorphic rocks.

Conventions for structural studies established during previous drilling legs (e.g., Leg 131, Shipboard Scientific Party, 1991; Leg 134, Shipboard Scientific Party, 1992b; Leg 141, Shipboard Scientific Party, 1992a) were generally followed during Leg 180. In addition, approaches used recently for the study of structures in sediments and sedimentary rocks were also employed (e.g., Leg 160, Shipboard Scientific Party, l996a). As far as possible, systems for recording soft- and hard-rock structures were merged into a single unified system.

Given the specific aims of Leg 180, special attention was paid to the vertical variations of strain in the vicinity of the fault zone. The descriptions focused on structural features concerning the style of deformation (e.g., flattening and simple shear), the strain gradient, and the strain kinematics.

The following sections deal with the macroscopic and microscopic descriptions of sediments and hard-rock cores. The aim is to identify and describe the observed structural features in a systematic and, if possible, quantitative way and then to orient them in the core reference frame.

Macroscopic Core Description

Descriptions and structural measurements were based on observations of the working half of the core (see **"Structural Measurements,"** p. 16). We followed the procedures used for the description of hard rocks in the *Initial Reports* "Explanatory Notes" chapters for Leg 153 (Shipboard Scientific Party, 1995a) and Leg 176 (Shipboard Scientific Party, 1999b). For soft rocks we followed the system employed during Leg 160 (Shipboard Scientific Party, l996a). Gradation and overlap between different features were identified by adding modifiers, descriptive comments, and sketches. The structural identifiers, listed in Table **T4** as a checklist, were entered into the structural logs that are included in the **"Supplementary Materials"** contents list.

T4. Structural identifiers, **p. 71.**

A structural log spreadsheet (Table **T5**) was used to record all forms of structural data. The following categories of structural identifiers were recorded: (1) drilling-induced structure, bedding, and unconformity; (2) slump folds; (3) joints; (4) folds (with the hinge-zone angle noted when possible); (5) crenulation cleavage, disjunctive cleavage, and foliation; (6) fault, brittle shear zone, and ductile shear zone; (7) sedimentary breccia and tectonic breccia (clast/matrix ratio as well as maximum and average clast size); and (8) veins and dikes. The structural log spreadsheets are provided in Excel 5.0 format in **"Supplementary Materials."**

T5. Structural core descriptions, **p. 72.**

For each of the above structures, the intensity of deformation was noted in three categories. The cleavage/foliation category was further subdivided into more specific structures as appropriate. Similarly, different linear structures were also assigned specific symbols (e.g., slickenlines and mineral lineations). Sense of shear was recorded where possible. The description and orientation of structural features were recorded using curated depths so that structural intervals could easily be correlated with other lithologic intervals.

Drilling-Induced Structures

Natural structures are sometimes difficult to distinguish from those caused by drilling and coring disturbance (Kopf and Flecker, 1996). In

general during Leg 180, planar structures having polished surfaces and/or linear grooves were regarded as tectonic induced rather than drilling induced. In zones of brecciation, features were attributed to drilling disturbance if their tectonic origin was in doubt. The recommendations of Lundberg and Moore (1986), as well as the approach adopted during Leg 160 (Shipboard Scientific Party, 1996a), were generally followed with regard to the recognition of drilling disturbance.

Structures in Sediments and Weakly Lithified Sedimentary Rocks

When dealing with sediments and weakly lithified sedimentary rocks, if the core length was relatively devoid of features we did not draw that interval, but merely marked the features on the data table (Table T5). The feature number was used to link data in the data table with drawings of the feature on the VCD form. In the data table, the feature is identified using the codes defined in the accompanying list of structural terms (Table T4).

Structures in Hard Rocks

Hard-rock structures were also recorded on the structural log spreadsheet as shown in Table T5.

Structural Measurements

All the structural features were recorded relative to core-section depths in centimeters from the top of the core section. Depth was defined as the point where the structure intersects the center of the cut face of the working half of the core, as detailed in the "Explanatory Notes" chapter of the Leg 153 *Initial Reports* volume (see fig. 15A, Shipboard Scientific Party, 1995a).

Apparent fault displacements were recorded as they appeared on the cut face of the archive half of the core and the end of broken pieces. Displacements observed on the core face were treated as components of dip-slip movement, either normal or reverse. Displacements of features visible on the upper and lower surfaces of core pieces were treated as components of strike-slip and termed sinistral or dextral. Displacements were measured between displaced planar markers parallel to the trace of the fault. Additional cuts and slickenside orientations were incorporated wherever possible to differentiate between apparent dip-slip, oblique-slip, and strike-slip displacements.

The measurement of the orientations of observed structures was taken with respect to the core reference frame (working half) (Fig. F10). The convention we used for the core reference frame is detailed in the "Explanatory Notes" chapter of the Leg 153 *Initial Reports* volume (Shipboard Scientific Party, 1995a) and shown at the top of the comments box in the structural data spreadsheets. All spreadsheet orientations are given in the core reference frame.

Planar structures were oriented using the techniques outlined during Legs 131 (Shipboard Scientific Party, 1991), 153 (Shipboard Scientific Party, 1995a), and 160 (Shipboard Scientific Party, 1996a). Apparent dip angles of planar features were measured on the cut face of the working half of the core. To obtain a true dip value, a second apparent dip reading was obtained where possible in a section perpendicular to the core face (second apparent orientation). Apparent dips in the cut plane of

F10. Conventions for measuring azimuths and dips of structural features, p. 61.

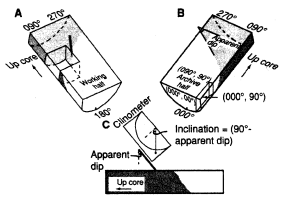

the working core were recorded as a two-digit number (between 00° and 90°) with a dip direction to 090° or 270°. In the second plane, apparent dip directions were recorded as either 000° or 180°. The dip and dip direction for the working half of the core were recorded on the spreadsheet together with second plane measurements. If the feature intersected the upper or lower surface of the core piece, measurements were made directly of the strike and dip in the core reference frame. Where broken surfaces exposed lineations or striations, the trend and plunge were measured directly and relative to the core reference frame. Fold hinge lines were identified in two mutually perpendicular sections and measured as discussed in the "Explanatory Notes" chapter of the Leg 153 *Initial Reports* volume (Shipboard Scientific Party, 1995a).

The two apparent dips and dip directions measured for each planar feature were used to calculate a true dip, following classical geometrical techniques.

Fabric Intensities and Textural Terms

A key for fabric intensity (Fig. F11) was used to refine identifier descriptions. Previous usage was modified to take account of the recovery during Leg 180. When feasible, (semi-)quantitative estimates of feature development were used to define a three-category relative intensity scale. It is important to recognize that this scale is based on different characteristics for different types of structures and that not all of the identifiers could be appropriately assigned an intensity value. We also emphasize that the intensity estimates are only semiquantitative at best and could not be fully quantified during core description.

Intensity was recorded for the following categories:

1. The intensity of joints and faults is related to spacing estimated by the linear intercept method along the central divide of the core piece. If a piece was unoriented, then spacing was estimated along the long axis of the piece. Because no stereological corrections were applied, these values remain at best semiquantitative.
2. Vein intensity relates to an estimate of the percentage of veining on the cut face of the archive half of the core.
3. Brecciation intensity relates to the relative percentage of clasts to the matrix.
4. Foliation intensities broadly relate to the spacing of foliation planes. In the case of an anastomosing foliation, the closer the foliation planes and the more planar they become, the higher the intensity value.
5. Crystal-plastic fabric intensities relate to the attenuation and degree of preferred alignment of porphyroclasts and the degree of preferred alignment of any mineral grains.
6. Fold intensity relates to the interlimb angle for individual or multiple folds.
7. Magmatic fabric relates to the structure of plutonic igneous rocks. Magmatic deformation intensity relates broadly to the degree of shape-preferred orientation of magmatic phases.

Three textural classes were selected for macroscopic description. It must be stressed that these classes do not necessarily directly relate to any single physical parameter, such as stress or strain. The definitions below were designed primarily for hand-sample observations where thin sections were not necessarily available. "Gneissic" refers to composi-

F11. Intensity scale for brittle and ductile features of igneous and metamorphic rocks, p. 62.

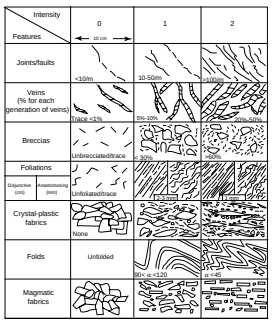

tional banding in a ductilely deformed rock in which porphyroclasts are commonly elongated parallel to the banding. "Schistose" refers to the visibility of platy or prismatic metamorphic minerals that define a preferred dimensional orientation and typically a parallel fissility. The terms "Mylonitic," "Ultra-mylonitic," and "Cataclastic" were used in accordance with the definitions presented by Twiss and Moores (1992; p. 53).

Thin-Section Descriptions

Thin sections of basement cores recovered during Leg 180 were examined to (1) confirm macroscopic descriptions of ductile and brittle structures; (2) determine the texture, the deformation at mineral scale, and the degree of recrystallization; (3) provide information regarding the kinematics of high-temperature ductile deformation and the time relationship with brittle deformation; and (4) document major structural zones and downhole textural variations. Where possible, the thin sections were oriented with respect to the core to preserve the original attitude of the core axis.

Selected samples were cut perpendicular to the foliation and parallel to any lineation to examine kinematic indicators and the shape-preferred orientation of minerals (see fig. 15, in the "Explanatory Notes" chapter of Shipboard Scientific Party, 1995a).

BIOSTRATIGRAPHY

Initial biostratigraphic determinations for calcareous nannofossils, planktonic foraminifers, and benthic foraminifers were based on core-catcher samples. Additional samples were subsequently investigated from selected core sections in order to refine the biostratigraphic zonal assignments. Abundance, preservation, and zonal data for each sample investigated were recorded in the JANUS paleontology database.

The nannofossil and foraminiferal biozonal schemes used are shown in Figure **F12,** with the events defining the zonal boundaries. Well-dated nannofossil and planktonic foraminiferal datums used during Leg 180 are shown in Table **T6.**

F12. Chronostratigraphic units correlated with fossil zonations and geomagnetic polarity, **p. 63.**

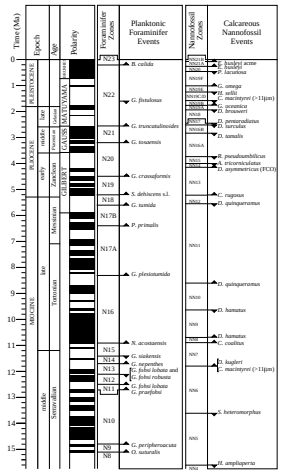

T6. Calcareous nannofossil and planktonic foraminifer age datums, **p. 73.**

Calcareous Nannofossils

Slides for nannofossil investigations were prepared by smearing sediment across a glass slide and attaching a cover glass. Taxon identifications were made under plane- and cross-polarized light using a Zeiss Axioscope microscope. Relative abundance estimates for individual species were made using a magnification of 1000×; abundances were estimated as follows:

D = dominant (more than 100 specimens of a species per field of view);
A = abundant (10–100 specimens of a species per field of view);
C = common (one to 10 specimens per field of view);
F = few (one specimen per 10 fields of view);
R = rare (fewer than one specimen per 10 fields of view);
B = barren (no nannofossils found); and
T = trace (fewer than one specimen per transect of slide).

Preservation of nannofossil specimens was characterized as follows:

VG = very good (no dissolution or secondary overgrowths of calcite). All specimens can be identified with certainty.
G = good (little dissolution or secondary overgrowths). Essentially all specimens can be identified to the species level.
M = moderate (slight to moderate dissolution and/or overgrowths). Identification of some species is impaired, but most species can still be identified.
P = poor (severe dissolution, breakage, or secondary overgrowths largely destroy primary morphological features). Many specimens cannot be identified to the species level; some cannot be identified to the generic level.

Specimens that have been reworked are designated by "r."

The calcareous nannofossil zonation used here (Fig. **F12**) is that of Martini (1971), with modifications by Rio et al. (1990). We were unable to consistently distinguish between Subzones NN19C and NN19D (the subzonal boundary is based on the first occurrence of *Gephyrocapsa* spp. [>5.5 µm]). Therefore, these two subzones have been combined as NN19C/D in this report.

Planktonic Foraminifers

The planktonic foraminiferal biozones followed are those of Blow (1969) as modified by Kennett and Srinivasan (1983). Correlations of zones to magnetostratigraphy and geochronology (Fig. **F12**) as well as the first appearance datum (FAD) and last appearance datum (LAD) of species (Table **T6**) are according to Berggren et al. (1995a) for the middle to late Miocene and Berggren et al. (1995b) for the late Neogene. Planktonic foraminiferal zones recognized in Papua New Guinea and vicinity were reviewed by Haig and Perembo (1990), who proposed that the FAD of *Globorotalia crassaformis* be used to approximate the base of Zone N20 in the western equatorial Pacific.

Unlithified to semilithified core sediment samples were soaked in beakers of water, broken up by hand if necessary, wet sieved over a 63-µm mesh screen, and dried. Lithified material was crushed to pea size, boiled in Calgon solution, sieved, and dried as before. Because of the fine-mesh screen used, juvenile specimens and small species dominated most of the well-preserved planktonic assemblages. Although the reported data are incomplete with respect to the total planktonic assemblages, the species abundances indicated on the site report tables were estimated from a portion of the sand fraction spread evenly over a 6 cm × 9.5 cm tray containing 45 fields of view at 25× magnification. The abundances were reported in the following categories:

D = dominant (>10 specimens per field of view);
A = abundant (2–9 specimens per field of view);
C = common (if used, the lower range of abundant);
F = few (0.5–1.0 specimen per field of view);
R = rare (1–3 specimens per tray);
P = present (if used, 1 specimen per 2–3 trays); and
B = barren (no planktonic foraminifers).

Preservational characteristics were indicated as follows:

VG = very good (no evidence of breakage or dissolution);
G = good (>90% of specimens unbroken);
M = moderate (30%–90% of the specimens unbroken); and
P = poor (dominated by fragments and broken or corroded specimens).

Benthic Foraminifers

The generic classification of Loeblich and Tappan (1988) was used and updated in some instances. Benthic species found in the western equatorial Pacific are illustrated in several publications including Graham and Militante (1959), Barker (1960), Hughes (1977), Burke (1981), Van Morkhoven et al. (1986), Kurihara and Kennett (1986, 1988), Hermelin (1989), Clark et al. (1994), and Akimoto (1994).

The bathymetric divisions (biotopes) occupied by modern benthic foraminiferal assemblages were designated following Ingle (1980). Reference to the literature listed above as well as other Indo-Pacific sources given in Haig and Perembo (1990) suggests upper depth limits for various species within the bathymetric divisions, used here for bathyal and abyssal biotopes to avoid problems arising from downslope transport of tests. These species upper depth limits, as given in Haig and Perembo (1990) and Perembo (1994), as well as biofacies data based on species abundance (Resig, 1984; Resig and Cheong, 1997; J. Resig, unpubl. data), were used to interpret paleobathymetry of the samples. Some of the diagnostic species for the various bathymetric divisions are as follows:

Inner neritic (0–50 m): *Alveolinella quoyi, Ammonia* spp., *Amphistegina* spp., *Baculogypsina sphaerulata, Calcarina calcar, Elphidium craticulatum, Lobatula lobatula, Marginopora vertebralis, Operculina* spp., *Pseudorotalia* spp., and *Quinqueloculina* spp.;

Outer neritic (50–150 m): *Anomalina glabrata, Anomalinoides colligerus, Baggina indica, Bolivina hantkeniana, Cancris auriculus, Rectobolivina striata,* and *Siphonina tubulosa;*

Upper bathyal (150–500 m; upper depth limit): *Brizalina alata, Bulimina alazanensis, Cibicidoides cicatricosus, Cribroparrella bengalensis, Globocassidulina murrhina, Oridorsalis umbonatus, Osangularia culter, Pyrgo depressa, Pleurostomella alternans, Siphonodosaria insecta,* and *Vulvulina pennatula;*

Middle bathyal (500–2000 m; upper depth limit): *Adercotryma glomeratum, Alabaminella weddellensis, Bathysiphon arenacea, Dentalina spirostriolata, Dorothia pauperata, Laticarinina pauperata, Melonis affinis, Melonis pompilioides, Parrelloides bradyi, Sigmella edwardsi, Uvigerina bradyana, Uvigerina hispida,* and *Valvulineria javana;* and

Lower bathyal (2000–4000 m; upper depth limit): *Cyclammina cancellata, Ehrenbergina hystrix, Favocassidulina favus, Globocassidulina crassa, Laevidentalina communis,* and *Nuttallides umbonifera* (dominant below the lysocline).

Samples used for the study of benthic foraminifers were the same as those for planktonic foraminifers; therefore, the initial processing was the same—wet sieving on a 63-µm screen. For selected samples throughout the cored section, faunal reference slides were made, particularly in areas of lithologic and/or assemblage changes.

PALEOMAGNETISM

Paleomagnetic work conducted during ODP Leg 180 consisted of (1) long-core measurements of the remanent magnetization (RM) of archive-half core sections before and after alternating field (AF) demagnetization, (2) magnetic remanence measurements on discrete samples collected from the working half of core sections, (3) mean magnetic susceptibility measurement of whole- and half-core sections and of discrete samples, and (4) anisotropy of magnetic susceptibility measurement of discrete samples.

Instrumentation

Long-core remanence measurements and AF demagnetization were performed using an automated pass-through cryogenic direct current superconducting quantum interface device (DC-SQUID) magnetometer (2G Enterprises Model 760-R) with an in-line AF demagnetizer (2G Enterprises Model 2G-600) capable of reaching peak fields of 80 mT with a 200-Hz frequency. The background noise level of the magnetometer is on the order of ~10^{-10} A·m^2. The large volume of core material within the sensing region of the magnetometer, which is on the order of 100 cm^3, permits the measurement of cores with remanent intensities as weak as ~10^{-5} A·m^{-1}.

The AF demagnetization of discrete samples to peak fields of 30 mT was achieved by using the in-line demagnetizer installed on the pass-through cryogenic magnetometer.

Magnetic susceptibility was measured for all whole-core sections as part of the MST analysis (see **"Physical Properties,"** p. 28). Raw data values were stored in the JANUS database in units of 10^{-5} SI. To convert to true SI volume susceptibilities, raw values should be multiplied by a correction factor to account for the volume of material that passed through the susceptibility coils. The correction factor for a standard ODP core is about 0.66 (= 1/1.5). Figures illustrating magnetic susceptibilities in the "Paleomagnetism" sections in this report have not been volume corrected (refer to **"Magnetic Susceptibility,"** p. 29, for the appropriate correction and for equipment details).

Point susceptibilities were measured for most archive-half core sections as part of the AMST analysis. The AMST susceptibility meter (a Bartington Model MS2 with an MS2F probe having a tip diameter of 15 mm; spatial resolution = ~20 mm; operating frequency = 580 Hz) was set on SI units, with one measurement (period = 2 s) taken every 5 cm. Raw data values are stored in units of 10^{-5} SI on the accompanying Lamont Doherty Earth Observatory (LDEO) CD-ROM and in the ODP database.

Measurements of susceptibility and its anisotropy (AMS) for discrete samples used a Geofyzika Brno Kappabridge KLY-2 magnetic susceptibility meter. Experiments of the acquisition of isothermal remanent magnetization (IRM) were made using an ASC Impulse Magnetizer Model IM-10, which imparts short-term fields ranging from 0.02 to 1.0 T. Experiments of anhysteretic remanent magnetization (ARM) were made using a DTECH Partial Anhysteretic Remanent Magnetizer in conjunction with a Schonstedt GSD-1 AF demagnetizer. A direct current (DC) field of 0.05 T was applied in a peak alternating current (AC) field of 100 mT. Data are stored on the accompanying LDEO CD-ROM and are available from the ODP data librarian.

Sampling

For the shipboard study, oriented discrete samples were taken from working halves of most cores, generally at two samples per core.

For postcruise studies, oriented discrete samples were collected from working halves of APC-drilled cores at a frequency of one sample per section with occasional additional samples taken as needed from horizons of special interest. Intervals of drilling-related core deformation or other disturbance were avoided. High-resolution sampling for postcruise studies consisted of one 5-cm³ plug every 10 cm in the upper 2 m, followed by one 5-cm³ plug per section to 20 mbsf from Holes 1109A, 1110A, 1115A, and 1115B. At Hole 1109C, two 5-cm³ plugs were taken at the same frequency as at the other holes.

Oriented sediment samples were collected in 8-cm³ plastic cubes with an arrow on the bottom pointing upcore. Two different sampling methods were used: (1) very soft intervals were sampled by pushing the plastic cube directly into the sediment; and (2) stiffer intervals were sampled using an extruder. These two sampling methods yielded a 180° difference in the orientations of both the +X and +Y axes relative to the standard "up" arrow (the -Z direction) drawn on the bottom of the sample box (Fig. **F13**).

Minicores, having a diameter of 2.5 cm and a length of 2.2 cm with an approximate volume of 11 cm³, were drilled from working halves of indurated rocks using a water-cooled drill press. Cubes with a dimension of ~2 cm × 2 cm × 2 cm were cut from smaller pieces using a diamond-bladed saw. Minicores and cut cubes were oriented by indicating the upcore and +Y directions on the sample surface corresponding to the split face of the working-half section.

The long-core cryogenic magnetometer was used to measure remanences of discrete samples selected for shipboard study; these were measured in a tray designed for seven samples. The data are shown in the "Paleomagnetism" sections of the individual site reports and are stored in the JANUS database. The remainder of the samples will be measured and analyzed onshore as part of postcruise studies.

F13. Coordinate system for working halves of core sections, **p. 64.**

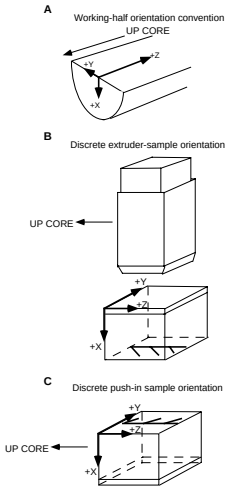

Core Orientation

Orientation of APC cores relative to magnetic north was achieved with a tensor tool mounted on the core barrel. The tensor tool consists of a three-component fluxgate magnetometer and a three-component accelerometer rigidly attached to the core barrel. Information from both sets of sensors allows the azimuth and dip of the hole to be measured, as well as the azimuth of the double-line orientation mark (+X direction) on the core liner. Orientation is not usually attempted for the top two to three cores (about 20–30 mbsf) until the bottom-hole assembly is sufficiently stabilized in the sediment. The XCB- and RCB-drilled cores were not oriented using the tensor tool. Tensor data are stored in the JANUS database.

Methods

Archive halves of all core sections were measured unless precluded by drilling-related deformation. Time constraints controlled the number of demagnetization steps applied to each core section. Cores were AF demagnetized at two to five steps ranging between 5 and 30 mT. False apparent low intensities and inaccurate directions occur where the wide

response function (maximum signal occurs within 10 cm on either side of the SQUID sensors) averages empty space with the core signal. Consequently, measurements within 15 cm of the ends of each section, which have been compromised by an edge effect, were omitted. Core photographs and laboratory notes were examined in order to delete data from disturbed or missing intervals. The raw data are archived in the ODP database.

Discrete sediment samples were placed into the tray such that +X and +Y were oriented parallel to the SQUID orientations (i.e., +X up, +Y to starboard, +Z into the cryogenic magnetometer). The AF demagnetization was applied at six steps ranging between 2 and 25 mT. Data were corrected for tilt where information was available.

The AMS measurement of discrete samples involved 15 oriented measurements for each sample. Acceptable data from measurements had a standard error of less than 3%. Susceptibility parameters were calculated according to Jelinek (1981).

Magnetostratigraphy

All sediment cores were affected to some extent by a steep, vertically downward-pointing overprint attributed to the drill string. Some cores also showed a radially inward overprint manifested as declinations of 0° along the entire length of a section.

Where magnetic cleaning successfully isolated the characteristic component of remanence, paleomagnetic directions and intensities were used to define the polarity. The revised time scale of Cande and Kent (1995), as presented in Berggren et al. (1995a), was used as a reference for the ages of Cenozoic polarity chrons.

INORGANIC GEOCHEMISTRY

Interstitial Water Sampling and Geochemistry

The inorganic geochemistry program during Leg 180 was designed to identify the various geochemical reactions taking place throughout key lithologic sections. The bulk of the shipboard inorganic geochemistry focused on the analysis of squeezed IW to identify major changes in the composition of the sediments and the water/rock interactions therein.

Shipboard IW analyses were performed on waters extracted from 5- to 15-cm-long whole-round sections that were cut immediately after core retrieval on deck. Specific details of the sampling resolution are described in the individual site chapters. After extrusion from the core liner, the outer few millimeters of each whole round were carefully removed with a clean spatula to minimize potential contamination. Interstitial waters were collected using a titanium squeezer, modified after the standard ODP stainless steel squeezer of Manheim and Sayles (1974), to provide contamination-free IW samples. Scraped excess material was saved and archived for any future potential research needs. After loading the squeezer, pore water was extruded through Whatman No. 1 filters fitted on a titanium screen by applying pressures up to 40,000 lb (~4150 psi) with a hydraulic press.

The IW samples were double filtered. IW was collected through 0.45-µm Gelman polysulfone disposable filters into scrupulously cleaned (acid washed with 10% volume/volume [v/v] HCl or HNO_3) 50-mL plastic syringes. The IW was subsequently refiltered through

0.45-µm Gelman polysulfone disposable filters as needed. Trace element splits for postcruise shore-based research were subsequently processed under "clean conditions" in a Class 100 laminar flow hood, filtered through acid-washed 0.22-µm Gelman polysulfone disposable filters, and acidified with 100 µL of double quartz distilled 8.7 N HNO_3 per 25 mL of IW. Samples for postcruise isotopic analyses were heat sealed in glass vials. Samples for shipboard work were stored in plastic vials before analysis.

In the deeper portions of the core, where IW sampling became more difficult because of lithification of the sediments, larger whole-round samples were selected from what appeared to be the softer portions of the core. These samples were placed inside several plastic bags and crushed with a hammer. The crushed sample was then squeezed in the normal manner described above. This procedure was previously used during Leg 166 and found to yield a much greater volume of pore water than obtainable by simply squeezing the original whole-round material (Leg 166, Shipboard Scientific Party, 1997).

The IW samples were routinely analyzed for salinity as total dissolved solids in grams per kilogram with a Goldberg optical handheld Reichart refractometer. The alkalinity was measured by Gran titration with a Brinkmann pH electrode and a Metrohm autotitrator. The pH was measured on the National Bureau of Standards (NBS) scale as part of the alkalinity titration. It should be noted that pH measurements obtained in this fashion are not always reliable given that the algorithm employed for pH measurement before the start of the alkalinity titration is adversely affected by degassing.

Dissolved chloride was determined by titration and by ion chromatography (IC; see paragraph below). Dissolved SiO_2 and NH_4^+ were determined by spectrophotometric methods with a Milton Roy Spectronic 301 spectrophotometer (Gieskes et al., 1991). The standard deviations of the analyses described above are as follows: alkalinity = <1.5%; chloride = <0.5%; and SiO_2 and NH_4^+ = ~3%.

Sodium, potassium, magnesium, calcium, chloride, and sulfate were analyzed by IC using a Dionex DX-100 automated system equipped with an autosampler. Typical 1-σ standard deviations were as follows: potassium = <6%; magnesium and calcium = <3%; sulfate = <4%; and sodium = <5%. Chloride measurements by IC, which are often systematically higher by ~3%–5% than those obtained by titration, were more accurate with the new IC installed at the beginning of Leg 180. Titrations were routinely performed to compare results obtained by the two techniques except in IW from Site 1108. Dissolved Cl^- measurements made by $AgNO_3$ titration are still better constrained than those by IC and are deemed more reliable. Excursions were observed to occur in Cl^- data from IC on a run-by-run basis, with notable divergence of the titration and IC data observed in the first 150 mbsf of Site 1109 (see Fig. **F70A,** p. 162, in the "Site 1109" chapter).

Lithium and strontium concentrations were quantified using flame atomic emission spectrometry (AES) and atomic absorption spectrometry (AAS) on a Varian SpectrAA-20. Tenfold dilutions of the IW were used for lithium and five- to twentyfold dilutions were employed for strontium analyses. Air-acetylene (Li) and nitrous oxide–acetylene (Sr) flames were utilized for these analyses. Standards for all flame AAS/AES techniques were matrix matched as closely as possible to samples (Li and Sr). Matrix matching is particularly important for Li determinations, because large variations in salinity and matrix composition of the

IW result in interferences that lead to erroneously high Li concentrations (E. De Carlo and P. Kramer, unpubl. data). A more detailed description of analytical methods and standards used can be found in ODP Technical Note 15 (Gieskes et al., 1991). The 1-σ standard deviations were <2% for lithium and ~3%–4% for strontium.

ORGANIC GEOCHEMISTRY

The shipboard organic geochemistry program for Leg 180 included (1) real time monitoring of volatile hydrocarbons as required by ODP safety regulations; (2) measurement of inorganic carbon and carbonate content of the sediments; and (3) elemental analyses of total nitrogen, sulfur, and carbon. All methods and instruments used during Leg 180 are described in detail by Emeis and Kvenvolden (1986), Kvenvolden and McDonald (1986), and in the "Explanatory Notes" chapter of the Leg 156 *Initial Reports* volume (Shipboard Scientific Party, 1995b).

Volatile Hydrocarbons

For safety and pollution prevention, concentrations and distribution of light hydrocarbon gases, mainly methane (C_1), ethane (C_2), and propane (C_3), were monitored for each core following the standard headspace sampling method described by Kvenvolden and McDonald (1986). A 5-cm^3 sediment sample was collected using a calibrated borer tool while the core was still on deck. The sample was placed in a 21.5-cm^3 glass serum vial and sealed with a septum and metal crimp cap. When consolidated or lithified samples were encountered, chips of material were placed in the vial and sealed. Before gas analyses, the vial was heated to 60°C for 30 min. A 5-cm^3 subsample of the headspace gas was extracted from each vial using a standard glass syringe for gas chromatography (GC) analysis. When gas pockets were encountered, vacutainer samples were collected by penetrating the liner using a syringe connected to a penetration tool.

The constituents of the gas were analyzed using a HP5890 II gas chromatograph equipped with a 8 ft × ⅛ in stainless steel column packed with HayeSep 5 and a flame ionization detector (FID). When heavier molecular-weight hydrocarbons (C_3) and above were detected, the sample was analyzed by a natural gas analyzer (NGA) used to quantify C_1 to C_6, nitrogen, oxygen, and carbon dioxide. Helium was used as the carrier gas. Data acquisition and processing were performed by a HP Chemstation. Chromatographic response was calibrated against authentic standards and the results reported as parts per million by volume (ppmv).

Inorganic Carbon

Inorganic carbon was determined using a Coulometrics 5011 carbon dioxide coulometer equipped with a System 140 carbonate carbon analyzer. Samples of 10–12 mg of freeze-dried ground sediment were weighed and then reacted with 2M HCl to liberate CO_2. The CO_2 was titrated and the change in light transmittance monitored by a photo detection cell. The weight percentage of calcium carbonate was calculated from the inorganic carbon content, assuming that all the CO_2

evolved was derived from dissolution of calcium carbonate by the following equation:

$$wt\%CaCO_3 = wt\%IC \text{ (inorganic carbon)} \times 8.33.$$

The amount of carbonate is expressed as weight percent (wt%), assuming all the carbonate was present as calcite. No correction was made for other carbonate minerals.

Elemental Analysis

Total carbon, nitrogen, and sulfur were analyzed using a Carlo Erba 1500 CNS Analyzer. An aliquot of 12–15 mg freeze-dried ground sediment with a V_2O_5 catalyst was combusted at 1000°C in a stream of oxygen. Nitrogen oxides were reduced to N_2. The mixture of N_2, CO_2, and SO_2 gases was separated by gas chromatography and detection was performed by a thermal conductivity detector (TCD). All measurements were calibrated by comparison to synthetic standards. The amount of total organic carbon (TOC) was calculated as the difference between total carbon (TC) and inorganic carbon (IC), i.e.,

$$wt\%TOC = wt\%TC - wt\%IC.$$

MICROBIOLOGY

Bacteria play a dominant role in the degradation of organic matter within sediments and, as a consequence, drive chemical changes and early diagenesis. The existence of a deep bacterial biosphere in marine sediments has only recently been established (Parkes et al., 1994), but already the activity of bacteria in depths to 750 mbsf and their direct involvement in geochemical changes have been demonstrated.

Recent research (Wellsbury et al., 1997) has shown that temperature increases during burial can result in organic matter becoming easier to degrade by bacteria, and that bacterial populations and their activity can increase in deeper layers below 100 m. Increasing organic matter bioavailability was reflected in increases up to a thousandfold in substrates for bacterial activity (volatile fatty acids, particularly acetate) in deep sediments (Leg 164; Paull, Matsumoto, Wallace, et al., 1996b). Thus, bacterial populations should exist at much greater depths and may even increase with depth rather than decrease as the energy sources "improve" with increasing depth and temperature.

This work aims to determine the bacterial mechanisms involved in, and the impact these have on, the modification of deeply buried organic matter. Leg 180 also provided the deepest samples yet collected for bacterial analysis.

Sediment Sampling for Microbiological Analysis

Two types of samples were taken for microbiological analysis:

1. Sediment in 1-cm^3 samples was taken for direct microscopic determination of bacterial numbers. The samples were taken from the end of selected 1.5-m core sections immediately after the sections were cut on the catwalk and before the sections were sealed

with an end cap. Potentially contaminated sediment was first removed using a sterile scalpel. Then, using a sterile 5-cm^3 plastic syringe with the luer end removed, a 1-cm^3 minicore sample was taken and sealed with a sterile suba-seal stopper. In a clean area of the laboratory, the 1-cm^3 sample was extruded into a sterile serum vial containing 9 mL of filter-sterilized (0.2 µm) 4% formaldehyde in artificial seawater. The vial was crimped and shaken vigorously to disperse the sediment particles and then stored at 4°C.

2. Whole-round core samples were taken and stored intact for shore-based laboratory analysis. These were cut from 1.5-m core sections on which the end caps had not been sealed with acetone. The core sections were removed from the catwalk and brought into the core reception area, where they were cleaned, wiped with ethanol, and placed into a sterile cutting rig (Cragg et al., 1992) flushed constantly with sterile oxygen-free nitrogen (OFN) to maintain anoxia. Sterile whole-round core samples were taken adjacent to the whole-round cores for IW sampling and organic geochemical analysis. One end of the whole-round core was cut with a sterile hacksaw blade, removed from the rig, and immediately capped with a sterile core end cap while being flushed with sterile OFN from a gassing jet. The core end cap was then taped to the liner. The cutting rig was cleaned, alcohol washed, and heat sterilized, and the process was repeated with the other end of the whole-round core. Once fitted with end caps, cores were sealed in a gas-tight laminated plastic/aluminum bag containing a chemical oxygen scrubber (Anaerocult A, Merck-BDH) to produce anaerobic conditions. Sealed, anaerobic core sections were stored at 4°C before analysis onshore.

Laboratory Handling Determination of Total Bacterial Populations

Total bacterial numbers and numbers of dividing and divided cells were determined using acridine orange as a fluorochrome dye with epifluorescence microscopy (Fry, 1988). Fixed samples were mixed thoroughly, and a 5- to 10-µL subsample was added to 10 mL of 2% (v/v) filter-sterilized (0.2 µm) formaldehyde in artificial seawater containing 2% (v/v) acetic acid to dissolve excess carbonate. Acridine orange (50 µL of a 5-$g \cdot L^{-1}$ filter-sterilized (0.1 µm) stock solution) was added and the sample was incubated for 3 min. Stained cells and sediment were trapped on a 0.2-µm black polycarbonate membrane (Costar, High Wycombe, United Kingdom). Excess dye was removed from the membrane by rinsing with an additional 10 mL of 2% (v/v) filter-sterilized formaldehyde in artificial seawater containing 2% (v/v) acetic acid, and the membrane was mounted for microscopic analysis in a minimum of paraffin oil under a coverslip. At least three membranes were prepared for each sample: where 95% confidence limits of the mean count exceeded 0.5 log10 units, further replicate filters were prepared. A minimum of 200 fields of view were counted.

The mounted membrane filters were viewed under incident illumination with a Zeiss Axioskop microscope fitted with a 50-W mercury vapor lamp, a wide-band interference filter set for blue excitation, a 100× (numerical aperture = 1.3) Plan Neofluar objective lens, and 10× eyepieces. Bacterially shaped fluorescing objects were enumerated, with the numbers of cells on particles doubled in the final calculations to

account for masking. Dividing cells (those with a clear invagination) and divided cells (pairs of cells of identical morphology) were also counted. The detection limit for bacterial cells is ~1 × 10^5 cells/cm^3 (Cragg, 1994).

PHYSICAL PROPERTIES

Introduction

Physical properties were measured on unsplit cores and on the undisturbed parts of split cores. The MST was used for nondestructive measurements of wet bulk density, compressional wave velocity, magnetic susceptibility, and natural gamma radiation in unsplit cores. Thermal conductivity measurements were also conducted on unsplit sediment cores and split rock cores. Undrained shear strength and/or unconfined compressive strength tests were performed on split sediment cores, and three-directional compressional wave velocities were measured on both sediment and rock cores. Portions of split cores that were undisturbed by drilling and sampling, gas expansion, bioturbation, cracking, and large voids were used to obtain specimens for index properties measurements (wet bulk density, grain density, dry bulk density, water content, void ratio, and porosity).

Physical properties measurements during Leg 180 were used to obtain (1) near-continuous records for hole-to-hole correlation, construction of complete stratigraphic sequences, and downhole log calibration; (2) sediment properties related to composition and consolidation history, such as porosity, natural gamma radiation, magnetic susceptibility, and shear strength to help constrain the location of unconformities, sediment fracturing, and fluid migration and expulsion; (3) estimates of rock and fracture properties in order to constrain paleo- and contemporary-fault movements, stress orientation, and fluid migration and expulsion; and (4) data for the calculation of synthetic seismograms, such as compressional wave velocity and bulk density, and for the calculation of local heat flow (i.e., thermal conductivity). A graphical representation of the physical properties procedures adopted for Leg 180 is flow-charted in Figure **F14.**

F14. Sequence of physical properties measurements, **p. 65.**

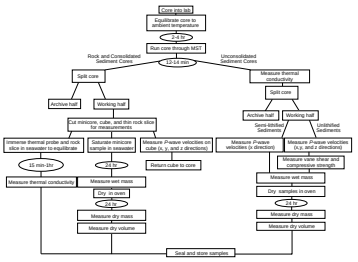

All physical properties measurements were conducted after the cores had equilibrated to ambient room temperature (i.e., 22°–24°C) ~2–4 hr after recovery. The first measurement station was the MST, which combines four sensors on an automated track to measure magnetic susceptibility, bulk density, compressional wave velocity, and natural gamma-ray emission on whole-core sections. The respective sensors are the magnetic susceptibility meter (MSM), the gamma-ray attenuation porosity evaluator (GRAPE), the *P*-wave logger (PWL), and the natural gamma-ray (NGR) detector. The MST measurement intervals and periods for each 1.5-m core section were selected so that the physical properties could be accurately characterized in 12–14 min without hindering the flow of core processing in the laboratory. Sediment cores were split into archive and working halves immediately following thermal conductivity measurements on the whole sediment core. However, the rock cores were split prior to thermal measurements and each measurement was conducted on the half core.

The working half of each unconsolidated sediment and rock section was used for further physical properties measurements. For the unconsolidated sediment sections, *P*-wave velocity, undrained vane shear

strength and/or compressive strength, and water content and grain density were measured. For the rock sections, *P*-wave velocity, water content, and grain density were measured. Water content and grain density were used to calculate bulk density, porosity, and related parameters. A summary of each of the physical properties measurement procedures for Leg 180 is outlined in the paragraphs below. Refer also to the physical properties handbook (Blum, 1997) for a description of the physical principles underlying the sampling methods.

Multisensor Track Measurements

Magnetic susceptibility, bulk density, and natural gamma-ray emission were generally measured on all cores indiscriminate of collection method, (i.e., APC, XCB, and RCB). The *P*-wave velocities were measured on all APC-cored intervals and some XCB- and RCB-cored intervals. Measuring *P*-wave velocities on XCB and RCB cores is not usually recommended because of the likelihood of discontinuous coring and/or a loss of coupling between the liner and the core. However, high frequency of *P*-wave measurements on XCB and RCB cores was deemed necessary for the earlier sites during Leg 180 to provide a backup data set in the event that logging could not be conducted in unstable boreholes.

In order to collect measurements, individual, unsplit core sections were placed on the MST, which automatically moves the core section through the four sensors on a fiberglass track. The MST data are not always continuous as a function of depth because of the removal of whole-round sections immediately after coring. For those sections cored through XCB and RCB methods, the presence of overcompacted, discontinuous core (biscuits) was noted and subsequently cross-correlated with core descriptions. Upon encountering highly fractured hard rock intervals, whether to carry out MST measurements was decided on a core-by-core basis.

Magnetic Susceptibility

Magnetic susceptibility is used mostly as a proxy for changes in composition that can be linked to depositional cycles. The high precision and sensitivity of susceptibility logs makes this measurement extremely useful for core-to-core and core-downhole log correlation. The magnetic susceptibility was measured with a Bartington meter MS2 using an 80-mm internal diameter sensor loop (88-mm coil diameter) operating at a frequency of 565 Hz and an AF of 80 $A \cdot m^{-1}$ (0.1 mT) and set on SI units. The sensitivity range was set to the low sensitivity setting (1.0 Hz). The sample period and interval were set to 4 s and 4 cm, respectively. The raw mean value of the measurements was calculated and stored automatically in units of 10^{-5} SI. The quality of these results degrades in XCB and RCB sections, where the core may be undersized and/or disturbed. Nevertheless, the general downhole trends are useful for stratigraphic correlations. The MS2 meter measures relative susceptibilities, which need to be corrected for volume variations. For core (d) and coil (D) diameters of 66 and 88 mm, respectively, the corresponding correction factor for d/D is 1.48 (Blum, 1997; page 38). During data reduction, it is necessary to convert the relative susceptibility to the volume-normalized magnetic susceptibility by multiplying by 1/1.48 or 0.68. All magnetic susceptibility data presented in the "Physical Properties" figures have been volume normalized.

Bulk Density and Porosity

Bulk density was estimated for unsplit core sections as they passed through the GRAPE, using a sampling period of 4 s every 4 cm on the MST. The gamma-ray source was ^{137}Cs. For each site the GRAPE bulk densities and the bulk densities measured on discrete samples were compared for repeatability.

Compressional Wave (*P*-wave) Velocity

The *P*-wave velocity was measured at 4-cm intervals for 4-s periods with the high-resolution *P*-wave logger (PWL) mounted on the MST. The PWL measures *P*-wave velocity across the unsplit core sections. To determine the *P*-wave velocity, the PWL transmits 500-kHz compressional wave pulses through the core at a frequency of 1 kHz. The transmitting and receiving transducers are aligned perpendicular to the core axis while a pair of displacement transducers monitor the separation between the compressional wave transducers. Variations in the outer diameter of the liner do not degrade the accuracy of the velocities, but the unconsolidated sediment or rock core must completely fill the liner for the PWL to provide accurate results.

Natural Gamma Ray

Natural gamma-ray emissions are a function of the random and discrete decay of radioactive atoms and are measured with scintillating detectors as outlined by Hoppie et al. (1994). During Leg 180, NGR emissions were measured using observation periods suitable for the predicted radioactivity of the recovered core. For those cores believed to contain low radioactive (i.e., carbonate-rich) sediments, NGR was measured for 28 s per each 14-cm length of core, and for non-carbonate cores, NGR was measured for 20 s per each 10-cm length of core. If the carbonate content could not be predicted, the longer sampling period was selected as a default. The NGR calibration was performed at the beginning of the leg, and sample standards were run for instrument accuracy between each site.

Thermal Conductivity

Thermal conductivity was measured during Leg 180 using the TK04 system described by Blum (1997). This systems employs a single-needle probe (von Herzen and Maxwell, 1959) heated continuously in "full-space configuration" for soft sediments and in "half-space configuration" for hard rock. Under conditions of moderate to full recovery, thermal conductivity measurements were conducted at a minimum frequency of one every other section and at increased frequencies when time allowed. When recovery was limited, a minimum of one thermal conductivity measurement per core was obtained.

Full-core unconsolidated sediment sections were measured for thermal conductivity using a full-space single-probe TeKa (Berlin) TK04 unit. An aperture was drilled in the outer core liner and the 2-mm temperature probe was inserted into the working half of the core section. Half-core rock specimens were measured for thermal conductivity using the half-space configuration. The needle probe was secured onto the flat surface of the half core. Good coupling with the needle probes was ensured by flattening and smoothing the core surface with carbide grit

sandpaper. The samples and needles were then immersed in seawater. This procedure has been used since ODP Leg 140 (Shipboard Scientific Party, 1992c), with the TK04 unit first being used for hard-rock thermal conductivity measurements during ODP Leg 169 (Shipboard Scientific Party, 1998b).

At the beginning of each half-space and full-space measurement, temperatures in the samples were monitored automatically, without applying a heater current until the background thermal drift was determined to be less than 0.04°C/min. The heater circuit was then closed and the temperature increase in the probe was recorded. This technique proved highly sensitive to small variations in ambient temperature. To account for the sensitivity, core samples and monitor needles were equilibrated to a constant temperature by immersion in a seawater bath for 15 min to 1 hr before measurements. Immersion in seawater kept the samples saturated, improved the thermal contact between the needle and the sample, and reduced thermal drift during the tests.

The reported thermal conductivity measurement for each sample was the average of three repeated measurements for the full-space method and four repetitions for the half-space method. Under conditions where it was necessary to expedite core processing, the thermal conductivity repetitions were truncated after the second measurement if the first two measurements differed by 1% or less.

Data are reported in $W \cdot m^{-1} \cdot °C^{-1}$ with a stated error of about 5%. Choice of measurement interval and assessment of thermal stability are automatic with the TK04 meter, which does not require shipboard calibration.

Index Properties Measurements

Moisture and density (MAD) measurements (water content, wet and dry bulk density, and grain density) were routinely measured using ~10-cm^3 specimens from the split cores. Other related properties, such as porosity and void ratio, were calculated from phase-relation equations. Samples for MAD measurements were collected at a frequency of one per section. However, the sampling frequency was either increased as needed to characterize all significant lithologies throughout the cores or decreased for homogeneous sections. In XCB cores, which frequently showed a biscuiting type of disturbance, particular care was taken to sample undisturbed parts of the core and to avoid drilling slurry. Immediately after the samples were collected, wet sediment mass (M_{wet}) was measured. Dry sediment mass (M_{dry}) and dry sediment volume (V_{dry}) were determined after the samples had dried in a convection oven for 24 hr at a temperature of 105° ± 5°C. Wet sediment volume (V_{wet}) was not measured.

The calculation of index properties was derived from both predetermined parameters and measurements collected during the MAD procedure. Below is a discussion of the parameters and equations used to calculate the index properties.

Parameter Descriptions

The mass of salt (M_{salt}) in the sample is given by:

$$M_{salt} = [s/(1 - s)] \times M_{water},$$

where s is the assumed saltwater salinity (0.035) corresponding to a pore-water density (ρ_{pw}) of 1.024 g·cm^{-3} and a salt density (ρ_{salt}) of 2.257 g·cm^3. The corrected mass of pore water (M_{pw}), volume of pore water (V_{pw}), mass of solids excluding salt (M_{solid}), volume of salt (V_{salt}), and volume of solids excluding salt (V_{solid}) are, respectively

$$M_{pw} = M_{water} + M_{salt} = M_{water}/(1 - s),$$

$$V_{pw} = M_{pw}/\rho_{pw},$$

$$M_{solid} = M_{dry} - M_{salt},$$

$$V_{salt} = M_{salt}/\rho_{salt},$$

and

$$V_{solid} = V_{dry} - V_{salt} = V_{dry} - M_{salt}/\rho_{salt},$$

where M_{dry} and V_{dry} are the dry mass and volume, respectively.

Water Content

Wet water content (w_{wet}) is expressed as the ratio of the mass of pore water to the wet sediment (total) mass, and the dry water content (w_{dry}) is the ratio of the mass of pore water to the mass of solids (excluding salt; ASTM Standard D 2216-80; ASTM, 1980):

$$w_{wet} = M_{pw}/M_{wet}$$

and

$$w_{dry} = M_{pw}/M_{dry}.$$

Wet and Dry Bulk Densities

Wet bulk density (ρ_{wet}) was calculated from

$$\rho_{wet} = M_{wet}/V_{wet}.$$

Dry bulk density (ρ_{dry}) is used to estimate the mass accumulation rate for a given depth interval and is defined by

$$\rho_{dry} = M_{dry}/V_{dry}.$$

Grain Density

Sediment grain (solid) density (ρ_{solid}) was calculated from

$$\rho_{solid} = M_{solid}/V_{solid}.$$

Porosity and Void Ratio

Porosity (η) and void ratio (e) were determined assuming that all original sediment voids (V_{voids}) were filled with pore water. Porosity and void ratio were, respectively, calculated from

$$\eta = V_{voids}/V_{wet}$$

and

$$e = V_{voids}/V_{solid}\,.$$

P-wave Velocities on Split Cores

The chosen method for compressional wave velocity measurements (V_P) was dependent on the degree of sediment consolidation. For unconsolidated sediments, the PWS1 and PWS2 insertion probe system was used to measure the transverse and longitudinal (i.e., along the core axis) *P*-wave velocity. In semilithified sediments and rock cores, the PWS3 contact probe system, described by Boyce (1976), was employed. The hard-rock measurements were made on ~10-cm^3 cubes cut perpendicular to the axis of the core at room temperature and pressure.

The PWS1 and PWS2 probe system calculates *P*-wave velocity based on a fixed distance and measured traveltime. Anisotropy was calculated using the following equation:

$$\text{Anisotropy (\%)} = (V_{Pt} - V_{Pl})/[(V_{Pt} + V_{Pl})/2] \times 100,$$

where V_{Pt} is the transverse compressional wave velocity and V_{Pl} is the longitudinal velocity. The velocity meter was calibrated by measuring V_P in water.

In addition to traveltime, the PWS3 system measures variable sample thickness with a digital micrometer. Measurements were generally taken once per section, with more measurements taken in sections characterized by varying lithology. In cores that were too consolidated for the PWS1 and PWS2 insertion probes, but too soft or friable to cut into cubes, the PWS3 system was used to measure *P*-wave velocity in the x direction. In hard rock, cubes were oriented, cut, and then rotated so that the PSW3 could measure velocities in the X, Y, and Z directions.

Shear and Compressional Strength

Undrained shear strength (S_u) was estimated using a motorized miniature vane shear apparatus that was inserted into soft sediment and rotated until the sediment failed, following the ASTM D 4648-87 procedure (ASTM, 1987). Difference in rotational strain between the top and bottom of the vane shear spring is measured digitally and the peak shear strength is recorded. Shear strength measurements by this apparatus are reliable up to a threshold of 100–150 kPa.

A pocket penetrometer was used to measure unconfined compressive strength in stiffer sediments. The penetrometer is a small, flat-footed, cylindrical probe that is pushed ~6.5 mm vertically into the split-core surface; the measured resistance (in kg·cm^{-2}) is the unconfined compressive strength, or 2 S_u. The values of unconfined compression were converted to values of S_u and reported in units of kPa. The maximum strength that can be measured with the pocket penetrometer is 225 kPa. Both vane shear and pocket penetrometer measurements were performed on each section in regions where the S_u values ranged between 100 and 150 kPa.

DOWNHOLE MEASUREMENTS

Introduction

After coring was completed, combinations of sensors were lowered downhole to measure the physical and chemical properties of formations penetrated by the borehole. Interpretation of these continuous in situ measurements can yield a lithostratigraphic, structural, geophysical, and geochemical characterization of the hole. The downhole tools run during Leg 180 are listed in Table T7; they were combined as represented in Figure F15 and described below.

1. The Schlumberger "triple combo" is made of the hostile environment natural gamma-ray sonde (HNGS), the accelerator porosity sonde (APS), the hostile environment lithodensity sonde (HLDS), the dual induction tool (DIT), and the LDEO temperature logging tool (TLT).
2. The Formation MicroScanner (FMS) sonic combination includes the natural gamma-ray spectrometry tool (NGT), the array sonic digital tool (sonic digital cartridge [SDC], sonic logging receiver [SLR], sonic logging sonde [SLS-C]), and the FMS.
3. The ultrasonic borehole imager (UBI) string includes the NGT and the general purpose inclinometry tool (GPIT).
4. Vertical seismic profiling data are acquired by the well seismic tool (WST) in the open hole.

The natural gamma ray is acquired (by either HNGS or NGT) on all combinations to provide a common basis for depth correlations. The FMS and the UBI provide high-resolution continuous images of sedimentary or structural features and hole geometry, and help place the core pieces back in depth and orientation.

Throughout the acquisition of downhole measurements, data are transmitted to the surface by the seven-conductor logging cable, displayed in real time, and simultaneously recorded. The TLT is an exception to this because its data are recorded internally and downloaded after logging.

The logging data became quickly available aboard the ship and were depth shifted as explained in the site chapters to produce the logging section of each site report. Further processing conducted onshore includes a differential depth shift and yields the data included on the accompanying LDEO CD-ROM.

Table T8 lists the main measurements and their approximate vertical resolution and sampling interval, as well as their depth of investigation. These tools and their applications are briefly described in the following sections according to the physical properties they measure. More detailed information can be found in Hearst and Nelson (1985), Serra (1984), Timur and Toksöz (1985), Ellis (1987), and Schlumberger (1989).

T7. Logging tool strings and components, p. 74.

F15. Logging tool string combinations used on Leg 180, p. 66.

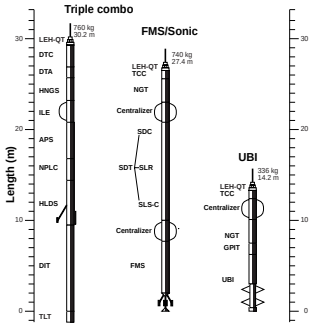

T8. Logging acronyms and measurements, p. 75.

Electrical Resistivity

Dual Induction Tool

The DIT provides three different measurements of electrical resistivity, each with a different depth of investigation. Two induction devices (deep and medium resistivity) send high-frequency alternating currents through transmitter coils, creating magnetic fields that induce second-

ary (Foucault) currents in the formation. These ground-loop currents produce new inductive signals proportional to the conductivity of the formation, which are recorded by the receiving coils. The third device (shallow resistivity) is the spherically focused resistivity that measures the current necessary to maintain a constant voltage drop across a fixed interval. This tool becomes inaccurate for formation resistivity exceeding 150 Ωm (error = >20% at 150 Ωm).

Interpretation

Bulk formation resistivity is mainly controlled by fluid resistivity and by porosity. To a first-order approximation, it responds to the inverse square root of porosity (Archie, 1942). Fluid resistivity depends mainly on water salinity and hydrocarbon content. Additional factors affecting resistivity include clay content, temperature, hydrous and metallic minerals concentration, presence of vesicles, and the geometry of interconnected pore spaces.

Sonic Velocity

The array sonic digital tool has three components. A sonic digital cartridge (SDC) hosts electronics. An SLS-C hosts two broadband (5–18 kHz) acoustic transmitters 2 ft (61 cm) apart and two receivers, 3 and 5 ft (91.4 and 152.4 cm), respectively, above the upper transmitter. An SLR hosts an array of eight receivers located 8–11.5 ft (243.8–350.5 cm) above the upper transmitter.

This setup allows recording of the full waveforms of sound waves that travel along the borehole wall over various source-receiver distances. Compressional wave velocity is determined in real time by a threshold-measuring technique that attempts to detect the first arrival. Occasionally, this technique fails, and either the threshold is exceeded by noise or the amplitude of the first compressional arrival is too small. The latter of these effects is known as cycle skipping and creates spurious spikes on the sonic log. Such problems may often be eliminated by reprocessing the data. Further processing of the full waveforms after logging may also determine shear and Stoneley wave velocities in relatively fast formations.

Compressional wave velocity is primarily controlled by porosity, matrix density, and elastic properties. In sedimentary rocks decreasing porosity and increasing lithification by diagenesis increases velocity.

Natural Gamma Ray

The NGT measures the natural gamma radiation of the formation by a scintillation detector (Lock and Hoyer, 1971). The gamma-ray energy spectrum is divided into five discrete windows, and count rates are recorded for each.

The more recent HNGS provides the same measurements with larger dual detectors of higher quality. The result is vastly improved statistical accuracy, as well as faster logging speed. This tool is additionally capable of high-temperature operation (up to 235°C), from which it derives its name.

Most natural gamma rays are emitted by the radioactive isotope ^{40}K and radioactive isotopes of the U and Th decay series, each at a characteristic energy level. Processing of the windowed counts therefore gives elemental abundances of K, U, and Th. Generally, K and Th are most

abundant in clays, and the uranium-corrected gamma-ray log (CGR, HCGR) can be used to estimate the clay content of the formation. This was not the case, however, in the Woodlark Basin, where sandy formations often correspond to high gamma-ray counts as described in the site chapters.

Density and Photoelectric Effect

The HLDS uses a chemical gamma-ray source (0.66 MeV, ^{137}Cs) to induce a back-scattered flux of gamma rays that is measured at fixed distances from the source. It also records a photoelectric effect (PEFL). The radioactive source and two detectors are located in a skid pressed against the borehole wall by a spring-loaded caliper arm.

Attenuation of these induced gamma rays is mainly caused by Compton scattering and is thus controlled by the density of electrons in the formation. Formation density (RHOM) is extrapolated by assuming that the atomic weight of most rock-forming elements is approximately twice the atomic number. This density is converted to density porosity (DPHI) using the formula

$$DPHI = (dm - RHOM)/(dm - dw),$$

where dw is the seawater density taken as 1.03 $g \cdot cm^{-3}$, and dm is the grain density taken as 2.71 $g \cdot cm^{-3}$, which corresponds to a limestone matrix.

Photoelectric absorption occurs at low energy levels (<150 keV) and depends on the energy of the incident gamma ray, the atomic cross section, and the nature of the atom. The PEFL measurement is almost independent of porosity and, therefore, can be used directly as a matrix lithology indicator.

Excessive roughness of the borehole wall allows drilling fluid between the skid and the formation and induces inaccuracy in the density measurement. Delta-rho (DRH) is a correction that attempts to compensate this effect; its magnitude is a good indicator of hole rugosity and measurement quality.

Neutron Porosity

The APS contains an accelerator that uses high voltage to produce 14-MeV fast neutrons from tritium. Five detectors then measure the population of formation-backscattered neutrons.

The neutrons must be reduced to the epithermal energy level (0.4–10 eV) by scattering before they can be detected. Because the scattering cross section for hydrogen is about 100 times larger than that of any other common element in the crust, most energy dissipation is related to hydrogen content. The measured neutron population is closely related to porosity because hydrogen occurs primarily in pore fluids. However, the log will overestimate porosity in hydrous minerals because hydrogen also occurs as bound water in hydrous minerals such as clay. There is also an effect caused by the borehole fluid, but it is minimized by using a bowspring to push the tool against the formation and by applying an empirical correction using caliper data. The theoretical vertical resolution is 0.25 m (Table T8), but it can be degraded by poor contact with the formation in enlarged boreholes.

When the neutrons reach thermal energy levels (0.025 eV) they are captured and absorbed by atomic nuclei such as hydrogen, chlorine, sil-

icon, and boron. Sigma (SIGF) is a measurement of the rate at which this absorption takes place; it is controlled primarily by the salinity of the formation fluid and the porosity.

Lithologic Analysis

The lithologic analysis primarily uses four measurements: natural gamma ray, neutron porosity, DPHI, and PEFL.

Generally, natural gamma-ray magnitude is proportional to clay content. However, the relationship between near-array porosity (APLC) and DPHI can also be used to examine clay content as described below, if it is certain that the formation does not contain significant amounts of dolomite.

Both porosity measurements, DPHI and APLC, are based on the assumption that the matrix is pure calcium carbonate. In this situation, both curves will read true porosity and will overlay perfectly. When the matrix is other than this, an error is induced on the output porosity. Fortunately, the induced errors act oppositely on the two curves. For instance, in a pure sand matrix DPHI will be too high and APLC will be too low, resulting in a total separation of about 0.05. In dolomite or clay, the effect is reversed; DPHI reads too low, whereas APLC reads too high. The separation in some clays can be as large as 0.40.

The PEFL measurement brings additional information. A pure limestone matrix reads about 5.2 barns/e^-, whereas a pure sandstone reads 1.8 barns/e^-. Clays tend to be intermediate, as are dolomites. The presence of iron-bearing minerals may cause the PEFL to spike to values as high as 17.

It should be noted that very few formations are pure enough in matrix to achieve the log responses described above. What typically appears on the log is a volumetric average of the constituents of the formation. Reconstructing the original volumes of these constituents is not just a tricky job—it's an art!

Electrical Images

The FMS was introduced by Schlumberger in 1986 to measure the electrical resistivity of the borehole with an array of sensors sufficiently dense to produce high-resolution borehole resistivity images (Ekstrom et al., 1986). Because ODP operations require logging tools to pass through drill pipe (3.8 in), a modified, smaller diameter tool was specifically designed by Schlumberger and introduced on ODP Leg 126 (Shipboard Scientific Party, 1990a, 1990b; Pezard et al., 1990). The FMS used in ODP has four orthogonal pads that are pressed against the borehole wall, each with an array of 16 electrodes. The electrode spacing, together with a vertical sampling distance of 2.5 mm and processing that corrects the offset rows to one level, yields a vertical and horizontal resolution of 5 mm. However, the size threshold of a detectable feature depends on the contrast in conductivity and can be on the order of microns. The 16 conductivity traces from one pad are displayed side by side to produce an image. The four images (one from each pad) typically cover only about 25% of the borehole. The coverage can sometimes be increased by running the tool twice, but both images may overlap in elliptical holes. Proper pad contact with the formation is ensured only in holes with diameter smaller than 37 cm. The electrode currents probe the conductivity of the rock to a depth of a few centimeters into the borehole wall; therefore, they respond to such variations in

physical and chemical properties of the rock as porosity or surface conduction when conductive clay minerals such as smectites are present.

Initial processing of the data into images was conducted aboard ship using proprietary Schlumberger GeoFrame software on a Sun workstation and included speed correction and depth shifting. Further processing and interpretation of the FMS images were performed postcruise and included a differential depth shift. Directional data that are recorded by the GPIT allow orientation of these images with respect to geographic north.

Applications of the FMS images include identification and mapping of fractures, faults, and bedding contacts, determination of strike and dip of structures, lithologic discrimination, detailed correlation of coring and logging depth, and orientation of cores (Serra, 1989; Pezard and Anderson, 1990; Pezard et al., 1992; MacLeod et al., 1992). The FMS can also be used to determine borehole geometry from the precise measurement of borehole diameter by its two orthogonal calipers.

Acoustic Images

The UBI, a Schlumberger evolutionary descendant of the borehole televiewer (BHTV; Zemanek, Caldwell, et al., 1970; Zemanek, Glenn, et al., 1970), produces an acoustic image of the borehole wall. The BHTV was first introduced to DSDP during Leg 83 (Newmark, Anderson, et al., 1985) but the UBI was first introduced to ODP during Leg 180. A focussing rotating transducer emits either 250- or 500-kHz ultrasonic pulses that are directed toward the borehole wall. Amplitude and traveltime of the reflected signals are then recorded either 140 or 180 times per rotation. The 7.5 revolutions per second allow upward movement of 3.6 $cm \cdot s^{-1}$ (logging speed of 130 m/hr) while sampling vertically every 5 mm. This, combined with a footprint of 4 mm (at 500 kHz) or 9 mm (at 250 kHz), allows the entire borehole wall to be scanned with a resolution of ~5 mm for hole diameters ~30 cm. Data are presented in the form of unwrapped images of the borehole wall both in amplitude and radius. Directional data recorded by the GPIT allow these images to be oriented geographically.

The amplitude of the reflected signal depends essentially on the roughness of the borehole wall, but also on the reflection coefficient of the fluid-rock interface, the position of the UBI tool in the borehole, and the shape of the borehole. Fractures or lithologic variations in the drilled rocks can easily be recognized in the amplitude image and thus help to reorient cores. The radial images give detailed information about the shape of the borehole and can be considered as very sophisticated caliper data. The radius data can thus be used to construct horizontal borehole cross sections. These data cover the borehole wall completely, whereas the FMS data cover the borehole wall only partially.

Borehole Inclination, Tool Orientation, and Total Magnetic Field

The GPIT, which is part of the FMS and UBI string, contains a three-component accelerometer from which the hole inclination (DEVI) and tool relative bearing (RB) are derived. The RB is the rotational orientation of the tool with respect to the high side of the hole. Additionally, the accelerometer data may be used to correct the log for irregular tool motion caused by sticking or ship heave.

The GPIT also contains a three-component magnetometer that measures the rotational orientation of the tool with respect to magnetic north (P1AZ). The local magnetic declination is entered in the logging software so that the images are oriented with respect to the geographic north. The P1AZ and RB measurements are combined to give the azimuth of a deviated hole (HAZI).

Borehole Geometry

Borehole geometry studies have become possible with the appearance of oriented orthogonal caliper measurements provided by the dipmeter (Cox, 1970; Babcock, 1978; Hottman et al., 1979; Schafer, 1980; Gough and Bell, 1981), the later FMS (Shamir et al., 1988; Shipboard Scientific Party, 1990b; Pezard et al., 1992), and the higher resolution measurements of the borehole televiewer (Zemanek, Caldwell, et al., 1970; Zemanek, Glenn, et al., 1970). These studies have often revealed borehole elongations that can have multiple origins (Beaudemont et al., 1988; Guenot, 1989; Dart and Zoback, 1989).

However, most attention during the last 20 yr has focused on the relationship between the anisotropy of the horizontal state of stress and a particular type of borehole elongation termed breakouts (Babcock, 1978).

Breakouts are characterized by seven conditions. They were defined by Babcock (1978) as zones (1) of elongation, where one diameter is significantly greater than the other (by at least 1 cm); (2) that begin and end abruptly; (3) that persist for a significant depth interval (larger than the pad height); (4) that slow or stop the natural clockwise rotation of the tool; and (5) where the smallest measured caliper is equal to the drill-bit size. Plumb and Hickman (1985) added that breakouts (6) are symmetrically elongated and (7) correspond to high electrical conductivity zones.

Breakouts are induced by remote anisotropic stress concentration around the borehole for three main reasons. First, the theoretical calculation of the state of stress around a circular hole in an elastic impervious medium (Kirsch, 1898; Hubbert and Willis, 1957; Hottman et al., 1979; Bell and Gough, 1979), a porous permeable medium (Haimson and Fairhurst, 1967) or a poroelastic medium (Detournay and Cheng, 1988) shows that the stress difference is greatest along the direction of the remote minimum horizontal principal stress, S_{Hmin}, which is the preferred site of shear failure initiation. Second, the orientation of breakouts remains consistent between different formations within a well and between wells on a basin scale. Third, the S_{Hmin} direction deduced from breakouts coincides with that deduced from other stress indicators, such as hydrofracture directions or large-scale geological features (Bell and Gough, 1979; Gough and Bell, 1981, 1982; Fordjor et al., 1983; Zoback et al., 1985; Hickman et al., 1985; Plumb and Hickman, 1985; Morin et al., 1989, 1990).

As a consequence, breakouts have been used to infer the remote direction of the minimum principal horizontal stress (Newmark et al., 1984; Newmark, Zoback, et al., 1985; Zoback et al., 1985; Hickman et al., 1985; Morin et al., 1989). Such an analysis, together with the packer hydrofracturing test, was a major component of the plan of Leg 180 toward characterizing the state of stress in the vicinity of an active normal fault.

Temperature Measurement

The LDEO TLT is a self-contained tool that was attached to the base of the Schlumberger triple combo. Data from a fast and a slow thermistor and a pressure gauge are collected every second and are recorded by an internal Tattletale computer. The Schlumberger Maxis unit wireline depth vs. time is recorded independently by a surface computer. After logging, the data are transferred from the tool to a shipboard computer. The fast-response (0.5 s) thermistor, although less accurate (0.01°C resolution), is able to detect small abrupt temperature excursions caused by fluid flow from the formation. The slow-response (2.5 s) thermistor is more accurate (0.001°C resolution) and can be used to estimate the temperature gradient. Data are recorded as a function of time. Conversions to depth were done by correlating the time between the wireline time-depth data obtained from the Schlumberger Maxis unit and the time-temperature pressure data from the TLT. The depth shift applied to obtain mbsf takes into account the fact that the TLT sensors are 1.3 m below the wireline zero.

Because logging is conducted soon after water circulation during drilling, the water temperatures measured by the TLT are not in equilibrium with the formation temperatures; thus, it is common to observe a gradual warming of the TLT temperatures as logging proceeds. Therefore, the temperatures taken from the last logging run are the closest to formation temperature, but even these should be considered minimum estimates. The measured temperatures are therefore extrapolated to equilibrium formation temperature whenever possible, as described in the site chapters. The geothermal gradient obtained from these and other in situ temperature data, coupled with the conductivity measurements taken on core samples, yield an estimate of heat flow at the well.

Data Quality

Downhole data quality may be seriously degraded in excessively large diameter sections of the borehole or by rapid changes in the hole diameter. Electrical resistivity and velocity measurements are less sensitive to such borehole effects. The nuclear measurements (density, neutron porosity, and both natural and induced spectral gamma rays) are the more seriously impaired because they rely on direct tool contact with the formation. However, processing can reduce these borehole effects to some extent.

Different logs may have small depth mismatches caused by cable stretch or ship heave during recording. To minimize such errors, a wireline hydraulic heave compensator adjusts for ship motion during logging. The natural gamma-ray tool is incorporated in all tool strings whenever possible to provide a common basis for log correlations.

IN SITU TEMPERATURE MEASUREMENTS

In situ thermal measurements were made using the Adara APC temperature tool and the DVTP (Davis-Villinger Temperature Tool; Davis et al., 1997). The in situ temperature instruments are described below and the resulting data are listed in the site chapters.

Adara APC Tool

The Adara tool consists of electronic components, including battery packs and a data logger, and a platinum resistance temperature device calibrated over a temperature range of 0°–30°C. A photograph of Adara components can be found in Fisher and Becker (1993). The Adara thermal tool fits directly into the cutting shoe on the APC and, therefore, can be used during regular piston coring. The thermal time constant of the cutting shoe assembly into which the Adara tool is inserted is ~2–3 min. To obtain thermal measurements, the only modification required to the normal APC procedures is that the corer be held in place for at least 10 min after firing. During this time the Adara tool tracks the thermal equilibration of the sediments.

The Adara tool logs data on a microprocessor contained within the instrument. Following deployment, the data are downloaded for processing on PC computers. The tool can be preprogrammed to record temperatures at a range of sampling rates. Sampling rates of 5 s were used during Leg 180.

A typical APC measurement consists of a mudline temperature record lasting 10 min for the first deployment at each borehole, a pulse of frictional heating when the piston is fired, a period of thermal decay that is monitored for 10 min, and a frictional pulse upon removal of the corer. Prior to reduction and drift corrections, the nominal accuracy of Adara temperature data is estimated at 0.1°C.

Davis-Villinger Temperature Probe

At depths below which the Adara tool could no longer be used, the DVTP was deployed. The probe is conical and has two thermistors, one located 1 cm from the tip of the probe and the other 12 cm above the tip. A third thermistor, referred to as the internal thermistor, is located in the electronics package. Thermistor sensitivity is 10^{-3} °C in an operating range of –5° to 20°C, and the total operating range is –5° to 100°C. The thermistors were calibrated at the factory and on the laboratory bench before installation in the probe. In addition to the thermistors, the probe contains an accelerometer sensitive to 0.98 $m \cdot s^{-2}$. Both peak and mean acceleration are recorded by the logger. The accelerometer data are used to track disturbances to the instrument package during the equilibration interval.

In a DVTP deployment, mudline temperatures are measured for 10 min on the first run within each hole before descent into the hole for a 10-min equilibration interval at the bottom. Mudline temperatures are also collected for at least 2 min on ascent. Data collected during Leg 164 indicate that the time constants are probably 1 min for the probe tip thermistor and ~2 min for the thermistor at 12 cm from the tip (Shipboard Scientific Party, 1996b). Data from the probe tip thermistor were used for estimation of in situ temperatures.

Data Reduction

Data reduction procedures are similar for all the temperature tools. The transient thermal decay curves for marine thermal probes are known to be a function of the geometry of the probes and the thermal properties of the probe and the sediments (Bullard, 1954; Horai and von Herzen, 1985). Analysis of data requires the construction of synthetic decay curves calculated on the basis of tool geometry, sampling

interval, and tool and sediment thermal properties. For the DVTP tool, thermal decay data are analyzed by comparison to computed type curves using the software program CONEFIT developed by Davis et al. (1997). However, it is never possible to obtain a perfect match between the synthetic curves and the data because (1) the probe never reaches thermal equilibrium during the penetration period; (2) contrary to theory, the frictional pulse upon insertion is never instantaneous; and (3) temperature data are sampled at discrete intervals, meaning that the exact time of penetration is always uncertain. Thus, both the effective penetration time and equilibrium temperature must be estimated by applying a fitting procedure, which involves shifting the synthetic curves in time to obtain a match with the recorded data. The data collected more than 20–50 s beyond penetration usually provide a reliable estimate of equilibrium temperature. The thermal decay curves for the measurements were initially fit aboard ship assuming formation thermal conductivity of 1.0 $W \cdot m^{-1} \cdot °C^{-1}$ for all of the data. Thermal conductivities from core measurement (see **"Thermal Conductivity,"** p. 30) were used for final estimation of in situ temperatures and for calculation of heat flow. Laboratory thermal conductivity results were corrected to approximate in situ conditions assuming an increase in conductivity of 0.5% per 1000 m of water depth and a decrease in conductivity of 0.25% per degree of temperature increase (Ratcliffe, 1960). These corrections do not account for any underestimation of thermal conductivity caused by elastic rebound during recovery of the cores.

VERTICAL SEISMIC PROFILING

Scientific Objectives

Vertical Seismic Profile (VSP) experiments measure compressional wave velocities from direct and reflected waves propagating through strata intersected by a borehole at seismic frequencies (10–100 Hz) and at seismic scales (hundreds of meters). The experiments provide results intermediate between small scale measurements such as laboratory analysis of cores and sonic logs and large scale measurements such as seismic refraction and reflection.

The goals of the VSP experiments conducted during Leg 180 included determination of the detailed *P*-wave velocity depth structure of the drilled section, an accurate correlation between the drilled section and the regional seismic reflection data, and improved deconvolution and amplitude decay functions for use in reprocessing surface multichannel seismic reflection data. Processing techniques can be applied to separate the upgoing and downgoing wavefields (Ross and Shaw, 1987; Christie et al., 1983; Kommedal and Tjostheim, 1989), which can then be analyzed for the attenuation properties of rock (Rutledge and Winkler, 1989; Swift and Stephen, 1992), for prediction of acoustic properties below the bottom of the hole (Swift et al., 1996) and for correlation with borehole lithology, wireline logs, and events on conventional seismic reflection and refraction profiles (Bolmer et al., 1992). The VSP measurements provide seismic information only for the interfaces penetrated by the borehole; reflecting interfaces below the bottom of the borehole are imaged by the VSP technique, but neither interval velocities nor time-depth information can be obtained (Gal'perin, 1974).

Acquisition Hardware

Leg 180 used the WST for VSP acquisition. The WST comprises a single vertical component geophone that is pressed against the borehole wall by a hydraulic caliper arm. The quality of the clamping between the tool and the side of the hole directly affects the quality of the signal received.

The signals received by the WST were recorded in Digital Log Interchange Standard (DLIS) format on 4-mm (DAT) tapes with the Schlumberger MAXIS system. The DLIS tapes were then converted to the standard seismic data format (SEGY) using Schlumberger's LOGOS software. Detailed processing takes place postcruise using a standard sequence (e.g., Hardage, 1985) and Landmark's INSIGHT seismic processing software.

Method

The WST was lowered down each hole using a clamping interval specific to each site (depending on time available and ease of clamping). This depth interval allowed us to record unaliased frequencies as high as 100 Hz (the approximate maximum frequency expected for an air-gun source) for velocities as low as 1524 $m \cdot s^{-1}$. The seismic source for the zero-offset VSP comprised one 4.9 L (300 in^3) air gun suspended from a buoy at 7 m water depth (Fig. F16). A hydrophone suspended near the air gun was used to record the source signal. Seven shots were fired at each clamping level and summed to increase signal-to-noise levels.

Preliminary shipboard processing included bandpass filtering, velocity filtering, and waveform deconvolution. The bandpass filter passed all frequencies between 10 and 60 Hz. Velocity filtering was used to separate the upgoing and downgoing waveforms by examining where reflectors fall on neighboring traces. Waveform deconvolution used the signal recorded at the near-surface hydrophone to remove the air-gun signature from the recorded traces.

F16. Air-gun configuration for zero-offset VSP experiment, p. 67.

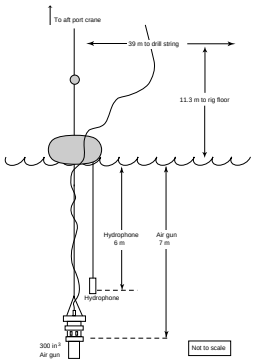

REFERENCES

Akimoto, K., 1994. Cenozoic benthic foraminiferal biostratigraphy, paleobathymetry, paleoenvironments and paleoceanography of the New Hebrides Island Arc and North d'Entrecasteaux Ridge area. *In* Greene, H.G., Collot, J.-Y., Stokking, L.B., et al., *Proc. ODP, Sci. Results,* 134: College Station, TX (Ocean Drilling Program), 265–291.

Archie, G.E., 1942. The electrical resistivity log as an aid in determining some reservoir characteristics. *J. Pet. Technol.,* 5:1–8.

ASTM, 1980. Standard method for laboratory determination of water (moisture) content of soil, rock and soil-aggregate mixtures. In *Annual Book of ASTM Standards:* Philadelphia (Am. Soc. Testing Materials).

————, 1987. Standard test method for laboratory miniature vane shear test for saturated fine-grained clayey soil. In *Annual Book of ASTM Standards* (Vol. 04.08): Philadelphia (Am. Soc. Testing and Mater.), 868–873.

Babcock, E.A., 1978. Measurement of subsurface fractures from dipmeter logs. *AAPG Bull.,* 62:1111–1126.

Barker, R.W., 1960. Taxonomic notes on the species figured by H.B. Brady in his report on the foraminifera dredged by *H.M.S. Challenger* during the years 1873–1876. *Spec. Publ.—Soc. Econ. Paleontol. Mineral.,* 9:1–238.

Beaudemont, D., Ruhland, M., Gauer, P., and Janot, P., 1988. L'ovalisation des trous de forages—synthèse bibliographique. *Rev. Inst. Fr. Pet.,* 43:389–403.

Bell, J.S., and Gough, D.I., 1979. Northeast-southwest compressive stress in Alberta: evidence from oil wells. *Earth Planet. Sci. Lett.,* 45:475–482.

Berggren, W.A., Kent, D.V., Swisher, C.C. III, and Aubry, M.-P., 1995a. A revised Cenozoic geochronology and chronostratigraphy. *In* Berggren, W.A., Kent, D.V., Aubry, M.-P., and Hardenbol, J. (Eds.), *Geochronology Time Scales and Global Stratigraphic Correlation,* SEPM Spec. Publ. 54:129–212.

Berggren, W.A., Hilgen, F.J., Langereis, C.G., Kent, D.V., Obradovich, J.D., Raffi, I., Raymo, M.E., and Shackleton, N.J., 1995b. Late Neogene chronology: new perspectives in high-resolution stratigraphy. *Geol. Soc. Am. Bull.,* 107:1272–1287.

Blow, W.H., 1969. Late middle Eocene to Recent planktonic foraminiferal biostratigraphy. *In* Brönnimann, P., and Renz, H.H. (Eds.), *Proc. First Int. Conf. Planktonic Microfossils, Geneva, 1967:* Leiden (E.J. Brill), 1:199–422.

Blum, P., 1997. Physical properties handbook: a guide to the shipboard measurements of physical properties of deep-sea cores. *ODP Tech. Note,* 26.

Bolmer, S.T., Buffler, R.T., Hoskins, H., Stephen, R.A., and Swift, S.A., 1992. Vertical seismic profile at Site 765 and seismic reflectors in the Argo Abyssal Plain. *In* Gradstein, F.M., Ludden, J.N., et al., *Proc. ODP, Sci. Results,* 123: College Station, TX (Ocean Drilling Program), 583–600.

Bouma, A.H., 1962. *Sedimentology of Some Flysch Deposits: A Graphic Approach to Facies Interpretation:* Amsterdam (Elsevier).

Boyce, R.E., 1976. Definitions and laboratory techniques of compressional sound velocity parameters and wet-water content, wet-bulk density, and porosity parameters by gravimetric and gamma-ray attenuation techniques. *In* Schlanger, S.O., Jackson, E.D., et al., *Init. Repts. DSDP,* 33: Washington (U.S. Govt. Printing Office), 931–958.

Bullard, E.C., 1954. The flow of heat through the floor of the Atlantic Ocean. *Proc. R. Soc. London A,* 222:408–429.

Burke, S.C., 1981. Recent benthic foraminifera of the Ontong Java plateau. *J. Foraminiferal Res.,* 11:1–19.

Cande, S.C., and Kent, D.V., 1995. Revised calibration of the geomagnetic polarity time scale for the Late Cretaceous and Cenozoic. *J. Geophys. Res.,* 100:6093–6095.

Cannat, M., Karson, J.A., Miller, D.J., et al., 1995. *Proc. ODP, Init. Repts.,* 153: College Station, TX (Ocean Drilling Program).

Christie, P.A.F., Hughes, V.J., and Kennett, B.L.N., 1983. Velocity filtering of seismic reflection data. *First Break,* 1:9–24.

Cita, M.B., 1996a. Report on the 30th International Geological Congress. *Neogene Newsletter,* 3:62–65.

————, 1996b. Submission of the recommendation for the definition of the Gelasian. *Neogene Newsletter,* 3:49–51.

Clark, F.E., Patterson, R.T., and Fishbein, E., 1994. Distribution of Holocene benthic foraminifera from the tropical southwest Pacific Ocean. *J. Foraminiferal Res.,* 24:241–267.

Cox, J.W., 1970. The high resolution dipmeter reveals dip-related borehole and formation characteristics. *Trans. SPWLA Annu. Logging Symp.,* 11:1–25.

Cragg, B.A., 1994. Bacterial profiles in deep sediment layers from the Lau Basin (Site 834). *In* Hawkins, J., Parson, L., Allan, J., et al., *Proc. ODP, Sci. Results,* 135: College Station, TX (Ocean Drilling Program), 147–150.

Cragg, B.A., Harvey, S.M., Fry, J.C., Herbert, R.A., and Parkes, R.J., 1992. Bacterial biomass and activity in the deep sediment layers of the Japan Sea, Hole 798B. *In* Pisciotto, K.A., Ingle, J.C., Jr., von Breymann, M.T., Barron, J., et al., *Proc. ODP, Sci. Results.,* 127/128 (Pt. 1): College Station, TX (Ocean Drilling Program), 761–776.

Dart, R.L., and Zoback, M.L., 1989. Wellbore breakouts stress analysis within the Central and Eastern continental United States. *Log Analyst,* 30:5497–5512.

Davis, E.E., Villinger, H., MacDonald, R.D., Meldrum, R.D., and Grigel, J., 1997. A robust rapid-response probe for measuring bottom-hole temperatures in deep-ocean boreholes. *Mar. Geophys. Res.,* 19:267–281.

Detournay, E., and Cheng, A.H.D., 1988. Poroelastic response of a borehole in a non-hydrostatic stress field. *Int. J. Rock Mech. Min. Sci. Geomech. Abstr.,* 25:171–182.

Dick, H.J.B, Natland, J., Miller, D.J., et al., 1999. *Proc. ODP., Init. Repts.,* 176: College Station, TX, (Ocean Drilling Program).

Dowsett, H., 1988. Diachrony of the late Neogene microfossils in the southwest Pacific Ocean: application of the graphic correlation method. *Paleoceanography,* 3:209–222.

Ekstrom, M.P., Dahan, C.A., Chen, M.-Y., Lloyd, P.M., and Rossi, D.J., 1986. Formation imaging with microelectrical scanning arrays. *Trans. SPWLA 27th Annu. Logging Symp.,* Pap. BB.

Ellis, D.V., 1987. *Well Logging for Earth Scientists:* New York (Elsevier).

Emeis, K.-C., and Kvenvolden, K.A., 1986. Shipboard organic geochemistry on *JOIDES Resolution. ODP Tech. Note,* 7.

Fisher, R.V., and Schmincke, H.-U., 1984. *Pyroclastic Rocks:* New York (Springer-Verlag).

Fisher, A., and Becker, K., 1993. A guide to ODP tools for downhole measurements. *ODP Tech. Note,* 10.

Fordjor, C.K., Bell, J.S., and Gough, D.I., 1983. Breakouts in Alberta and stress in the North American plate. *Can. J. Earth Sci.,* 20:1445–1455.

Frey, R.W., and Pemberton, S.G., 1984. Trace fossils facies models. *In* Walker, R.G. (Ed.), *Facies Models* (2nd ed.): Geosci. Can., Reprint Ser., 1:189–207.

Fry, J.C., 1988. Determination of biomass. *In* Austin, B. (Ed.), *Methods in Aquatic Bacteriology:* Chichester (Wiley), 27–72.

Fry, N., 1984. *The Field Description of Metamorphic Rocks*. Open University Press, Milton Keynes.

Gal'perin, E.I., 1974. *Vertical Seismic Profiling*. Spec. Publ.—Soc. Explor. Geophys., 12.

Gieskes, J.M., Gamo, T., and Brumsack, H., 1991. Chemical methods for interstitial water analysis aboard *JOIDES Resolution. ODP Tech. Note,* 15.

Gillis, K., Mével, C., Allan, J., et al., 1993. *Proc. ODP, Init. Repts.,* 147: College Station, TX (Ocean Drilling Program).

Gough, D.I., and Bell, J.S., 1981. Stress orientations from oil well fractures in Alberta and Texas. *Can. J. Earth Sci.,* 18:638–645.

———, 1982. Stress orientations from borehole wall fractures with examples from Colorado, East Texas, and northern Canada. *Can. J. Earth Sci.,* 19:1358–1370.

Graham, J.J., and Militante, P.J., 1959. Recent Foraminifera from the Puerto Galera area, Northern Mindoro, Philippines. *Stanford Univ. Publ., Geol. Sci.,* 6:1–127.

Guenot, A., 1989. Borehole breakouts and stress fields. *Int. J. Rock Mech. Min. Sci. and Geomech. Abstr.,* 26:181–195.

Haig, D.W., and Perembo, R.C.B., 1990. Foraminifera as stratigraphic guides for Papua New Guinea. *In* Carmen, G.J., and Carmen, Z. (Eds.), *Petroleum Exploration in Papua New Guinea: Proc. 1st PNG Petrol. Conv.:* Port Moresby (Brown Prior Anderson), 381–395.

Haimson, B., and Fairhurst, C., 1967. Initiation and extension of hydraulic fractures in rocks. *Soc. Pet. Eng. J.,* 7:310–318.

Hardage, B.A., 1985. *Vertical Seismic Profiling, Part A: Principles* (2nd ed.): London (Geophysical Press).

Hearst, J.R., and Nelson, P.H., 1985. *Well Logging for Physical Properties:* New York (McGraw-Hill).

Hermelin, J.O.R., 1989. Pliocene benthic foraminifera from the Ontong-Java plateau (Western Equatorial Pacific Ocean): faunal response to changing paleoenvironment. *Spec. Publ. Cushman Found. Foraminiferal Res.,* 26:1–143.

Hickman, S.H., Healy, J.H., and Zoback, M.D., 1985. In situ stress, natural fracture distribution, and borehole elongation in the Auburn geothermal well, Auburn, New York. *J. Geophys. Res.,* 90:5497–5512.

Hoppie, B.W., Blum, P., and the Shipboard Scientific Party, 1994. Natural gamma-ray measurements on ODP cores: introduction to procedures with examples from Leg 150. *In* Mountain, G.S., Miller, K.G., Blum, P., et al., *Proc. ODP, Init. Repts.,* 150: College Station, TX (Ocean Drilling Program), 51–59.

Horai, K., and Von Herzen, R.P., 1985. Measurement of heat flow on Leg 86 of the Deep Sea Drilling Project. *In* Heath, G.R., Burckle, L.H., et al., *Init. Repts. DSDP,* 86: Washington (U.S. Govt. Printing Office), 759–777.

Hottman, C.E., Smith, J.H., and Purcell, W.R., 1979. Relationship among Earth stresses, pore pressure, and drilling problems offshore Gulf of Alaska. *J. Pet. Tech.,* 31:1477–1484.

Hubbert, M.K., and Willis, D.G., 1957. Mechanics of hydraulic fracturing [with discussion and reply by the authors]. *AIME Trans.,* 210:153–163.

Hughes, G.W., 1977. Recent foraminifera from the Honiara Bay area, Solomon Islands. *J. Foraminiferal Res.,* 7:45–57.

Ingle, J.C., 1980. Cenozoic paleobathymetry and depositional history of selected sequences within the Southern California continental borderland. *Spec. Publ. Cushman Found. Foraminiferal Res.,* 19:163–195.

Irvine, T.N., 1982. Terminology for layered intrusions. *J. Petrol.,* 23:127–162.

Jelinek, V., 1981. Characterization of the magnetic fabric of rocks. *Tectonophysics,* 79:63–67.

Kennett, J.P., and Srinivasan, M.S., 1983. *Neogene Planktonic Foraminifera: A Phylogenetic Atlas:* Stroudsburg, PA (Hutchinson Ross).

Kirsch, G., 1898. Die Theorie der Elastizität und die Bedürfnisse der Festigkeitslehre. *VDI—Z,* 42:797–807.

Kommedal, J.H., and Tjøstheim, B.A., 1989. A study of different methods of wavefield separation for application to VSP data. *Geophys. Prospect.,* 37:117–142.

Kopf, A., and Flecker, R., 1996. Problems associated with the interpretation of normal fault distributions in sediments recovered by the advanced hydraulic piston corer during Leg 160, Eastern Mediterranean. *In* Emeis, K.-C., Robertson, A.H.F., Richter, C., et al., *Proc. ODP, Init. Repts.,* 160: College Station, TX (Ocean Drilling Program), 507–511.

Kurihara, K., and Kennett, J.P., 1986. Neogene benthic foraminifers: distribution in depth traverse, southwest Pacific. *In* Kennett, J.P., von der Borch, C.C., et al., *Init. Repts. DSDP,* 90: Washington (U.S. Govt. Printing Office), 1037–1077.

————, 1988. Bathymetric migration of deep-sea benthic foraminifera in the southwest Pacific during the Neogene. *J. Foraminiferal Res.,* 18:75–83.

Kvenvolden, K.A., and McDonald, T.J., 1986. Organic geochemistry on the *JOIDES Resolution*—an assay. *ODP Tech. Note,* 6.

Le Maitre, R.W., 1989. *A Classification of Igneous Rocks and Glossary of Terms:* Oxford (IUGS, Blackwell).

Lock, G.A., and Hoyer, W.A., 1971. Natural gamma-ray spectral logging. *Log Analyst,* 12:3–9.

Loeblich, A.R., Jr., and Tappan, H., 1988. *Foraminiferal Genera and Their Classification:* New York (Van Nostrand Reinhold).

Lundberg, N., and Moore, J.C., 1986. Macroscopic structural features in Deep Sea Drilling Project cores from forearc regions. *In* Moore, J.C. (Ed.), *Structural Fabric in Deep Sea Drilling Project Cores From Forearcs*. Mem.—Geol. Soc. Am., 166:13–44.

MacLeod, C.J., Parson, L.M., and Sager, W.W., 1992. Identification of tectonic rotations in boreholes by the integration of core information with Formation MicroScanner and borehole televiewer images, *In* Hurst, A., Griffiths, C.M., and Worthington, P.F. (Eds.), *Geological applications of wireline logs: II*. Geol. Soc. Spec. Publ. London, 65:235–246.

Manheim, F.T., and Sayles, F.L., 1974. Composition and origin of interstitial waters of marine sediments, based on deep sea drill cores. *In* Goldberg, E.D. (Ed.), *The Sea* (Vol. 5): *Marine Chemistry: The Sedimentary Cycle:* New York (Wiley), 527–568.

Martini, E., 1971. Standard Tertiary and Quaternary calcareous nannoplankton zonation. *In* Farinacci, A. (Ed.), *Proc. 2nd Int. Conf. Planktonic Microfossils Roma:* Rome (Ed. Tecnosci.), 2:739–785.

Mazzullo, J.M., Meyer, A., and Kidd, R.B., 1988. New sediment classification scheme for the Ocean Drilling Program. *In* Mazzullo, J., and Graham, A.G. (Eds.), *Handbook for Shipboard Sedimentologists*. ODP Tech. Note, 8:45–67.

Miall, A.D., 1984. *Principles of Sedimentary Basin Analysis:* New York (Springer-Verlag).

Morin, R.H., Anderson, R.N., and Barton, C.A., 1989. Analysis and interpretation of the borehole televiewer log: information on the state of stress and the lithostratigraphy at Hole 504B. *In* Becker, K., Sakai, H., et al., *Proc. ODP, Sci. Results,* 111: College Station, TX (Ocean Drilling Program), 109–118.

Morin, R.H., Newmark, R.L., Barton, C.A., and Anderson, R.N., 1990. State of lithospheric stress and borehole stability at Deep Sea Drilling Project Site 504B, eastern Equatorial Pacific. *J. Geophys. Res.,* 95:9293–9303.

Newmark, R.L., Zoback, M.D., and Anderson, R.N., 1984. Orientation of in situ stresses in the oceanic crust. *Nature,* 311:424–428.

————, 1985. Orientation of in situ stresses near the Costa Rica Rift and Peru-Chile Trench, Deep Sea Drilling Project Hole 504B. *In* Anderson, R.N., Honnorez, J., Becker, K., et al., *Init. Repts. DSDP,* 83: Washington (U.S. Govt. Printing Office), 511–514.

Newmark, R.L., Anderson, R.N., Moos, D., and Zoback, M.D., 1985. Sonic and ultrasonic logging of Hole 504B and its implications for the structure, porosity, and stress regime of the upper 1 km of the oceanic crust. *In* Anderson, R.N., Honnorez, J., Becker, K., et al., *Init. Repts. DSDP,* 83: Washington (U.S. Govt. Printing Office), 479–510.

Parkes, R.J., Cragg, B.A., Bale, S.J., Getliff, J.M., Goodman, K., Rochelle, P.A., Fry, J.C., Weightman, A.J., and Harvey, S.M., 1994. A deep bacterial biosphere in Pacific Ocean sediments. *Nature,* 371:410–413.

Paull, C.K., Matsumoto, R., Wallace, P.J., et al., 1996. *Proc. ODP, Init. Repts.,* 164: College Station, TX (Ocean Drilling Program).

Perembo, R.C.B., 1994. Miocene foraminifera from bathyal deposits of Foreland Megasequence 1 in the Papuan Fold Belt, Papua New Guinea. [PhD dissert.]. Univ. Western Australia, Nedlands.

Pettigrew, T.L., Casey, J.F., Miller, D.J., et al., 1999. *Proc. ODP, Init. Repts.,* 179: College Station, TX (Ocean Drilling Program).

Pezard, P.A., and Anderson, R.N., 1990. Electrical resistivity, anisotropy, and tectonic context. *Trans. SPWLA 31st Annu. Logging Symp.,* paper M.

Pezard, P.A., Lovell, M., Fujioka, K., Taylor, B., Janecek, T., Aitchison, J.C., Cisowski, S., Colella, A., Cooper, P.A., Klaus, A., Dadey, K.A., Egeberg, P., Firth, J., Isiminger, K.M., Gill, J.B., Herman, Y., Hiscott, R.N., Kaiho, K., Koyama, M., Lapierre, H., Marsaglia, K., Nishimura, A., Rodolfo, K.S., Taylor, R., Tazaki, K., and Torssander, P., 1990. Downhole images: electrical scanning reveals the nature of subsurface oceanic crust. *Eos,* 71:709, 718.

Pezard, P.A., Lovell, M.A., and Hiscott, R.N., 1992. Downhole electrical images in volcaniclastic sequences of the Izu-Bonin forearc basin, western Pacific. *In* Taylor, B., Fujioka, K., et al., *Proc. ODP, Sci. Results,* 126: College Station, TX (Ocean Drilling Program), 603–624.

Pickering, K.T., Hiscott, R., and Hein, F.J., 1989. *Deep-marine Environments: Clastic Sedimentation and Tectonics:* London (Unwin Hyman).

Piper, D.J.W., 1978. Turbidite muds and silts on deep-sea fans and abyssal plains. *In* Stanley, D.J., and Kelling, G. (Eds.), *Sedimentation in Submarine Canyons, Fans and Trenches:* Stroudsburg, PA (Dowden, Hutchinson and Ross), 163–175.

Plumb, R.A., and Hickman, S.H., 1985. Stress-induced borehole elongation: a comparison between the four-arm dipmeter and the borehole televiewer in the Auburn geothermal well. *J. Geophys. Res.,* 90:5513–5521.

Ratcliffe, E.H., 1960. The thermal conductivities of ocean sediments. *J. Geophys. Res.,* 65:1535–1541.

Resig, J.M., 1984. Comparative bathymetry of Recent benthic foraminiferal species in east Asian and western equatorial Pacific waters. *Proc. Korea-U. S. Sem. Workshop Mar. Geol. Phys. Proc. Yellow Sea,* 260–270.

Resig, J.M., and Cheong, H.-K., 1997. Pliocene-Holocene benthic foraminiferal assemblages and water mass history, ODP 806B, western equatorial Pacific. *Micropaleontology,* 43:419–439.

Rio, D., Raffi, I., and Villa, G., 1990. Pliocene-Pleistocene calcareous nannofossil distribution patterns in the Western Mediterranean. *In* Kastens, K.A., Mascle, J., et al., *Proc. ODP, Sci. Results,* 107: College Station, TX (Ocean Drilling Program), 513–533.

Ross, W.S., and Shaw, P.M., 1987. Vertical seismic profile reflectivity: ups over downs. *Geophysics,* 52:1149–1154.

Rutledge, J.T., and Winkler, H., 1989. Attenuation measurements from vertical seismic profile data: Leg 104, Site 642. *In* Eldholm, O., Thiede, J., Taylor, E., et al., *Proc. ODP, Sci. Results,* 104: College Station, TX (Ocean Drilling Program), 965–972.

Schafer, J.N., 1980. A practical method of well evaluation and acreage development for the naturally fractured Austin Chalk formation. *Log Analyst,* 21:10–23.

Schlumberger, 1989. *Log Interpretation Principles/Applications:* Houston (Schlumberger Educ. Services).

Schulz, A.W., 1984. Subaerial debris-flow deposition in the Upper Paleozoic Cutter Formation. *J. Sediment. Petrol.,* 54:759–772.

Serra, O., 1984. *Fundamentals of Well-Log Interpretation* (Vol. 1): *The Acquisition of Logging Data:* Dev. Pet. Sci., 15A: Amsterdam (Elsevier).

————, 1989. *Formation MicroScanner Image Interpretation:* Houston (Schlumberger Educ. Services), SMP-7028. [\7-27-94]

Shackleton, N.J., Baldauf, J.G., Flores, J.-A., Iwai, M., Moore, T.C. Jr., Raffi, I., and Vincent, E., 1995. Biostratigraphic summary for Leg 138. *In* Pisias, N.G., Mayer, L.A., Janecek, T.R., Palmer-Julson, A., and van Andel, T.H. (Eds.) *Proc. ODP, Sci. Results,* 138: College Station, TX (Ocean Drilling Program), 517–536.

Shamir, G., Zoback, M.D., and Barton, C.A., 1988. In situ stress orientation near the San Andreas fault: preliminary results to 2.1 km depth from the Cajon Pass scientific drillhole. *Geophys. Res. Lett.,* 15:989–992.

Shipboard Scientific Party, 1989. Introduction and explanatory notes. *In* Robinson, P.T., Von Herzen, R., et al., *Proc. ODP, Init. Repts.,* 118: College Station, TX (Ocean Drilling Program), 3–24.

————, 1990a. Explanatory notes. *In* Taylor, B., Fujioka, K., et al., *Proc. ODP, Init. Repts.,* 126: College Station, TX (Ocean Drilling Program), 13–42.
————, 1990b. Site 792. *In* Taylor, B., Fujioka, K., et al., *Proc. ODP, Init. Repts.,* 126: College Station, TX (Ocean Drilling Program), 221–314.
————, 1991. Explanatory notes. *In* Taira, A., Hill, I., Firth, J.V., et al., *Proc. ODP, Init. Repts.,* 131: College Station, TX (Ocean Drilling Program), 25–60.
————, 1992a. Explanatory notes. *In* Behrmann, J.H., Lewis, S.D., Musgrave, R.J., et al., *Proc. ODP, Init. Repts.,* 141: College Station, TX (Ocean Drilling Program), 37–71.
————, 1992b. Explanatory notes. *In* Collot, J.-Y., Greene, H.G., Stokking, L.B., et al., *Proc. ODP, Init. Repts.,* 134: College Station, TX (Ocean Drilling Program), 65–91.
————, 1992c. Explanatory notes. *In* Dick, H.J.B., Erzinger, J., Stokking, L.B., et al., *Proc. ODP, Init. Repts.,* 140: College Station, TX (Ocean Drilling Program), 5–33.
————, 1993. Explanatory notes. *In* Gillis, K., Mével, C., Allan, J., et al., *Proc. ODP, Init. Repts.,* 147: College Station, TX (Ocean Drilling Program), 15–42.
————, 1994. Explanatory notes. *In* Larsen, H.C., Saunders, A.D., Clift, P.D., et al., *Proc. ODP, Init. Repts.,* 152: College Station, TX (Ocean Drilling Program), 17–39.
————, 1995a. Explanatory notes. *In* Cannat, M., Karson, J.A., Miller, D.J., et al., *Proc. ODP, Init. Repts.,* 153: College Station, TX (Ocean Drilling Program), 15–42.
————, 1995b. Explanatory notes. *In* Shipley, T.H., Ogawa, Y., Blum, P., et al., *Proc. ODP, Init. Repts.,* 156: College Station, TX (Ocean Drilling Program), 39–68.
————, 1996a. Explanatory notes. *In* Emeis, K.-C., Robertson, A.H.F., Richter, C., et al., *Proc. ODP, Init. Repts.,* 160: College Station, TX (Ocean Drilling Program), 29–52.
————, 1996b. Explanatory notes. *In* Paull, C.K., Matsumoto, R., Wallace, P.J., et al., *Proc. ODP, Init. Repts.,* 164: College Station, TX (Ocean Drilling Program), 13–41.
————, 1997. Explanatory notes. *In* Eberli, G.P., Swart, P.K., Malone, M.J., et al., *Proc. ODP, Init. Repts.,* 166: College Station, TX (Ocean Drilling Program), 43–68.
————, 1998a. Explanatory notes. *In* Christie-Blick, N., Austin, J.A., et al., *Proc. ODP, Init. Repts.,* 174A: College Station, TX (Ocean Drilling Program).
————, 1998b. Explanatory Notes. *In* Fouquet, Y., Zierenberg, R.A., Miller, D.J., et al., *Proc. ODP, Init. Repts.,* 169: College Station, TX (Ocean Drilling Program).
————, 1999a. Explanatory Notes. *In* Barker, P.F., Camerlenghi, A., Acton, G.D., et al., *Proc. ODP, Init. Repts.,* 178, 1–67 [CD-ROM]. Available from: Ocean Drilling Program, Texas A&M University, College Station, TX 77845-9547, U.S.A.
————, 1999b. Explanatory Notes. *In* Dick, H.J.B., Natland, J.H., Miller, D.J., et al., *Proc. ODP, Init. Repts.,* 176, 1–42 [CD-ROM]. Available from: Ocean Drilling Program, Texas A&M University, College Station, TX 77845-9547, U.S.A.
————, 1999c. Explanatory Notes. *In* Pettigrew, T.L., Casey, J.F., Miller, D.J., et al., *Proc. ODP, Init. Repts.,* 179, 1–47 [CD-ROM]. Available from: Ocean Drilling Program, Texas A&M University, College Station, TX 77845-9547, U.S.A.
Stow, D.A.V., and Piper, D.J.W., 1984. Deep-water fine-grained sediments: facies models. *In* Stow, D.A.V., and Piper, D.J.W. (Eds.), *Fine-Grained Sediments: Deep-Water Processes and Facies*. Geol. Soc. Spec. Publ. London, 15:611–645.
Swift, S.A., and Stephen, R.A., 1992. How much gabbro is in ocean seismic layer 3? *Geophys. Res. Lett.,* 19:1871–1874.
Swift, S.A., Hoskins, H., and Stephen, R.A., 1996. Vertical seismic profile into upper oceanic crust in Hole 504B. *In* Alt, J.C., Kinoshita, H., Stokking, L.B., and Michael, P.J. (Eds.), *Proc. ODP, Sci. Results,* 148: College Station, TX (Ocean Drilling Program), 339–347.
Timur, A., and Toksöz, M.N., 1985. Downhole geophysical logging. *Annu. Rev. Earth Planet. Sci.,* 13:315–344.
Turner, F.J., and Verhoogen, J., 1960. *Igneous and Metamorphic Petrology:* New York (McGraw Hill).
Twiss, R.J., and Moores, E.M., 1992. *Structural Geology:* New York (W.H. Freeman).

van Morkhoven, F.P.C.M., Berggren, W.A., and Edwards, A.S., 1986. Cenozoic cosmopolitan deep-water benthic foraminifera. *Bull. Cent. Rech. Explor.—Prod. Elf-Aquitaine,* Mem. 11.

Von Herzen, R.P., and Maxwell, A.E., 1959. The measurement of thermal conductivity of deep-sea sediments by a needle-probe method. *J. Geophys. Res.,* 64:1557–1563.

Wellsbury, P., Goodman, K., Barth, T., Cragg, B.A., Barnes, S.P., and Parkes, R.J., 1997. Deep marine biosphere fueled by increasing organic matter availability during burial and heating. *Nature,* 388: 573–576.

Wentworth, C.K., 1922. A scale of grade and class terms of clastic sediments. *J. Geol.,* 30:377–392.

Zemanek, J., Glenn, E.E., Norton, L.J., and Caldwell, R.L., 1970. Formation evaluation by inspection with the borehole televiewer. *Geophysics,* 35:254–269.

Zemanek, J., Caldwell, R.L., Glenn, E.E., Holcomb, S.V., Norton, L.J., and Strauss, A.J.D., 1970. The borehole televiewer–a new logging concept for fracture location and other borehole inspection. *J. Petrol. Tech.,* 21:762–774.

Zoback, M.D., Moos, D., Mastin, L., and Anderson, R.N., 1985. Well bore breakouts and in situ stress. *J. Geophys. Res.,* 90:5523–5530.

Figure F1. Diagram illustrating core, section, and sample numbering.

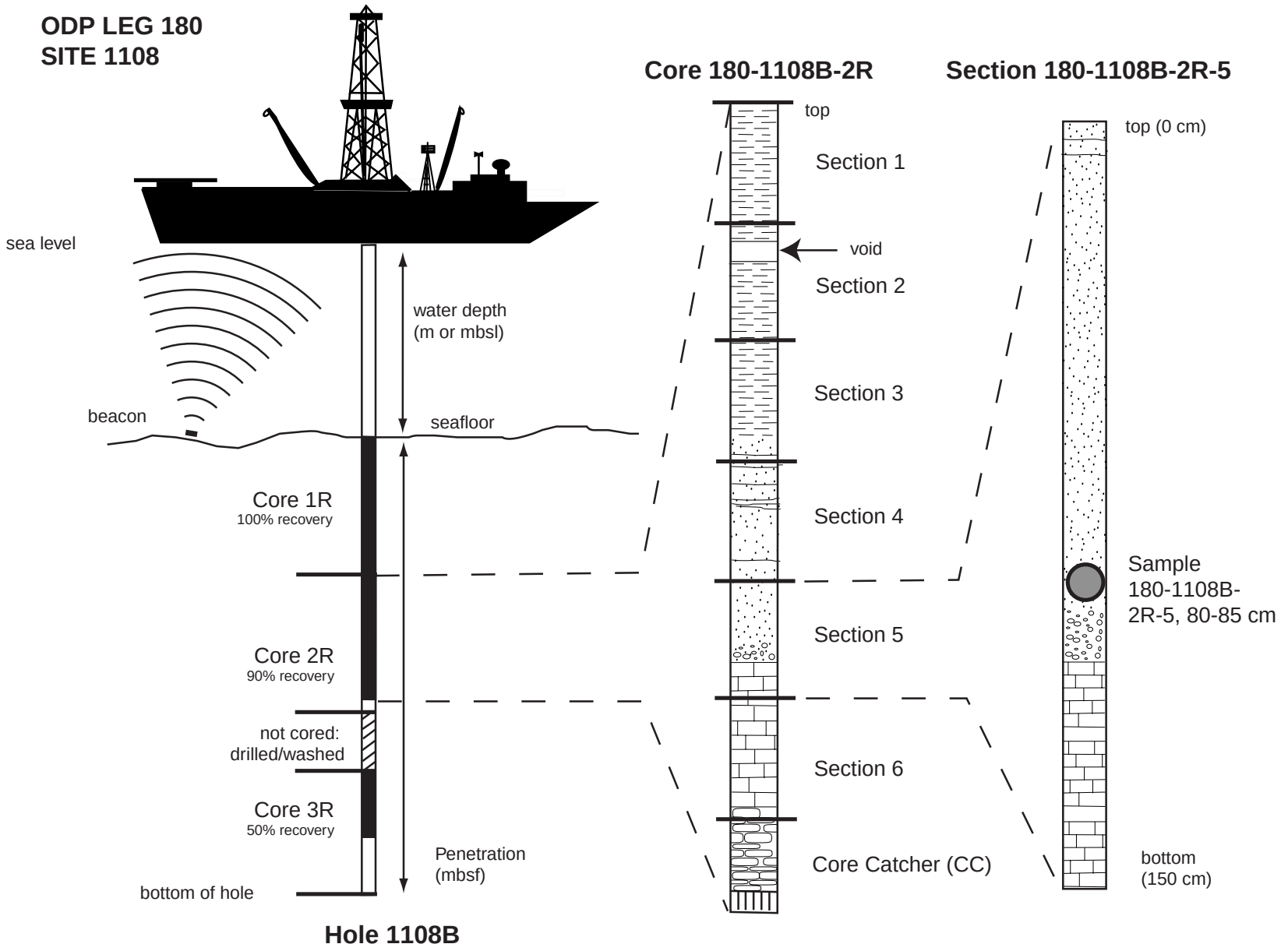

Figure F2. Key to symbols used in the "Graphic Lithology," "Structure," "Disturbance," and "Sample" columns of the core description and barrel sheets.

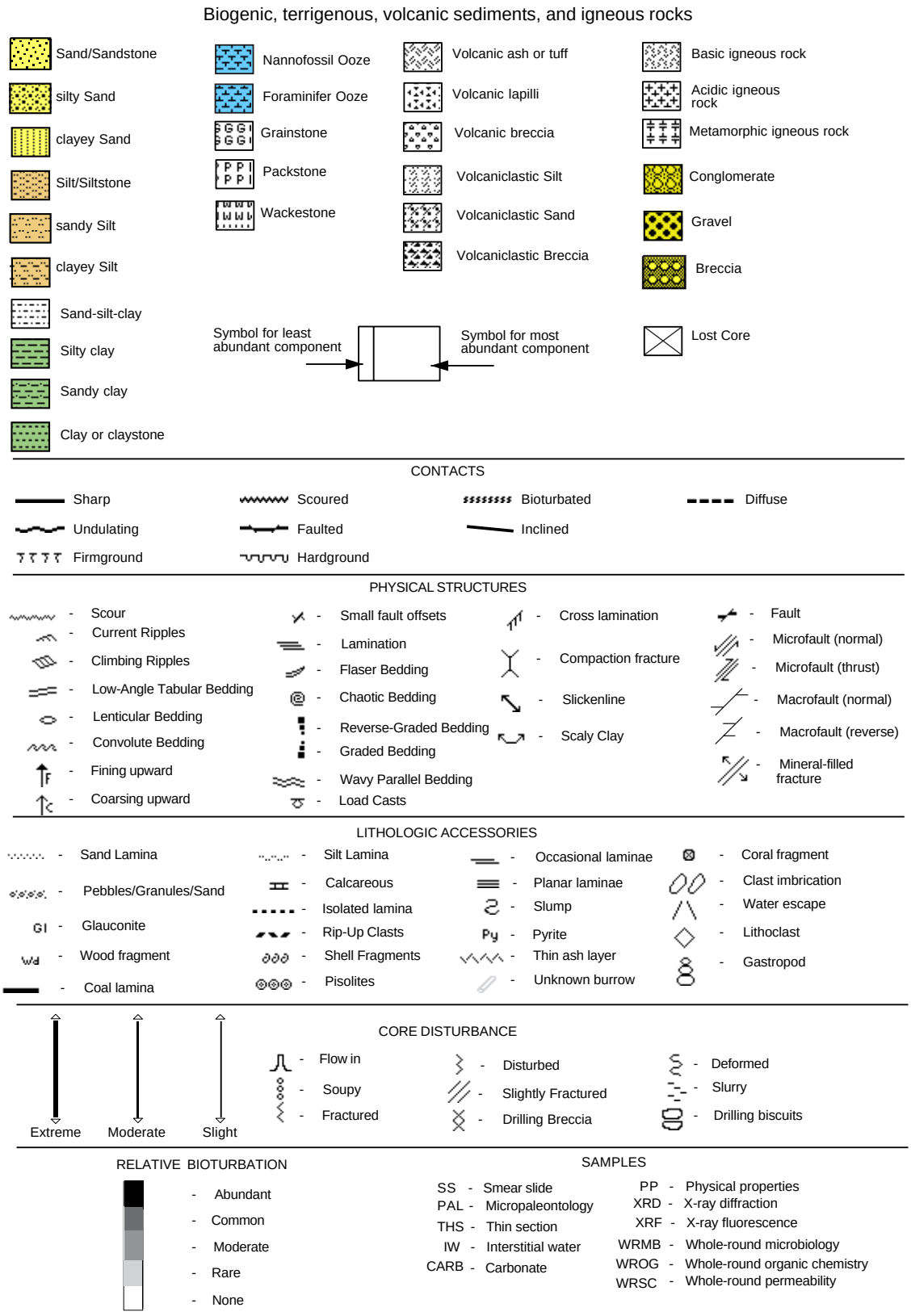

Figure F3. Diagram showing classes of granular sediment (after Muzzullo et al., 1988).

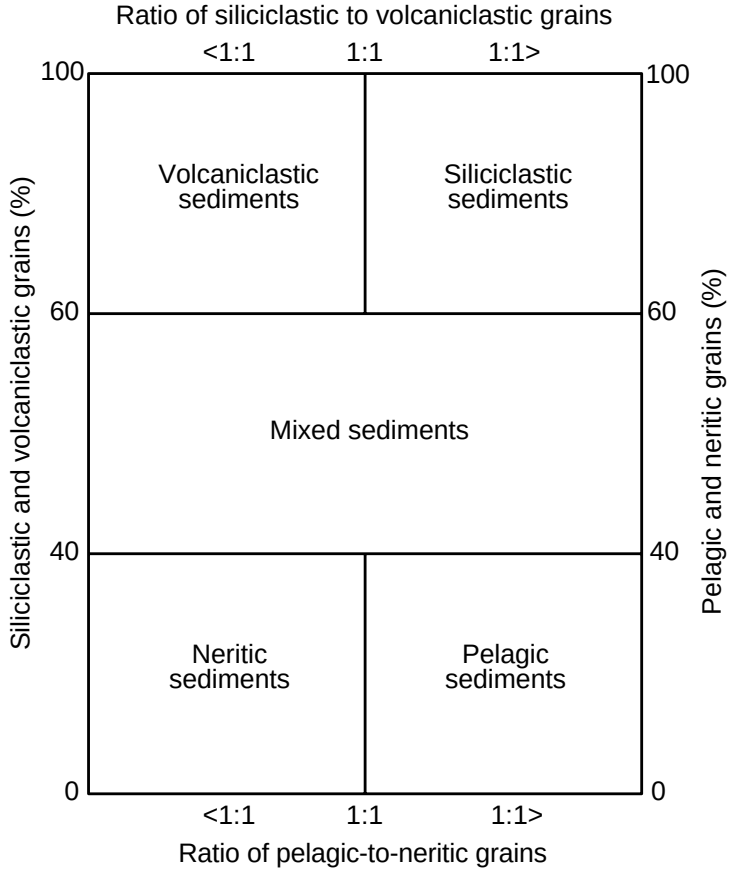

Figure F4. Lithologic classification scheme for sediments consisting of >70% terrigenous components. When the sediment consists of 50%–70% terrigenous components, this classification scheme is used and is preceded by a modifier that describes the nonterrigenous component. The general term "mud" may be replaced by more specific names, such as sand, silt, or clay.

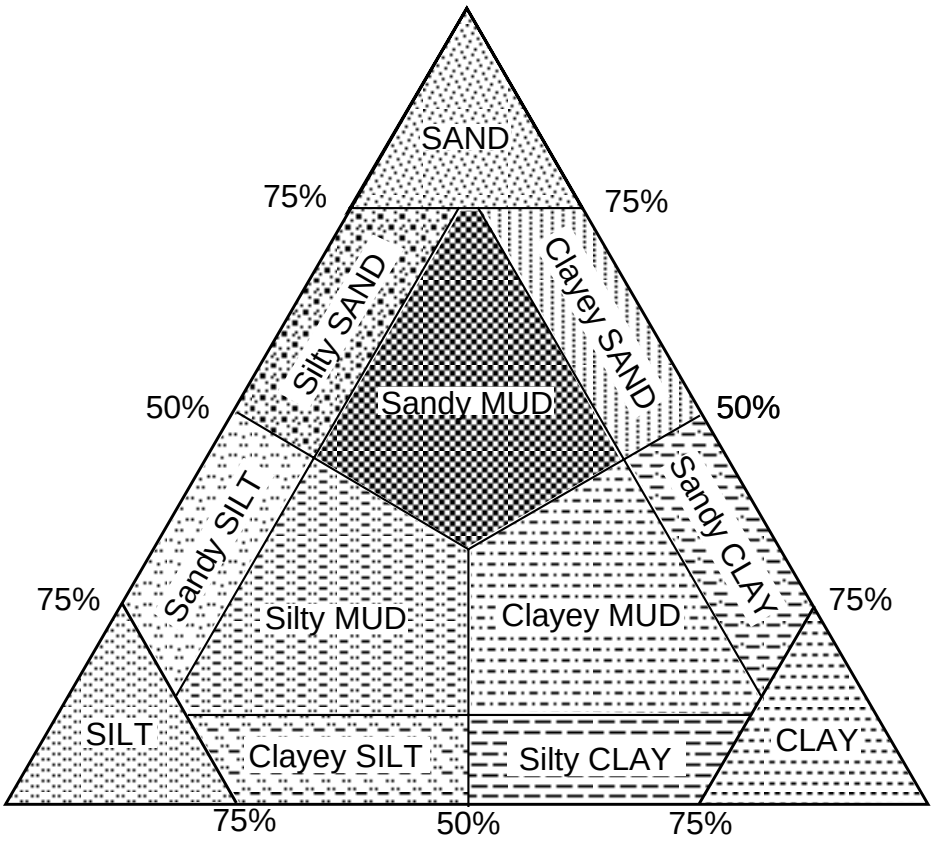

Figure F5. Schematic diagram showing the different types of debrites (debris-flow deposits). Clast-supported gravel or conglomerate include both inversely graded (Ci) and massive (Cm) gravels or conglomerate. Matrix-supported gravels or conglomerate include both massive (structureless) (Mm) and graded gravels or conglomerates (Mg) (after Schulz, 1984).

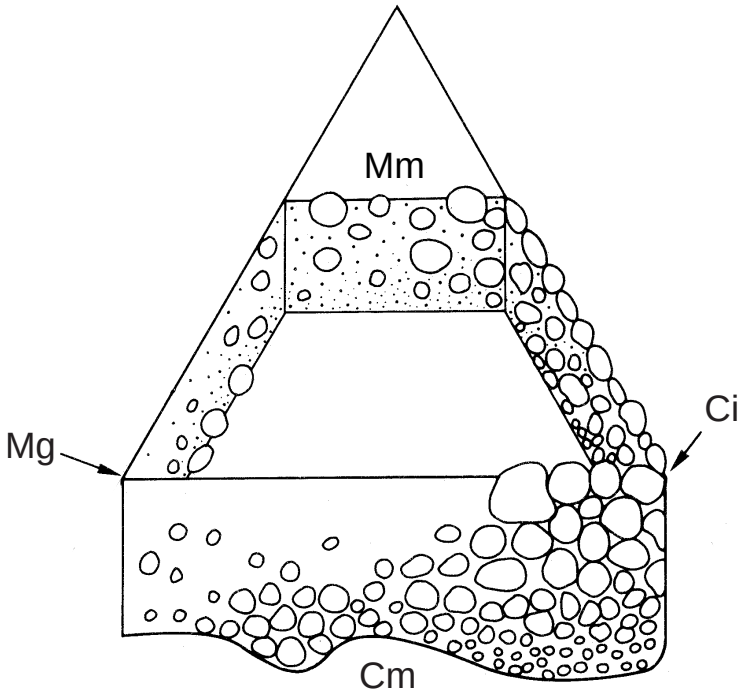

Figure F6. Schematic representation of internal structure of facies within turbidites recovered during Leg 180, following the internationally recognized scheme of Bouma (1962).

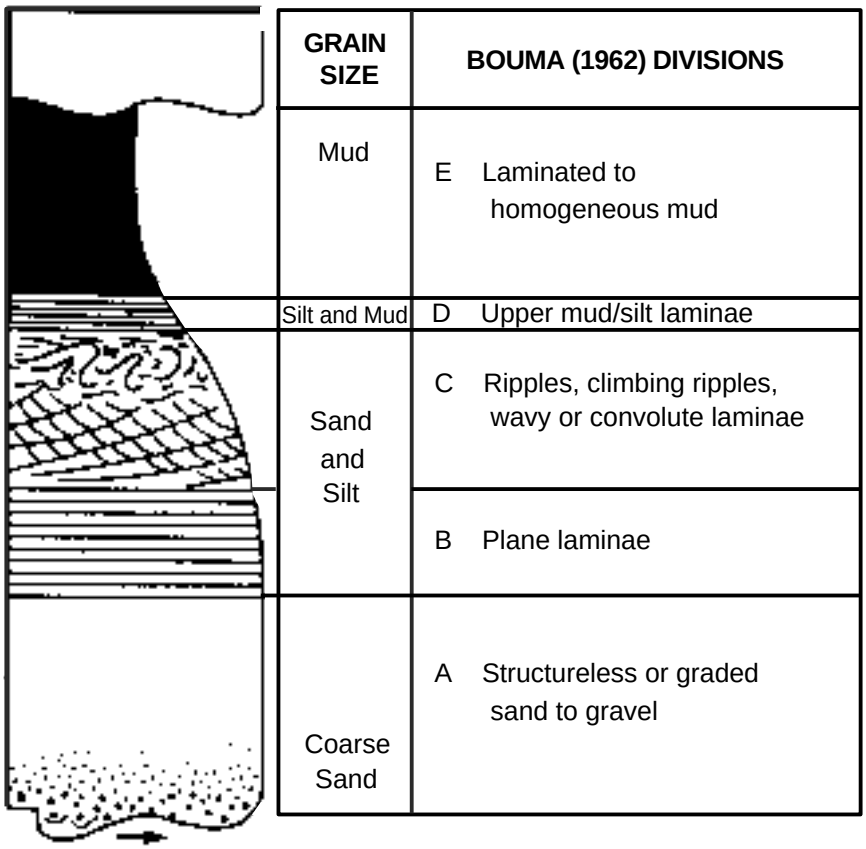

Figure F7. Piper's (1978) descriptive scheme for muddy turbidites, used during Leg 180. The three facies recognized are essentially formed by repetitive turbidite sequences that form relatively thick depositional units. Intensity of bioturbation depends on the recurrence interval of turbidity currents.

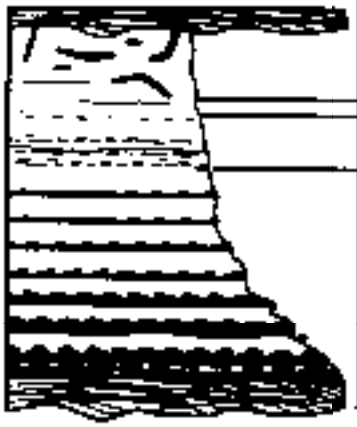

GRAIN SIZE	PIPER DIVISIONS
Mud	E3 Ungraded massive
	E2 Graded
Mud	E1 Laminated
Silt and Mud	D Parallel laminated
Sand and Silt	C Cross laminated

Figure F8. Example of visual core description form used during Leg 180 and previous legs.

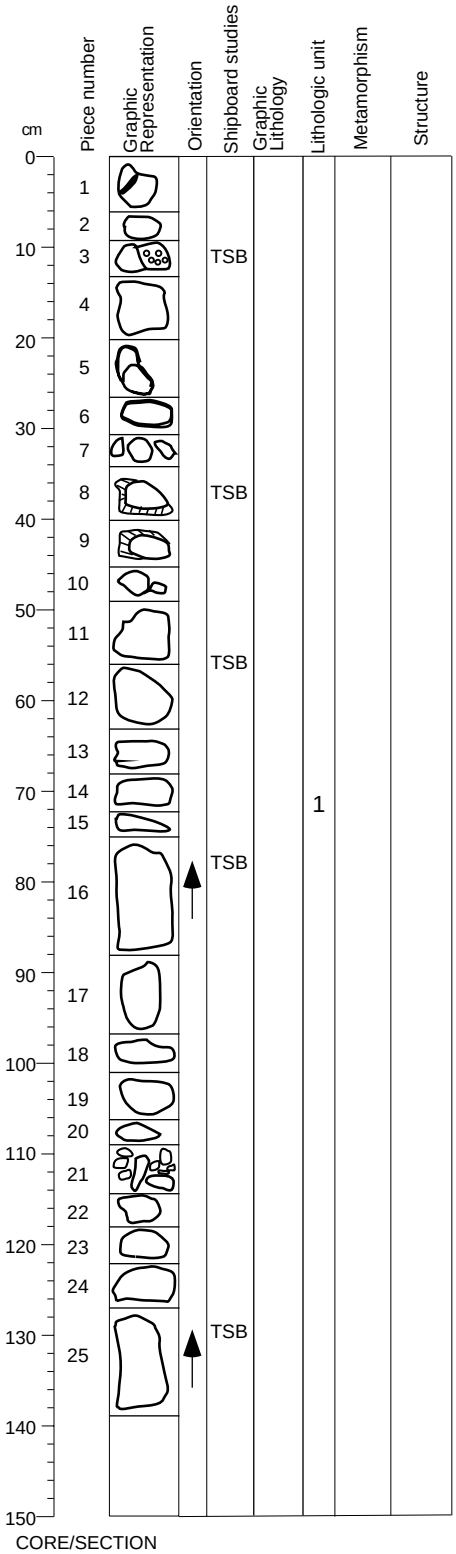

180-1109D-44R-1 (753.6-755.0 mbsf)

UNIT: 1 **CONGLOMERATE** and clasts therefrom

Pieces: 1-25

Interval Location:	Core	Section	Piece	Depth (mbsf)
Upper contact:	44R	1	1	753.60
Lower contact:	44R	1	25	755.00

Thickness (m): 1.40
Contact Type: None

GENERAL: Unit is predominantly a conglomerate containing fine- to medium-grained dolerite clasts within a clay matrix.

GRAIN SIZE: Fine- to medium-grained

TEXTURE: Ophitic

STRUCTURE: None discernable

ALTERATION: Slight, some rusty zones as noted.

COMMENTS: These pieces are thought to be clasts from a conglomerate, liberated by the drilling process.

Piece 1: Conglomerate with 2 basic clasts in a fine-grained matrix. Piece one is 4x2 cm, gray in color (5Y 6/1) in which small ferromagnesian minerals can be seen - probably a dolerite. The other is a 1x1 cm, rounded and apparently unaltered dolerite clast. It is gray (6Y 6/1) and too fine-grained to identify minerals.

Piece 2 is a volcaniclastic sandstone, 6x9 cm, with clastic grains of quartz and ferromagnesian minerals, Fe oxidation is pervasive. Color 5Y 4/4.

Piece 3 is a conglomerate similar to Piece 1. Clasts are well rounded, 5x5 cm to 2x2 cm, and weathered on the outside to rusty material.

Piece 4 is a dolerite similar to Piece1. Color gray (N7/0).

Pieces 5 and 6 are similar to Piece 4 but Piece 5 is slightly more mafic.

Piece 7 contains three small pebbles: a weathered sandstone similar to Piece 2 (1x1.5cm); a very rounded and weathered dolerite with adhereing matrix similar to that in conglomerate Piece 1, and a fresh dolerite similar to Piece 4.

Piece 8 is a chilled basaltic glass - identified from thin section.
Pieces 9-25: Dolerites similar to 4 but variable weathering (particularly 9 and 11, which have iron oxide staining). All rounded, suggesting conglomeratic clasts. These rocks are all fine-grained dolerites, in which only poikilitic ferromagnesian minerals (probably clinopyroxene) in patches up to 1 mm can be distinguished under the hand lens, especially in Pieces 10, 13, 17, 19, 23, and 24). Other pieces appear to be more equigranular.

Figure F9. A. Classification of ultramafic and gabbroic rocks composed of olivine, clinopyroxene, orthopyroxene, and plagioclase (after Le Maitre, 1989). (Continued on next page.)

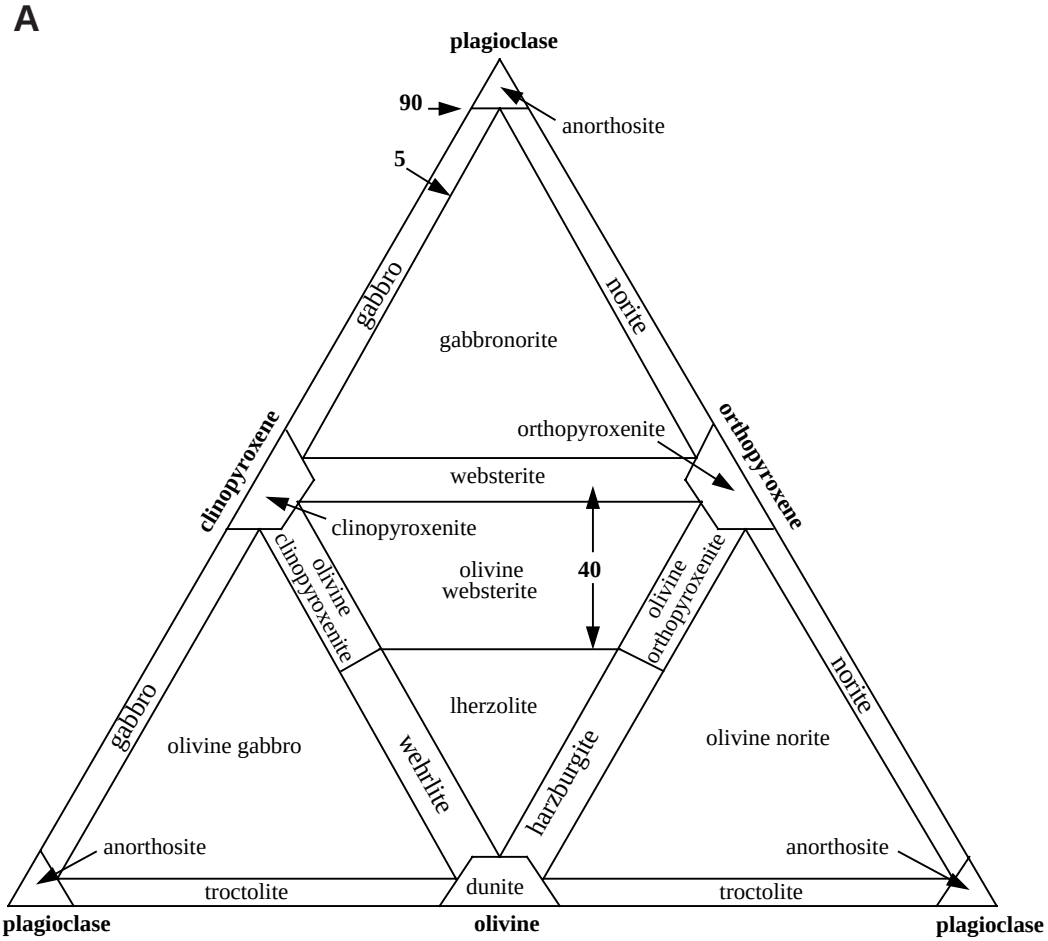

Figure F9 (continued). B. Classification of silicic plutonic rocks composed of quartz, plagioclase, and alkali feldspar (after Le Maitre, 1989).

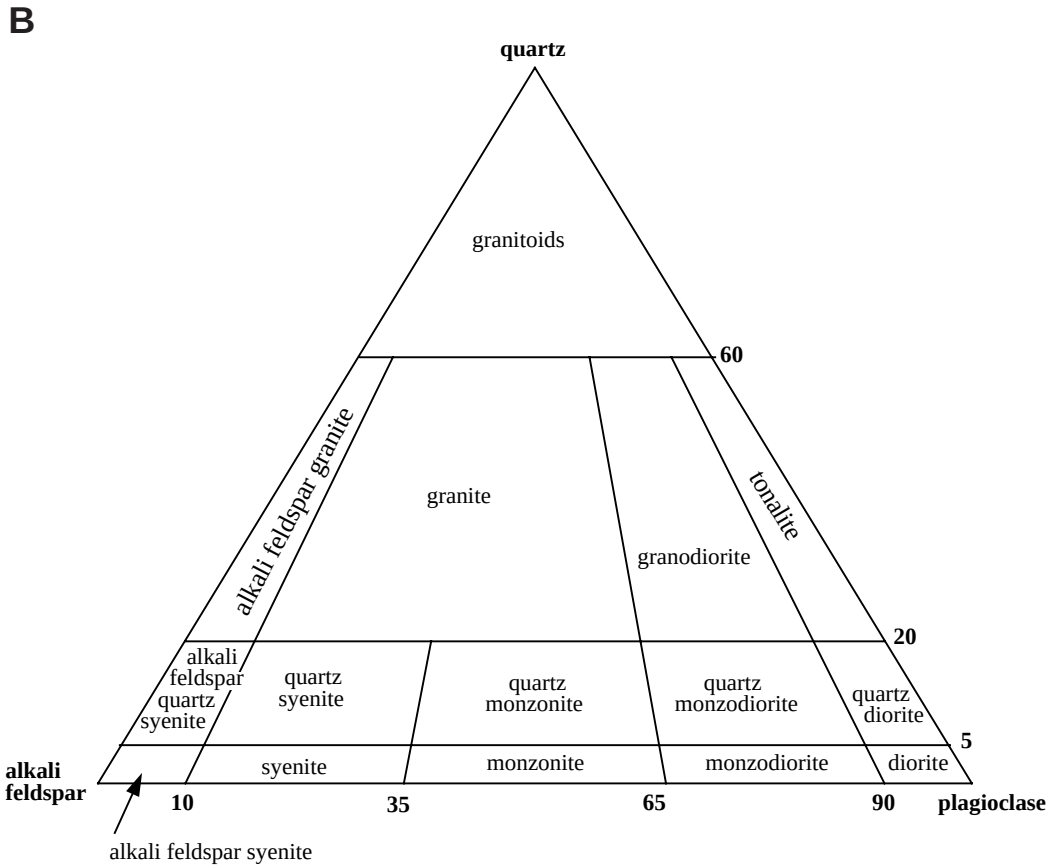

Figure F10. Conventions used for measuring azimuths and dips of structural features in the core, and techniques used for measuring structural planes in three dimensions in the core reference frame. **A.** Working half of the core showing the conventions used for indicating east (090°), west (270°), and south (180°). **B.** Sketch of the archive half of the core showing the conventions used for measuring the dip of a structure on the face of the split core. **C.** Sketch of the core showing the conventions used for measuring the dip of a structure at a right angle to the split core face.

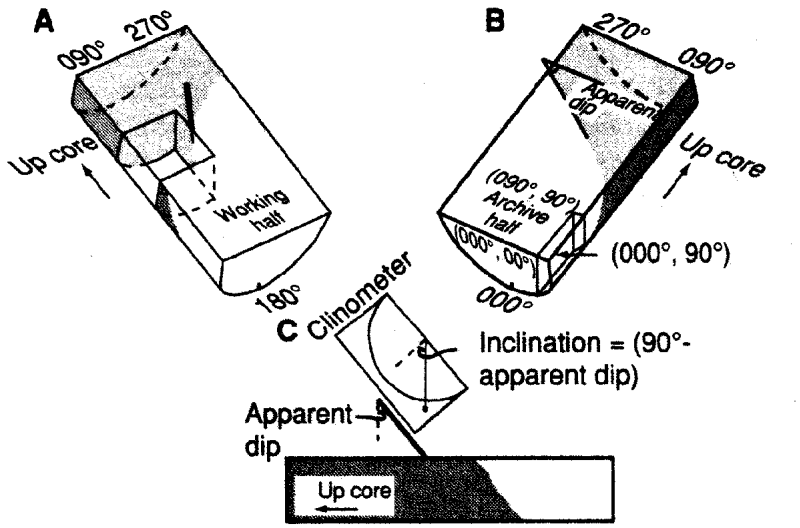

Figure F11. Intensity scales, subdivided into three groups and applied to structural identifiers for brittle and ductile deformation, as used for igneous and metamorphic rocks during Leg 180 (Shipboard Scientific Party, 1995, modified). See **"Fabric Intensities and Textural Terms,"** p. 17 for explanation.

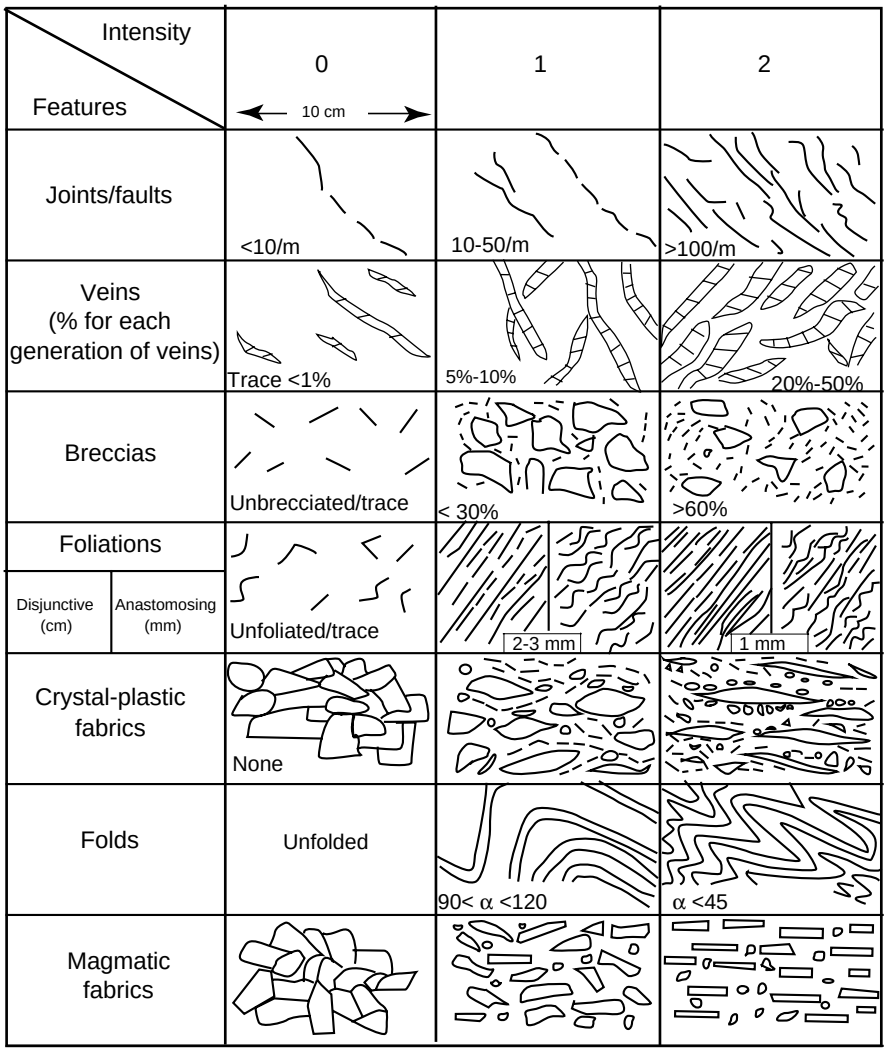

Figure F12. Miocene, Pliocene, and Pleistocene chronostratigraphic units correlated with planktonic foraminifer and calcareous nannofossil zonations and with the geomagnetic polarity scale. Time scale is from Berggren et al. (1995a) with a tri-stage Pliocene based on Rio et al. (1990), and the reports of Cita (1996a, 1996b). Note that the FAD of *G. truncatulinoides,* which defines the base of N22, is globally diachronous and in areas other than the southwest Pacific occurs at 2.0 Ma (Dowsett, 1988).

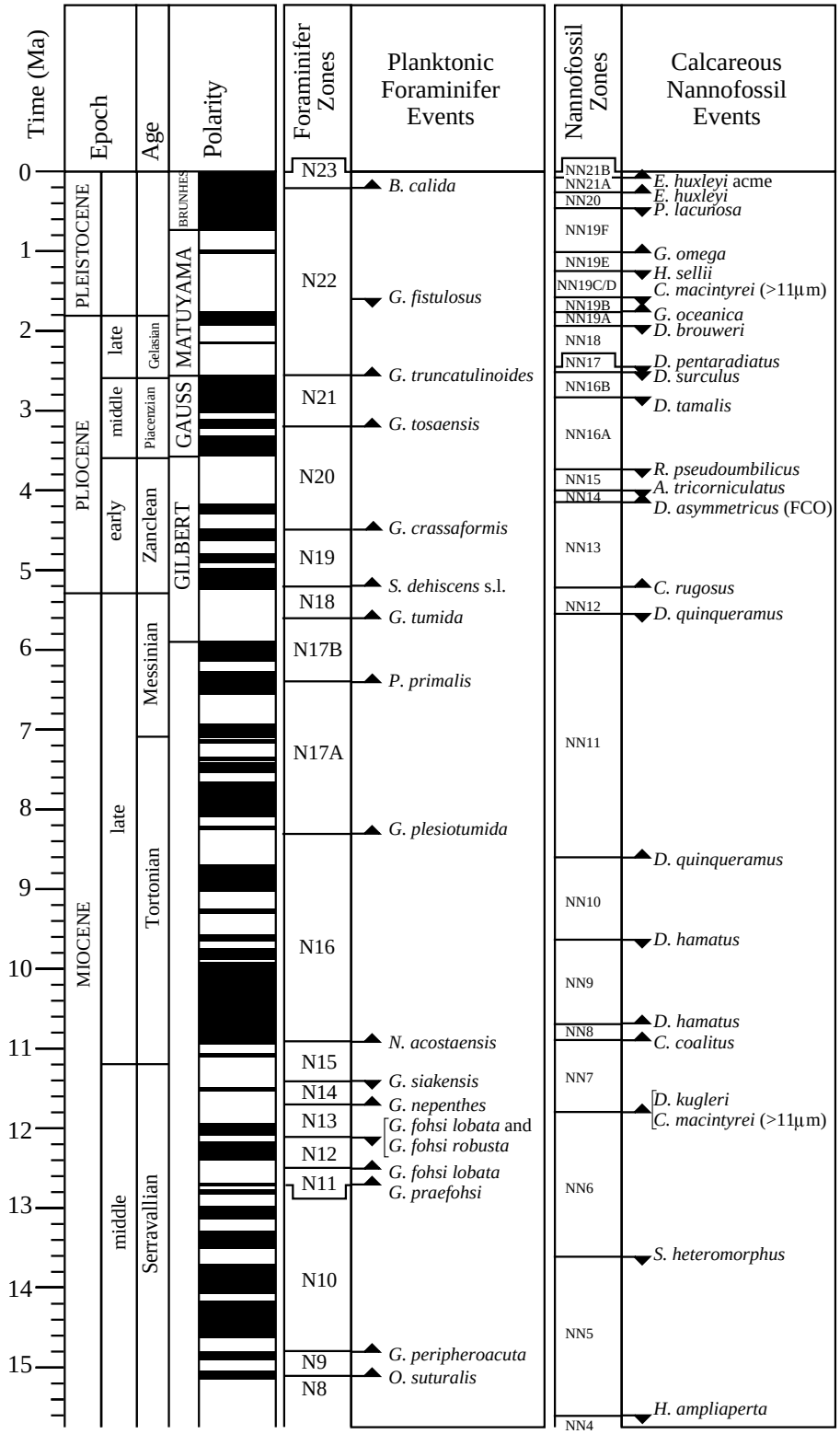

Figure F13. A. ODP paleomagnetic coordinate system for working halves of core sections. **B.** Coordinate system for discrete samples collected with the extruder. **C.** Coordinate system for discrete push-in samples.

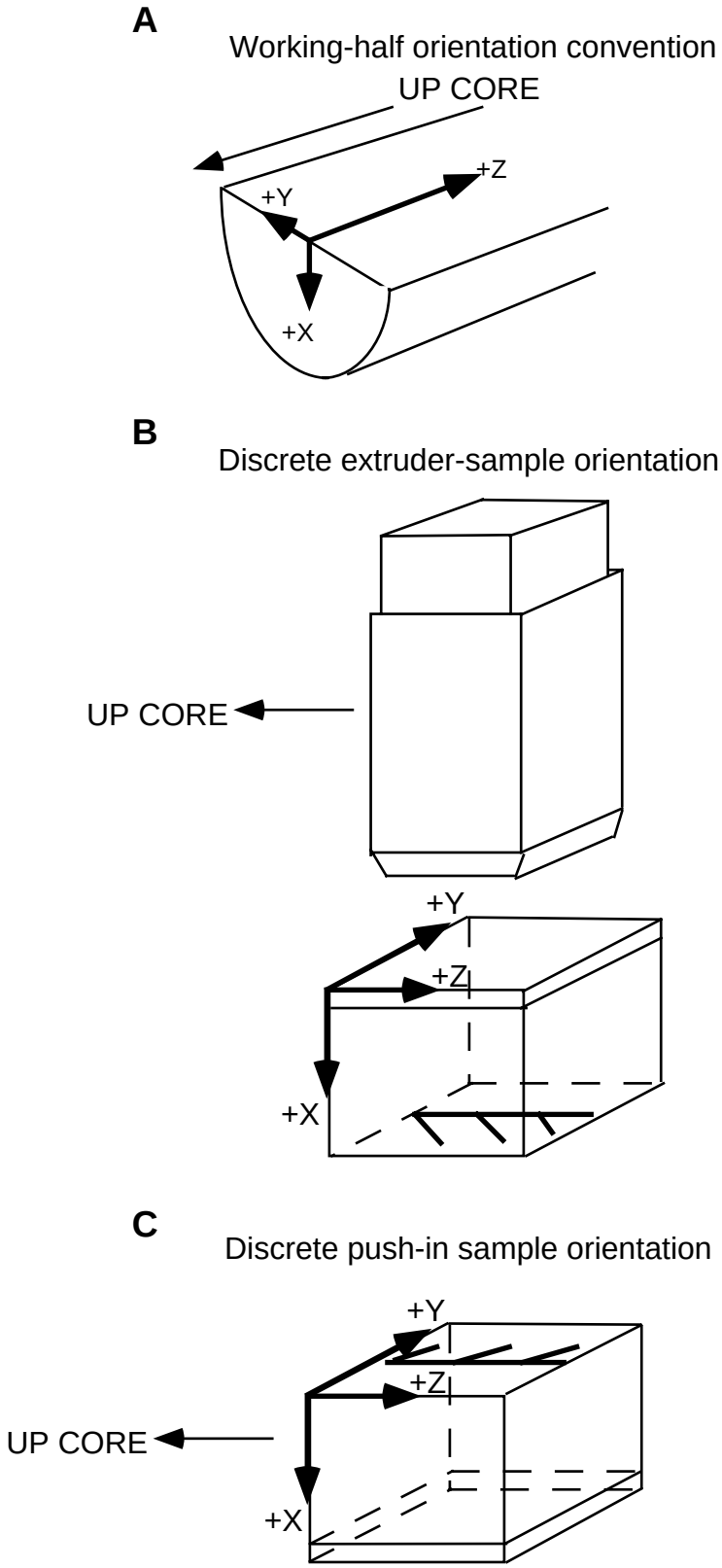

Figure F14. Flow chart depicting the sequence of physical properties measurements for both unconsolidated sediment and hard-rock cores analyzed during Leg 180.

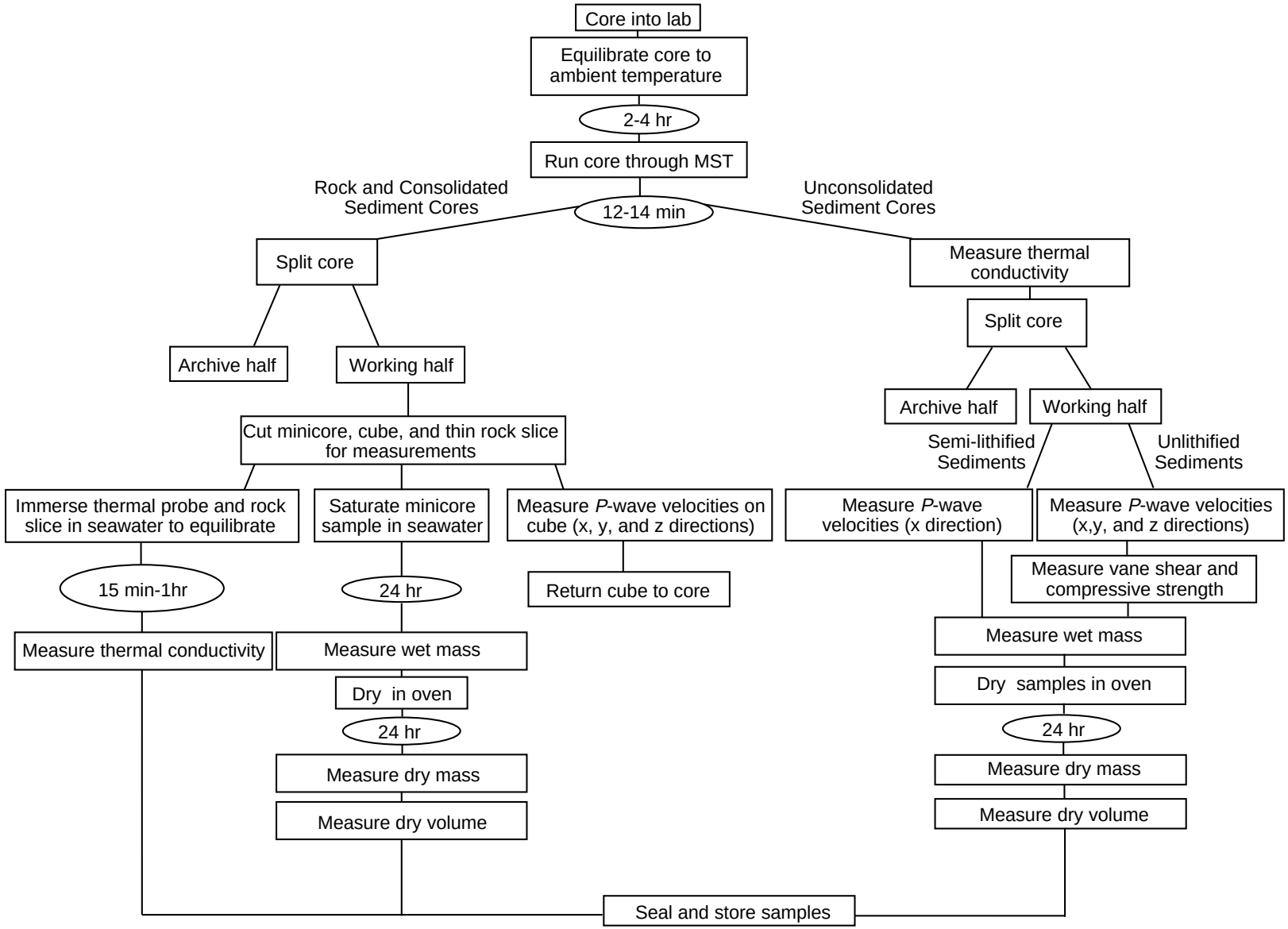

Figure F15. Sketch of the logging tool string combinations used on Leg 180. Weight refers to weight in air of the total string minus TLT. Diameter not to scale with length. Acronyms are listed in Table T7, p. 74. Zero refers to tool zero depth.

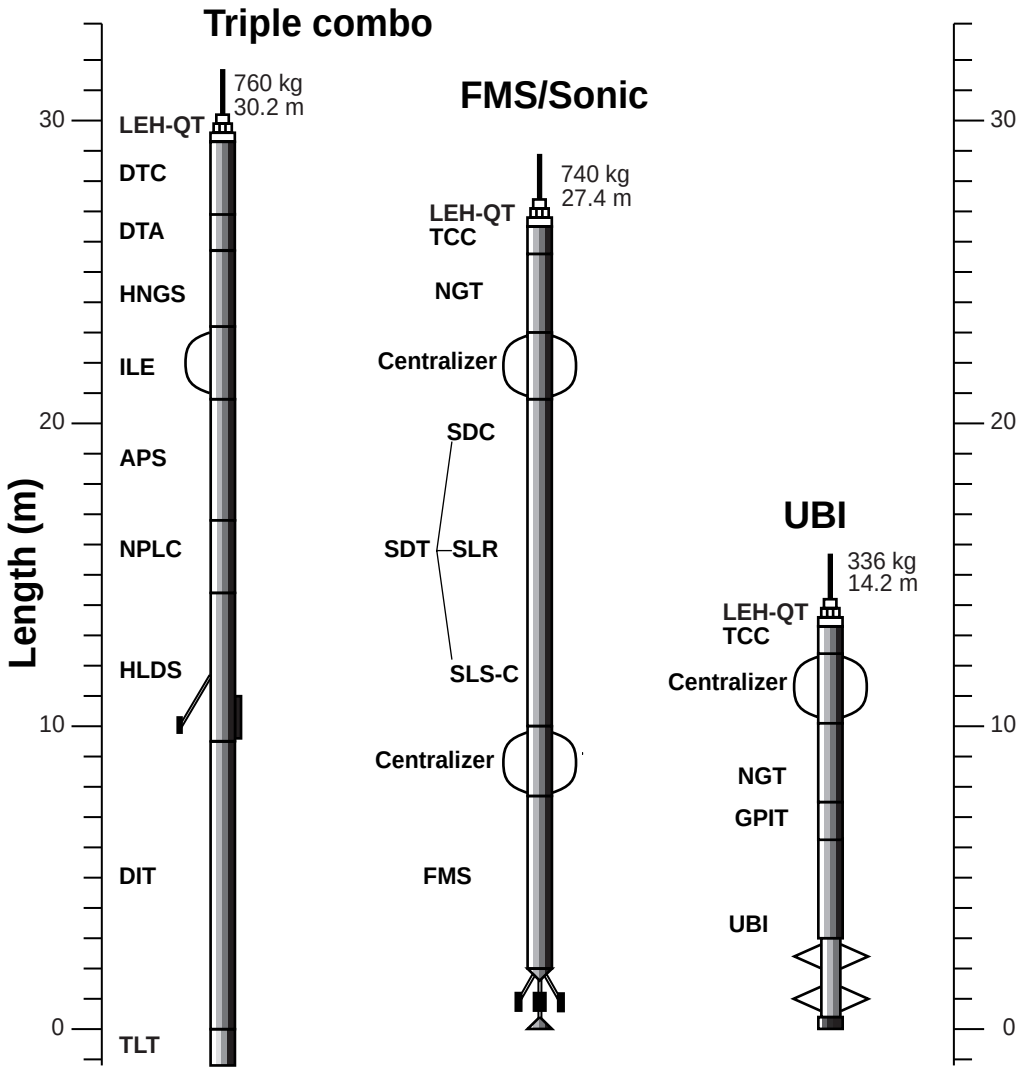

Figure F16. Air-gun configuration for zero-offset VSP experiment.

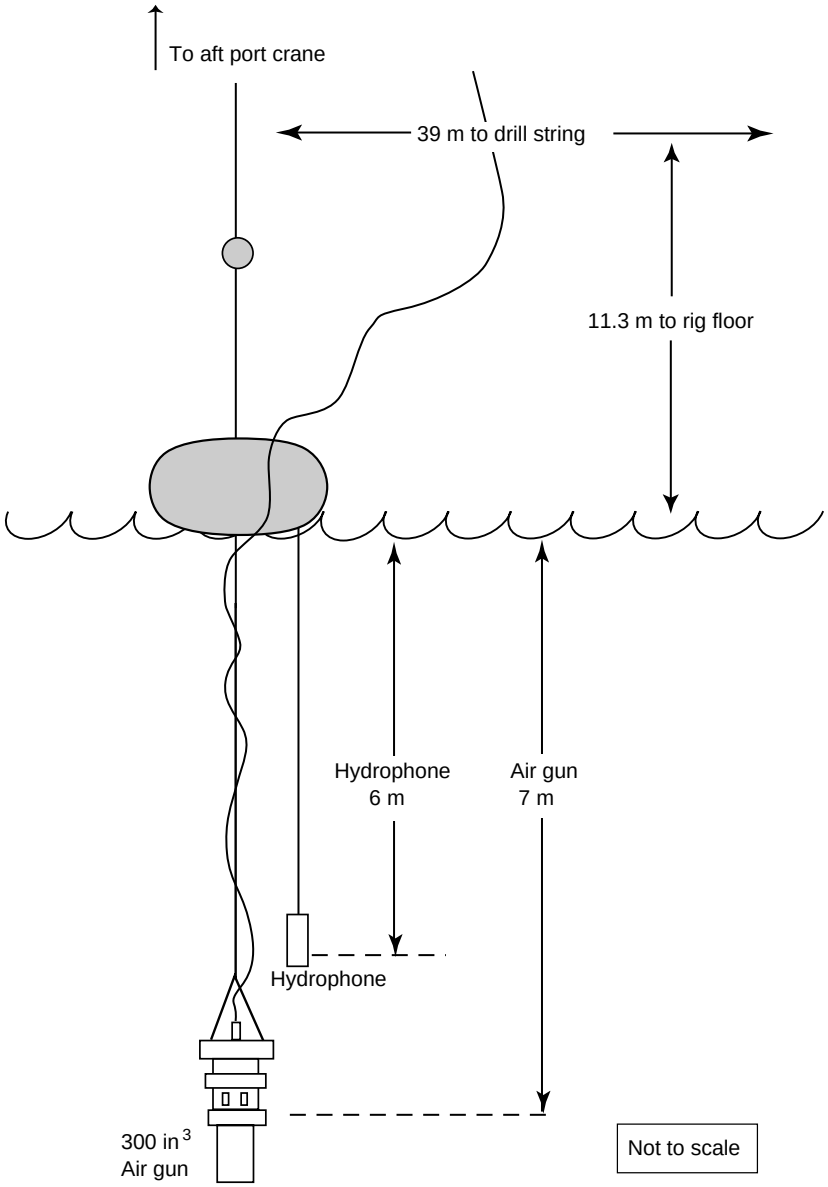

Table T1. Sedimentary rock smear-slide table used during Leg 180.

Core, section, interval (cm)	Depth (mbsf)	Described by	Lithology (dominant/minor)	Size			Siliciclastic and volcaniclastic composition																								Clay	Biogenic composition										Sediment or rock name	Remarks
				Sand	Silt	Clay	Quartz	Feldspar	Plagioclase	Muscovite	Biotite	Glauconite	Amphibole	Pyroxene	Rock fragments (sedimentary)	Rock fragments (metamorphic)	Rock fragments (basaltic)	Volcanic glass	Volcanic glass (brown)	Volcanic glass (colorless)	Accessory minerals	Carbonate	Calcite	Dolomite	Opaque (oxide)	Opaque (sulfide)	Fe oxides	Clinoptinolithe	Phillipsite	Other		Nannofossils	Foraminifers	Diatoms	Radiolarians	Sponge spicules	Shell debris	Organic material	Fish debris	Bioclasts	Unidentified/other		

Table T2. Sedimentary rock thin-section table used during Leg 180.

Thin-section number	Core, section, interval (cm)	Depth (mbsf)	Described by	Lithology (dominant/minor)	Granule	Size	Minerals	Rock fragments		Bioclasts	Lithology type	Comments
						Sand	**Minerals (%)**	**Rock Fragments (%)**		**Bioclasts (%)**		
						Silt	Quartz	Plutonic		Foraminifers		
						Clay	Unstrained	Volcanic		Benthic		
							Feldspar	Rhyolitic/dacitic		Planktonic		
							Multiple twins	Vitric		Shell debris		
							Single/untwinned	Andesitic/basaltic		Algae		
							Mica	Dolerite		Echinoderms		
							Biotite	Sedimentary		Bryozoa/corals		
							Muscovite	Limestone		Carbonaceous detritus		
							Carbonate	Siltstone				
							Chlorite	Metamorphic				
							Accessory minerals	Mica/calc-schist				
							Clinopyroxene	Polycrystalline quartz				
							Amphibole	Serpentinite				
							Olivine	**Matrix (%)**				
							Opaques					

Table T3. XRF analytical conditions for Leg 180.

Oxide or element	Line	Crystal	Detector	Collimator	Peak angle (°2θ)	Background offset (°2θ)	Count time (s)		Analytical error (relative %)	Detection limit
							Peak	Background		
SiO_2	Kα	PET	FPC	Medium	109.21		40		0.30	0.03
TiO_2	Kα	LIF200	FPC	Fine	86.14		40		0.37	0.01
Al_2O_3	Kα	PET	FPC	Medium	145.12		100		0.40	0.01
Fe_2O_3	Kα	LIF200	FPC	Fine	57.52		40		0.20	0.01
MnO	Kα	LIF200	FPC	Fine	62.97		100		0.10	0.005
MgO	Kα	TLAP	FPC	Medium	45.17	±0.80	150	150	0.60	0.01
CaO	Kα	LIF200	FPC	Medium	113.09		40		0.30	0.005
Na_2O	Kα	TLAP	FPC	Medium	54.10	–1.20	150	150	3.8	0.03
K_2O	Kα	LIF200	FPC	Medium	136.69		100		0.40	0.01
P_2O5	Kα	GE111	FPC	Medium	141.04		100		0.40	0.01
Rh	Kα Compton	LIF200	Scint	Fine	18.58		60			
Nb	Kα	LIF200	Scint	Fine	21.40	+0.35	200	100	0.2	0.5
Zr	Kα	LIF200	Scint	Fine	22.55	–0.35	100	50	0.5	0.6
Y	Kα	LIF200	Scint	Fine	23.80	–0.40	100	50	1.0	0.6
Sr	Kα	LIF200	Scint	Fine	25.15	–0.40	100	50	0.3	0.6
Rb	Kα	LIF200	Scint	Fine	26.62	–0.60	100	50	3.6	0.6
Zn	Kα	LIF200	Scint	Medium	41.81	–0.55	100	50	1.0	1.0
Cu	Kα	LIF200	Scint	Fine	45.03	–0.55	100	50	1.5	1.2
Ni	Kα	LIF200	Scint	Medium	48.67	–0.60	100	50	0.6	1.2
Cr	Kα	LIF200	FPC	Fine	69.35	–0.50	100	50	1.3	2.0
V	Kα	LIF220	FPC	Fine	123.06	–0.50	100	50	2.0	3.0
Ti	Kα	LIF200	FPC	Fine	86.14	+0.50	40	20		
Ce	Lα	LIF220	FPC	Medium	128.13	–1.50	100	50		
Ba	Lß	LIF220	FPC	Medium	128.78	–1.50	100	50		

Notes: All major elements were measured using a rhodium X-ray tube operated at 30 kV and 80 mA. Trace elements were measured using a rhodium X-ray tube operated at 60 kV and 50 mA. Detector: FPC = flow proportional counter (P10 gas); Scint = NaI scintillation counter.

Table T4. Checklist for spreadsheet comments associated with each structural identifier as used for metamorphic and sedimentary rocks during Leg 180.

Identifiers	Planar Feature	Linear Feature
DI	Drilling-induced subhorizontal microcracks	
B	Bedding	
UNC	Unconformity	
SFo	Slump fold	
J	Joint	
Fo	Fold	
CC	Crenulation cleavage	
DC	Disjunctive cleavage	
Fol	Foliation	Stretching lineation (SL)
F	Fault	Slickenline (S)
OF, OP	Open fracture	
BSZ	Brittle shear zone	Slickenline (S)
DSZ	Ductile shear zone	Slickenline (S)
SB	Sedimentary breccia	
TB	Tectonic breccia	
V	Veins	Mineral growth direction
D	Dikes	

Note: See **"Macroscopic Core Description,"** p. 15, for discussion.

Table T5. Structural core description form as used during Leg 180.

Core, section, interval (cm)	Feature				Position				Planar						Linear					Fault and shear sense					Vein dyke				Comments
	Unit	Identifier	Piece	Oriented	Identifier	Top	Bottom	mbsf to top of structure	Dip direction 1	Apparent dip 1	Dip direction 2	Apparent dip 2	True strike	True dip	Trend	Plunge	Pitch	Direction of pitch	DS (dip slip) or SS (strike slip)	Nature of fault rocks	Apparent shear sense	Zone thickness	Displacment (mm)	Cross-cutting relationships	Width (mm)	Length (mm)	Texture	Intensity	

Table T6. Ages of calcareous nannofossil and planktonic foraminifer datums used during Leg 180.

Datum events	Species	Age (Ma)
LAD	*Globorotalia flexuosa*	0.068
FAD	*Emiliania huxleyi* acme	0.085
LAD	*Globoquadrina pseudofoliata*	0.22
FAD	*Bolliella calida*	0.22
FAD	*Emiliania huxleyi*	0.26
FAD	*Globorotalia flexuosa*	0.401
FAD	*Globorotalia hirsuta*	0.45
LAD	*Pseudoemiliania lacunosa*	0.46
LAD	*Globorotalia tosaensis*	0.65
FAD	*Globorotalia crassaformis hessi*	0.75
LAD	*Reticulofenestra asanoi*	0.88
FAD	*Gephyrocapsa omega*	1.02
LAD	*Helicosphaera sellii*	1.25
LAD	*Globigerinoides fistulosus*	1.6
LAD	*Calcidiscus macintyrei*	1.67
FAD	*Gephyrocapsa oceanica*	1.75
LAD	*Globigerinoides extremus*	1.77
LAD	*Discoaster brouweri*	1.95
LAD	*Discoaster pentaradiatus*	2.52
LAD	*Discoaster surculus*	2.55
FAD	*Globorotalia truncatulinoides*	2.58
LAD	*Globorotalia pertenuis*	2.60
LAD	*Discoaster tamalis*	2.83
LAD	*Dentoglobigerina altispira*	3.09
LAD	*Globorotalia multicamerata*	3.09
LAD	*Sphaeroidinellopsis seminulina*	3.12
FAD	*Sphaeroidinella dehiscens* s.s	3.25
FAD	*Globorotalia fistulosus*	3.33
FAD	*Globorotalia tosaensis*	3.35
LAD	*Globorotalia margaritae*	3.58
LAD	*Pulleniatina primalis*	3.65
LAD	*Reticulofenestra pseudoumbilicus*	3.75
S. to D. coil	*Pulleniatina*	3.95
LAD	*Amaurolithus tricorniculatus*	4.0
FCO	*Discoaster asymmetricus*	4.13
LAD	*Globoturborotalita nepenthes*	4.20
LAD	*Pulleniatina spectabilis*	4.20
FAD	*Globorotalia crassaformis*	4.5
LAD	*Globigerinoides seigliei*	4.7
FAD	*Sphaeroidinella dehiscens* s.l.	5.20
LAD	*Ceratolithus acutus*	5.05
FAD	*Ceratolithus rugosus*	5.23
FAD	*Ceratolithus acutus*	5.37
LAD	*Discoaster quinqueramus*	5.54
FAD	*Globorotalia tumida*	5.60
LAD	*Globoquadrina dehiscens*	5.8
LAD	*Globorotalia lenguaensis*	6.0
FAD	*Globorotalia margaritae*	6.0
FAD	*Pulleniatina primalis*	6.4
S. to D. coil	*Neogloboquadrina acostaensis*	6.2
D. to S. coil	*Neogloboquadrina acostaensis*	6.6
FAD	*Amaurolithus primus*	7.2
FAD	*Globorotalia cibaoensis*	7.8
FAD	*Globorotalia juanai*	8.1
FAD	*Candeina nitida*	8.1
FAD	*Globigerinoides extremus*	8.3
FAD	*Globorotalia plesiotumida*	8.3
FAD	*Neogloboquadrina humerosa*	8.5
FAD	*Discoaster quinqueramus*	8.6
LAD	*Discoaster hamatus*	9.63
FAD	*Discoaster hamatus*	10.7
FAD	*Neogloboquadrina acostaensis*	10.9
FAD	*Catinaster coalitus*	10.9
LAD	*Neogloboquadrina mayeri*	11.4
LAD	*Discoaster kugleri*	11.5
FAD	*Globoturborotalia nepenthes*	11.8
FAD	*Discoaster kugleri*	11.8
LAD	*Globorotalia fohsi robusta*	11.9
LAD	*Globorotalia fohsi lobata*	12.1
FAD	*Globorotalia fohsi robusta*	12.3
FAD	*Globorotalia fohsi lobata*	12.5
FAD	*Globorotalia fohsi* s.s.	12.7
FAD	*Globorotalia praefohsi*	12.7
LAD	*Sphenolithus heteromorphus*	13.6
LAD	*Globorotalia peripheronda*	14.6
FAD	*Globorotalia peripheroacuta*	14.8
FAD	*Orbulina suturalis*	15.1
LAD	*Helicosphaera ampliaperta*	15.6
LAD	*Sphenolithus belemnos*	19.2

Notes: LAD = last occurrence datum; FAD = first occurrence datum; "S. to D. coil" refers to the change from sinistral to dextral coiling; FCO = first common occurrence. Nannofossil datum ages are taken from the ODP JANUS datum-database dictionary, Shackleton et al. (1995), and Sprovieri (1993). Foraminifer datum ages are from Berggren et al. (1995a) and Berggren et al. (1995b).

Table T7. Logging tool strings and components.

Combinations	Subcombination		Component	
	Acronym	Name	Acronym	Name
Triple combo			LEH-QT	Logging equipment head-q tension
			DTC	Digital telemetry cartridge
			DTA	Digital telemetry adaptor
			HNGS	Hostile environment natural gamma-ray sonde
			ILE	In-line eccentralizer
			APS	Accelerator porosity sonde
			NPLC	Nuclear porosity lithology cartridge
			HLDS	Hostile environment litho-density sonde
			DIT	Dual induction tool
			TLT	LDEO temperature-logging tool
FMS-sonic			LEH-QT	Logging equipment head-q tension
			TCC	Telemetry communication cartridge
			NGT	Natural gamma-ray tool
	SDT-C	Array sonic digital tool	SDC	Sonic digital cartridge
			SLS-C	Sonic logging sonde
			SLR	Sonic logging receiver
	FMS	Formation MicroScanner	MEST-B	Micro-electric scanner tool
			GPIT	General purpose inclinometry tool
Ultrasonic			LEH-QT	Logging equipment head-q tension
			TCC	Telemetry communication cartridge
			NGT	Natural gamma-ray tool
			GPIT	General purpose inclinometry tool
			UBI	Ultrasonic borehole imager

Table T8. Logging acronyms and measurements.

Measurements	Data channel	Tool acronym	Method	Units	Vertical resolution (cm)	Vertical sampling (cm)	Depth of investigation (cm)
Electrical properties							
Resistivity	IDPH	DIT	Deep induction	Ωm	200	15	120-150
	IMPH	DIT	Medium induction	Ωm	150	15	60-80
	SFLU	DIT	Shallow spherically focused current	Ωm	75	15	30-40
Microelectrical images	MEST		Button resistivity		0.5	0.25	~5
Density-porosity							
Density	RHOM	HLDS	Formation density (gamma ray scattering)	$g \cdot cm^{-3}$	40	15	20
	DRH	HLDS	Density correction (<0.25g/cm^3 for good data)	$g \cdot cm^{-3}$	40	15	20
Photoelectric effect	PEFL	HLDS	<200 KeV gamma ray	barns/e$^-$	40	15	20
	PEFS	HLDS	<200 KeV gamma ray	barns/e$^-$	15	15	10
Porosity	APLC	APS	Porosity by neutrons backscattering (near/array)	#	30	15	20
	HALC	APS	Neutrons backscattering (near/array)	#	20	5	20
	FPLC	APS	Neutrons backscattering (far/array)	#	60	15	50
	HFLC	APS	Neutrons backscattering (far/array)	#	30	5	50
Sigma	SIGF	APS	Thermal neutron capture rate	cu	30	15	20
	HSIG	APS	Thermal neutron capture rate	cu	30	5	20
Stand off	STOF	APS	Epithermal neutron (<3 cm for good data)	in	30	15	20
	HSTO	APS	Epithermal neutron (<3 cm for good data)	in	30	5	20
Sound waves							
Traveltime	LTT1-4	SDT	10-, 8-, 12-, and 10-ft source-receivers spacings	μs	240-360	15	1-30
	TT1-4	SDT	5-, 3-, 7-, and 5-ft source-receivers spacings	μs	90-150	15	1-15
Slowness	DTLF	SDT	12- and 10-ft source-receivers spacings	$\mu s \cdot ft^{-1}$	61	15	1-30
	DTLN	SDT	10- and 8-ft source-receivers spacings	$\mu s \cdot ft^{-1}$	61	15	1-30
	DTL	SDT	7- and 5-ft source-receivers spacings	$\mu s \cdot ft^{-1}$	61	15	1-15
	DT	SDT	5- and 3-ft source-receivers spacings	$\mu s \cdot ft^{-1}$	61	15	1-15
	DTCO	SDT	1/Vp from array receivers	$\mu s \cdot ft^{-1}$	107	15	1-30
	DTSM	SDT	1/Vs from array receivers	$\mu s \cdot ft^{-1}$	107	15	1-30
Waveforms	WF1-4	SDT	Either LTT or TT spacings	#	90-360	15	1-30
	PWF0	SDT	eight array receivers packed (not on depth)	#	90-360	15	1-30
Ultrasonic images		UBI	Rotating transducer + receiver		0.5	0.5	0
Traveltime	TTBN	UBI	Eccentering corrected traveltime	μs	0.5	0.5	0
Attenuation	AWBN	UBI	Eccentering corrected amplitude	dB	0.5	0.5	0
Temperature							
Tool	ITEM	DIT	Tool internal temperature	°C	NA	15	0
Borehole fluid	TF	TLT	Thermistors in borehole fluid	°C	NA	NA	0
	TS						
Fluid pressure	PT	TLT	Gauge in borehole fluid	psi	NA	NA	0
Natural gamma ray	SGR	NGT	Total gamma ray count	GAPI	45	15	30-50
	CGR	NGT	Total gamma ray count minus Uranium	GAPI	45	15	30-50
	URAN and THOR	NGT	U and Th by spectral gamma ray	ppm	45	15	30-50
	POTA	NGT	K by spectral gamma ray	#	45	15	30-50
	HSGR	HNGS	Total gamma ray count	GAPI	45	15	30-50
	HCGR	HNGS	Total gamma ray count minus Uranium	GAPI	45	15	30-50
	HURA and HTHO	HNGS	U and Th by spectral gamma ray	ppm	45	15	30-50
	HFK	HNGS	Formation K by spectral gamma ray	#	45	15	30-50
	HBK	HNGS	Borehole fluid K by spectral gamma ray	#	45	15	30-50
Borehole geometry							
Diameter	LCAL	HLDS	Caliper	in	45	15	0
	C1 and C2	FMS	Caliper	in	10	3.8-15	0
Radii	IRBC	UBI	Corrected radii	in	0.5	0.5	0
Deviation	DEVI	GPIT	Deviation from accelerometer	degrees	3000	15	NA
Azimuth	HAZI	GPIT	Azimuth from magnetometer and accelerometer	degrees	3000	15	NA
Magnetic field							
Components	FX, FY, and FZ	GPIT	Three-components magnetometer	Oer	15	3.8-15	0
Magnitude	FNOR	GPIT	Three-components magnetometer	Oer	15	3.8-15	0
Inclination	FINC	GPIT	Three-components magnetometer	degrees	15	3.8-15	0
Tool dynamics							
Pad 1 azimuth	P1AZ	GPIT	Azimuth from magnetometer	degrees	5	3.8-15	NA
Relative bearing	RB	GPIT	Pad 1angle with upper hole side from accelerometer	degrees	5	3.8-15	NA
Acceleration	AX, AY, AZ, and AN	GPIT	Three-components accelerometer	$m \cdot s^{-2}$	4	3.8-15	NA
Cable tension	TENS	LEH-QT	Strain gauge	lb	NA	15	NA

Notes: Acronyms are defined in **"Downhole Measurements,"** p. 34. # = nondimensional. NA = not applicable.